A Precision Millimeter-Wave Measurement of the Rydberg Frequency

by

Joel Christopher De Vries

B.S., The University of Michigan (1993)

Submitted to the Department of Physics
in partial fulfillment of the requirements for the degree of

Doctor of Philosophy

at the

MASSACHUSETTS INSTITUTE OF TECHNOLOGY

February 2002

Author . . . .
Department of Physics
November 8, 2001

Certified by . . . .
Daniel Kleppner
Lester Wolfe Professor of Physics
Thesis Supervisor

Accepted by . . . .
Thomas J. Greytak
Professor of Physics
Associate Department Head for Education

A Precision Millimeter-Wave Measurement of the Rydberg Frequency

by

Joel Christopher De Vries

Submitted to the Department of Physics
on November 5, 2001, in partial fulfillment of the
requirements for the degree of
Doctor of Philosophy

Abstract

The Rydberg frequency, cR_∞, sets the frequency scale for the spectrum of hydrogen atoms. From a frequency measurement of one transition in hydrogen, cR_∞ can be extracted and the frequency of any other transition can be predicted, given that the reduced-mass, relativistic, QED, and proton structure corrections can be computed to the desired accuracy. Recent advances in optical frequency techniques applied to transitions involving low-lying states of hydrogen have decreased the uncertainty in cR_∞ to 7.6×10^{-12}. This thesis presents our measurement of cR_∞ using millimeter-wave transitions between high-lying "circular Rydberg" states of atomic hydrogen with a principle quantum number, n, between 27 and 30. This measurement provides an independent check, in a different regime, of the optical measurements. Our measurement, $cR_\infty = 3\,289\,841\,960\,306(69)$ kHz with an uncertainty of 2.1×10^{-11}, is consistent with the CODATA 98 recommended value.

Thesis Supervisor: Daniel Kleppner
Title: Lester Wolfe Professor of Physics

To my parents,
Lee and Jean De Vries,

and my fiancée,
Meg Fairbank.

Contents

List of Figures

List of Tables

Chapter 1

Introduction

1.1 Significance of the Rydberg frequency

The Rydberg frequency cR_∞ sets the scale for the frequency spectrum of atomic hydrogen. The Balmer formula gives the non-relativistic transition frequency ν_{nr} between two states with principal quantum numbers n_1 and n_2:

$$\nu_{nr} = cR_\infty \left(\frac{1}{n_1^2} - \frac{1}{n_2^2} \right) . \tag{1.1}$$

The actual transition frequencies in hydrogen include small contributions due to external fields, relativistic effects and the Lamb shift, and there are small corrections due to the finite mass of the proton.

The Rydberg frequency cR_∞ is the best known fundamental constant. The recommended value from CODATA 98[MT00] for cR_∞ is

$$cR_\infty = 3\,289\,841\,960\,368(25)\ \text{kHz}, \tag{1.2}$$

which has a fractional uncertainty of 7.6×10^{-12}. This value is based on all available measurements of transition frequencies in hydrogen and deuterium, totalling 23 measurements from 5 different laboratories. The most important of these measurements are optical measurements involving low-lying states.

Currently, a more precise value of cR_∞ is needed to extract a better value for the ground state Lamb shift of hydrogen $E_{Lamb}(1S_{1/2})$ from the $1S_{1/2} \rightarrow 2S_{1/2}$ transition frequency. This transition frequency has been measured to a fractional precision of 1.5×10^{-14}[UHG+97]. Thus, any improvement in the value for cR_∞ would result in a more precise experimental value for $E_{Lamb}(1S_{1/2})$.

Another role for the Rydberg frequency is providing a cornerstone in the determination of other fundamental constants. Bohr theory predicts the value of cR_∞ to be

$$cR_\infty = \frac{\alpha^2 m_e c^2}{2h}, \tag{1.3}$$

where α is the fine structure constant, m_e is the mass of the electron, c is the speed of light, and h is the Planck constant. For instance, an ongoing effort [BPR+99] to measure the fine structure constant α utilizes the highly accurate determination of cR_∞ and Eq. (1.3) to help extract a value for α. The current value of cR_∞ is so precise that it does not limit this determination of α.

1.2 Motivation for our measurement of cR_∞

The history of fundamental constants underscores the importance of independent measurements. For example, the CODATA 1986[CT87] recommended value for cR_∞ has a fractional uncertainty of 1.2×10^{-9}, but it is fractionally 3.2×10^{-9} times smaller than the current recommended value from CODATA 1998 [MT00]. Such major revisions of fundamental constants are not that unusual. For instance, a similar revision of the fine structure constant α occurred in the mid 1960s, and currently there is significant discrepancy between different measurements of α[Kin96].

Our measurement is totally different from previous measurements because it employs millimeter-wave spectroscopy on high-lying "circular Rydberg" states of atomic hydrogen. A "Rydberg" state has a principal quantum number n much greater than one, and a "circular Rydberg" state has the maximal amount of angular momentum, given its principal quantum number ($\ell = |m_\ell| = n - 1$). The frequency metrology in our experiment is technically different from the optical measurements. The frequency of the radiation that we employ is small enough (≈ 300 GHz) to be easily synthesized and referenced to a cesium clock, which is the primary frequency reference. Hence, our measurement provides a check of techniques employed in the new field of optical frequency metrology. Also, the transitions that we use are different from the optical measurements. Most notably, they are insensitive to QED and proton structure perturbations.

While the precision for our measurement of cR_∞ does not surpass the precision of the current recommended value, the historical discrepancy of nearly 3σ in cR_∞ shows the need for a competitive, independent measurement in order to add reliability to the value for cR_∞.

1.3 Basic method

Our basic method is as follows: We measure the transition frequency of the $n = 27 \rightarrow 28$ or the $n = 29 \rightarrow 30$ "circular state transition" in hydrogen. By circular state transition, we mean a transition between circular states. Specifically, the quantum numbers describing the transitions that we measure are

$$(n; \ell = n-1; |m_\ell| = n-1) \rightarrow (n+1; \ell = n; |m_\ell| = n), \tag{1.4}$$

where $n = 27$ or 29. We then subtract off the frequency contributions due to the external fields and the fine structure (the Lamb shift and the hyperfine structure are essentially negligible for our purposes) to obtain $\nu_{nr}^{27\rightarrow 28}$ or $\nu_{nr}^{29\rightarrow 30}$. The Balmer formula, as given in Eq. (1.1), relates the non-relativistic transitions frequencies ν_{nr} to the Rydberg frequency cR_∞:

$$\begin{aligned} cR_\infty &= \nu_{nr}^{27\rightarrow 28}\left(\frac{1}{27^2} - \frac{1}{28^2}\right)^{-1} \\ cR_\infty &= \nu_{nr}^{29\rightarrow 30}\left(\frac{1}{29^2} - \frac{1}{30^2}\right)^{-1} \end{aligned}$$

In this discussion we ignored the corrections due to the finite mass of the proton, which must be taken into account before determining cR_∞. We discuss the finite-mass correction and all the contributions to the transition frequencies in Chapter 2.

1.4 Principle of the experiment

We use the Ramsey resonance method on an atomic beam to measure the circular state transition frequencies. Here we present only a brief description of the principle of the experiment; details on the lineshape and the experimental apparatus are given in Chapters 3 and 4, respectively.

We dissociate molecular hydrogen into atomic hydrogen. The atomic hydrogen then flows into a thermalizer at 80 K. The atoms exit the thermalizer, forming the atomic beam, and we collimate the beam using a slit.

The atomic beam enters the interaction region, which is shown schematically in Fig. 1-1. We logically divide the interaction region into three sections: the production region, the separated fields region, and the detection region.

In the production region we use a pulse of optical radiation at 121 nm to excite the atoms from the ground state to the $2P_{3/2}$ state. A simultaneous pulse at 366 nm further excites the atoms from the $2P_{3/2}$ state to a Rydberg state with $n = 27$ or 29. Then we circularize the Rydberg atoms using 1.81 GHz circularly polarized RF radiation, leaving them in the $\ell = |m_\ell| = n - 1$ state.

In the separated fields region, the atoms traverse the waists of two gaussian beam modes contained in two near-confocal cavities. These are the two oscillatory fields that we use in the Ramsey resonance method, and they drive transitions between the circular states with quantum numbers n and $n + 1$.

In the detection region, we use selective field ionization to count the number of atoms in the n and $n + 1$ circular states as a function of the transit time (the time from optical excitation to detection), the frequency of the oscillatory fields, etc.. The detector has an aperture which restricts the trajectories of the detected atoms.

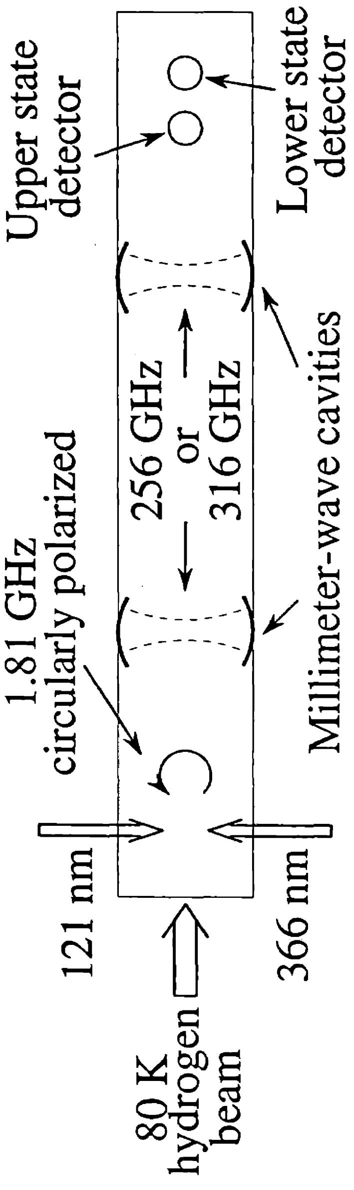

Figure 1-1: Schematic top view of the interaction region.

Chapter 2

Contributions To The Transition Frequencies

We measure the absolute frequencies of transitions between two adjacent circular Rydberg states with principal quantum numbers, n_i and $n_f = n_i + 1$, where $n_i = 27$ or 29. Note that for a circular state with principal quantum number n, the angular momentum and magnetic quantum numbers take on the maximal values: $\ell = |m_\ell| = n - 1$. In this section we discuss the contributions to these transition frequencies that are necessary to determine the Rydberg frequency cR_∞ from our data.

Throughout this thesis, we use SI units, except we use the CGS unit of magnetic field (Gauss) in numerical expressions (10^4 G = 1 T). We use values for the fundamental constants as reported in CODATA 98 [MT00].

For clarity, we reserve the symbol E for the energy of an energy level and the symbol ΔE for the difference in E between two energy levels. Experimentally, we observe the frequency of a transition between two levels, and we use the symbol ν to represent the transition frequency, where $\nu = \Delta E/h$. We reserve the symbol $\Delta\nu$ for the substructure of a transition, for instance the fine structure splitting of a transition frequency.

We start by enumerating the terms in the Hamiltonian H for a hydrogen atom with a proton of infinite mass, and we list the terms in descending order of importance for our measurement conditions:

$$H = H_{nr} + H_S + H_Z + H_{fs} + H_{QED} + H_{hfs}, \tag{2.1}$$

where H_{nr} is the non-relativistic Hamiltonian for the hydrogen atom, and the other terms are perturbations due to: the Stark effect, the Zeeman effect, fine structure, QED effects, and hyperfine structure.

To set the scale for significant interactions, the transition frequencies that we measure are about 300 GHz, and a fractional uncertainty of 1×10^{-11} corresponds to about 3 Hz. In electric and magnetic fields that we typically apply, the contributions to the circular state transition frequencies from the terms in Eq. 2.1 are: (Here, the ($\pm$) signs represent the dependence of the transition frequency on the sign of m_ℓ, m_s, or m_i, where m_s and m_i are the electron and proton spin quantum numbers.) $\nu_{nr} \approx 3 \times 10^{11}$ Hz, $\nu_S \approx -5 \times 10^2$ Hz, $\nu_Z \approx \pm 2 \times 10^5$ Hz, $\nu_{fs} \approx -10^4 \pm 2 \times 10^3$ Hz, $\nu_{QED} \approx -0.1 \pm 1$ Hz, and $\nu_{hfs} \approx \pm 1$ Hz. Note that the Stark effect contribution ν_S is not the largest contribution compared to the other perturbations: For our conditions, the first-order Stark effect is the dominant perturbation to the general energy level structure of Rydberg atoms, but it does not affect the circular state transition frequencies because circular states do not exhibit a first-order Stark effect. The value quoted above ($\nu_S \approx -5 \times 10^2$ Hz) comes from the second-order Stark effect.

In the rest of this section, we discuss each term in the "infinite proton mass" Hamiltonian (Eq. 2.1). For each term, we calculate the contribution to a circular state transition frequency, and then we include a correction due to the finite mass of the proton, which we refer to as a "finite-mass correction". This correction is a multiplicative factor of

$$\left(\frac{\mu}{m_e}\right)^\beta, \tag{2.2}$$

where β is an integer that depends on the situation and μ is the reduced mass for hydrogen, defined by

$$\frac{\mu}{m_e} = \frac{1}{1 + m_e/m_p}. \tag{2.3}$$

In most cases, $\beta = 1$ and the effect of including this factor is simply to replace the mass of the electron with the reduced mass. The value of this factor comes from the measurement of $m_e/m_p = 5.446\,170\,232(12) \times 10^{-4}$[MT00], which has a fractional uncertainty of 2.1×10^{-9}, so that μ/m_e is known to a fractional uncertainty of 1.2×10^{-12}. The uncertainty introduced by the finite-mass corrections is negligible.

At the end of this section, we calculate the frequencies of transitions between "near-circular" states. These states have $|m_\ell| = n - 2$ rather than $|m_\ell| = n - 1$, and we use them to calibrate the applied electric field because they exhibit a first-order Stark effect.

2.1 Balmer formula

The eigenvalues of H_{nr} are $E_{nr} = -cR_\infty/n^2$, and the Balmer formula for hydrogen, written in terms of frequency, is:

$$\nu_{nr\mu} = cR_\infty \frac{\mu}{m_e} \left(\frac{1}{n_f^2} - \frac{1}{n_i^2} \right), \tag{2.4}$$

where we have included the familiar finite-mass correction, the factor μ/m_e. Here, as throughout the paper, the addition of μ to the subscript indicates that the finite-mass correction is included.

2.2 Stark effect

The perturbation Hamiltonian for the Stark effect is $H_S = eFz$, where F is the magnitude of the electric field, which is taken to be along the z-axis, and $-e$ is the charge of the electron. The natural coordinate system for the Stark effect is not the usual spherical coordinates but is the parabolic coordinates (see, for example, Bethe and Salpeter [BS77]). The parabolic quantum numbers are n, k, and m_ℓ, where n and m_ℓ are the same quantum numbers used in the spherical basis and k is the electric quantum number (in the notation of [BS77], $k = n_1 - n_2$). The orbital angular momentum quantum number ℓ is not good, except for the circular state, which is a basis state in both the spherical basis (with $n, \ell = |m_\ell| = n-1$) and in the parabolic basis (with n, $k=0$, $|m_\ell| = n-1$).

The Stark effect perturbation energy can be found to arbitrarily high order [Sil78]. For our purposes, we only need the Stark effect to second order:

$$E_{S\mu} = \frac{3}{2}e\left(a_0\frac{m_e}{\mu}\right)nkF - \frac{1}{16}\left(a_0\frac{m_e}{\mu}\right)^3 \kappa F^2 n^4(17n^2 - 3k^2 - 9m^2 + 19), \qquad (2.5)$$

where $\kappa = 4\pi\epsilon_0$, $a_0 = (\kappa\hbar^2)/(m_e e^2)$ is the Bohr radius, and we have introduced a factor of m_e/μ for each factor of a_0 to correct for the finite mass of the proton. This finite-mass correction is explained in Appendix A.

A convenient expression for the first-order Stark effect is

$$E^{(1)}_{S\mu}/h \approx 1.920 \times 10^6\, nkF \text{ Hz/(V/cm)}. \qquad (2.6)$$

Circular states have $k = 0$, and the first-order contribution vanishes, so that the lowest-order contribution is the second-order term. The third-order and the fourth-order terms are neglected in Eq. (2.5) because the third-order term vanishes for $k = 0$ and the fourth-order term is negligible ($E^{(4)}_{S\mu}/h = 0.008$ Hz at 1 V/cm for n=30 circular states). For our purposes, the Stark effect for a circular state with principal quantum number n is

$$E_{S\mu} = -\frac{1}{16}\left(a_0\frac{m_e}{\mu}\right)^3 \kappa F^2 n^4(n+1)(4n+5). \qquad (2.7)$$

The contribution that the Stark effect makes to the transition frequency is calculated by finding the difference in $E_{S\mu}$ between the two circular states involved in the transition:

$$\nu^{27\to 28}_{S\mu} = -12\,588.06\, F^2 \text{ Hz/(V/cm)}^2, \qquad (2.8)$$

$$\nu^{29\to 30}_{S\mu} = -17\,799.38\, F^2 \text{ Hz/(V/cm)}^2. \qquad (2.9)$$

The fractional uncertainty in the fundamental physical constants h (7.8×10^{-8}) and a_0 (3.7×10^{-9}) leads to a negligible fraction uncertainty in the numerical values quoted above (7.9×10^{-8}).

We apply an electric field $\vec{F}$ in order to maintain the orientation of the circular states. The applied field overwhelms the residual electric fields in our apparatus. Without this applied field, the orientation of the circular states would likely adiabatically follow the residual fields, which vary in direction as a function of position. The adiabaticity criterion [GL86] is that the rotation rate ω_{rot} of the electric field is less than the Stark frequency $\omega_{Stark} = (2\pi)(3/2)ea_0nF$, which is the splitting between Stark states with $\Delta k = \pm 1$.

The size of the residual fields in our apparatus is approximately 5 mV/cm, and we typically apply a field of about 200 mV/cm. This applied field results in a Stark effect contribution ν_S on the order of 500 Hz. Fortunately, the experiment provides a sensitive measure of the applied electric field F. We measure F by measuring the first order Stark effect of a transition between adjacent "near-circular" states. Sec. 2.7 discusses the frequency contributions for the near-circular state transitions, and Sec. 5.2 discusses this method of measuring the applied electric field.

2.3 Zeeman effect

The Zeeman Hamiltonian is $H_Z = -\vec{\mu}\cdot\vec{B}$, where $\vec{\mu}$ is the total magnetic moment of the atom and $\vec{B}$ is the magnetic field. We break up $\vec{\mu}$ into its components: $\vec{\mu} = \vec{\mu}_\ell + \vec{\mu}_s + \vec{\mu}_i$, and we write $H_Z = H_{Z\ell} + H_{Zs} + H_{Zi}$. The components are due to the orbital motion of the electron, the spin of the electron, and the spin of the proton, respectively. For now we ignore the spin components and deal only with the orbital component of the Zeeman Hamiltonian $H_{Z\ell}$. We do this because it is convenient to deal with the spin components, H_{Zs} and H_{Zi}, in later sections devoted to the fine and hyperfine structure, respectively.

Note that we have omitted the diamagnetic term from the Zeeman Hamiltonian because it is negligible in our experiment. For a magnetic field $B_{\|}$ along the z-axis, the diamagnetic term is [CTDL77]

$$H_D = \frac{e^2}{8m_e} B_{\|}^2 (x^2 + y^2), \tag{2.10}$$

For circular states, the expectation of $x^2 + y^2$ is $\langle x^2 + y^2 \rangle \approx a_0^2 n^4$, and $\langle H_D \rangle$ is approximately

$$\langle H_D \rangle / h \approx 1.50 \times 10^{-4}\, n^4 B_{\|}^2 \frac{\text{Hz}}{\text{Gauss}^2}. \tag{2.11}$$

We apply a field $B_{\|} \approx 150$ mG. For a circular state with $n = 30$, $\langle H_D \rangle / h \approx 0.02$ Hz. The contribution of H_D to a circular state transition frequency is even smaller than 0.02 Hz and can be safely neglected.

2.3.1 Parallel magnetic field

For a magnetic field $B_{\|}$ that is parallel to the electric field (and hence along the z-axis), the Hamiltonian is $H_{Z\ell\|} = -\vec{\mu}_\ell \cdot B_{\|}\hat{z} = -\mu_{\ell,z} B_{\|} = \mu_B (L_z/\hbar) B_{\|}$[CTDL77], where μ_B is the Bohr magneton and L_z is the projection of the orbital angular momentum along the z-axis. The parabolic basis states are eigenstates of L_z and the energy level shift is:

$$E_{Z\ell\|} = \mu_B m_\ell B_{\|}. \tag{2.12}$$

This Zeeman effect removes the m_ℓ degeneracy.

The circular state transitions change the magnetic quantum number m_ℓ such that $\Delta m_\ell = +1$ or $\Delta m_\ell = -1$. Specifically, the quantum numbers describing a circular state transition with $\Delta m_\ell = +1$ are $(n, \ell = n-1, m_\ell = +(n-1)) \rightarrow (n+1, \ell = n, m_\ell = n)$, and for a transition with $\Delta m_\ell = -1$ they are $(n, \ell = n-1, m_\ell = -(n-1)) \rightarrow (n+1, \ell = n, m_\ell = -n)$. Using Eq. 2.12, the contribution to the transition frequency for a transition with $\Delta m_\ell = \pm 1$ is

$$\begin{aligned} \nu_{Z\ell\|} &= \mu_B \Delta m_\ell B_{\|}/h && (2.13) \\ &\approx \pm 1.4 \text{ MHz/G}, && (2.14) \end{aligned}$$

where the ($\pm$) sign depends on the sign of Δm_ℓ. We typically apply a field of $B_\| \approx$ 150 mG, and $\nu_{Z\ell\|} = \pm 211$ kHz. This contribution is large, but we eliminate it by measuring both the $\Delta m_\ell = \pm 1$ transitions. The details of this method for eliminating $\nu_{Z\|}$ are described in Sec. 5.1. We do not include the correction due to the finite mass of the proton in Eq. (2.13) because we eliminate $\nu_{Z\|}$ in such a way that its precise size is not important.

2.3.2 Perpendicular magnetic field

Now we consider the component of the magnetic field $B_\perp$ which is perpendicular to the electric field. We apply a magnetic field $B \approx 150$ mG. The angle between the electric and magnetic fields is less than 0.1 radians, so that $B_\perp < 15$ mG. Without loss of generality, we take $B_\perp$ to lie along the x-axis: $\vec{B} = B_\| \hat{z} + B_\perp \hat{x}$. The Hamiltonian is $H_{Z\ell\perp} = -\mu_{\ell,x} B_\perp = \mu_B (L_x/\hbar) B_\perp$. The parabolic basis states are eigenstates of L_z, so that the perturbation $H_{Z\ell\perp}$ does not produce a first-order effect, i.e., the expectation value of L_x (and hence $H_{Z\ell\perp}$) vanishes.

We go to second-order perturbation theory for $H_{Z\ell\perp}$, which mixes the circular state with the two near-circular states ($|m_\ell| = n-2, k = \pm 1$). They lie above and below the circular state in energy, and the second-order effect cancels to a large extent. However, the cancellation is not exact because the two energy separations are slightly different due to the first-order Zeeman effect. The calculation is lengthy. An approximate result is found in Appendix B, from which we find the contribution to a transition between two circular states with n_i and $n_f = n_i + 1$:

$$\nu_{Z\ell\perp} \approx \pm \frac{-1}{2h} \frac{\mu_B^3 B_\| B_\perp^2}{\left(\frac{3}{2} e a_0 F\right)^2} \left(\frac{n_f - 1}{n_f^2} - \frac{n_i - 1}{n_i^2} \right), \tag{2.15}$$

where the ($\pm$) sign depends on the sign of m_ℓ for the circular states involved. For the various experimental conditions that we use, the size of $\nu_{Z\ell\perp}$ is always less than 3 Hz. Furthermore, because the sign of $\nu_{Z\ell\perp}$ depends on the sign of m_ℓ, it is eliminated in the same way that $\nu_{Z\ell\|}$ is eliminated: by measuring the frequency of both the $\Delta m_\ell = \pm 1$ circular state transitions and then taking the average. We do not include the finite-mass correction to $\nu_{Z\ell\perp}$ in Eq. (2.15) because we eliminate $\nu_{Z\ell\perp}$ in such a way that its precise size is not important.

2.4 Fine structure

We now discuss how the fine structure interaction affects a circular state transition. The electric and magnetic fields that we apply modify the fine structure energy levels in a complicated manner. We discuss these modifications step by step: We first consider the fine structure energy levels in the absence of fields (for which there is an exact solution) in order to evaluate the size of the various terms. Then we consider the fine structure energy levels in a strong electric field and show how the circular state transitions are modified. Finally, we consider how the magnetic field interacts with the electron spin and modifies the circular state transitions. (We have already considered how the magnetic field interacts with the orbital motion of the electron.)

2.4.1 Fine structure energy levels in the absence of fields

We first consider the fine structure in the absence of fields in order to evaluate the size of the various terms for states with high angular momentum. In the absence of fields, the fine structure is given exactly by the Dirac theory[BS77]. The Dirac binding energy is

$$\frac{E_D}{m_e c^2} = \left[1 + \left(\frac{\alpha}{n - j' + \sqrt{j'^2 - \alpha^2}}\right)^2\right]^{-1/2} - 1, \tag{2.16}$$

where $j' = j + 1/2$ and j is the quantum number for the total angular momentum $\vec{J}$ of the electron. ($\vec{J} = \vec{L} + \vec{S}$ where $\vec{S}$ is the spin angular momentum, and $j(j+1)$ is the eigenvalue of $\vec{J}^2$.)

Expanding the Dirac binding energy E_D in powers of α^2, we obtain

$$E_D = hcR_\infty \left[\frac{-1}{n^2} - \frac{\alpha^2}{n^3}\left(\frac{1}{j'} - \frac{3}{4n}\right) - \frac{\alpha^4}{16n^3}\left(\frac{1}{j'^3} + \frac{3}{nj'^2} - \frac{6}{n^2 j'} + \frac{5}{2n^3}\right) + O(\alpha^6)\right]. \tag{2.17}$$

The first term is the non-relativistic binding energy E_{nr}. The second term, which is of order α^2, is the first-order fine structure energy, which we label as $E_D^{(1)}$. For a high angular momentum Rydberg state with $n \approx j \approx 30$, the size of this term is approximately

$$E_D^{(1)}/h \approx -cR_\infty \frac{\alpha^2}{4n^4} \approx -5 \times 10^4 \text{ Hz.} \tag{2.18}$$

The fine structure splitting $\Delta E_D^{(1)}$ between states with $j = \ell \pm 1/2$ when $n \approx j \approx 30$ is

$$\Delta E_D^{(1)}/h \approx cR_\infty \frac{\alpha^2}{n^5} \approx 7 \times 10^3 \text{ Hz.} \tag{2.19}$$

The third term, which is of order α^4, is the second-order fine structure energy, which we label as $E_D^{(2)}$. When $n \approx j \approx 30$, the size of this term is approximately

$$E_D^{(2)}/h \approx -cR_\infty \frac{3\alpha^4}{16n^6} \approx 2 \times 10^{-3} \text{ Hz,} \tag{2.20}$$

which is negligible.

2.4.2 Fine structure energy levels in a "strong" electric field

In our experiment, we apply an electric field $\vec{F}$ in order to maintain the orientation of the circular states (Sec. 2.2). We refer to the field that we apply as "strong" because the Stark interaction is much larger than the first-order fine structure interaction. The strong field criterion is $F \gg F_C$, where F_C is the critical field, i.e., the field for which the fine structure interaction is equal in size to the Stark interaction. We now find the critical field F_C, for a high angular momentum state with $n \approx 30$. We equate the fine structure splitting between states with $\Delta j = 1$, as given in Eq. (2.19), with the first-order Stark splitting between states with $\Delta k = 1$, found from Eq. (2.5) to be $\Delta E_S^{(1)}/h = (3/2)ea_0nF/h \approx 2 \times 10^6 nF$ Hz/(V/cm). The critical field F_C is

$$F_C = \frac{2hcR\alpha^2}{3ea_0n^6} \approx 0.1 \text{ mV/cm.} \tag{2.21}$$

The size of the electric field F that we apply is typically 200 mV/cm, and it clearly satisfies the strong field criterion.

The strong electric field mixes states with different ℓ and j so that we can not use the Dirac theory to find the fine structure. Instead, we use perturbation theory to get the fine structure energy. The unperturbed Hamiltonian is $H_0 = H_{nr} + H_S$. Ignoring the higher-order Stark effects, the eigenstates of H_0 are the parabolic basis states:

$$H_0|nkm_\ell m_s\rangle = \left[-\frac{cR_\infty}{n^2} + \frac{3}{2}e\left(a_0\frac{m_e}{\mu}\right)nkF\right]|nkm_\ell m_s\rangle. \tag{2.22}$$

The perturbation Hamiltonian comes from an expansion of the Dirac equation in $1/c$ [CTDL77], and we include only the terms of order $1/c^2$[CTDL77]:

$$H_{fs} = \underbrace{\frac{-p^4}{8m_e^3c^2}}_{H_{mv}} + \underbrace{\frac{e^2}{2\kappa m_e^2c^2}\frac{1}{r^3}\vec{L}\cdot\vec{S}}_{H_{SO}} + \underbrace{\frac{\pi e^2\hbar^2}{2\kappa m_e^2c^2}\delta(r)}_{H_{Darwin}} + O\left(\frac{1}{c^4}\right). \tag{2.23}$$

The last term, H_{Darwin}, contains a Dirac delta-function and vanishes for states with $l \neq 0$. The first term, H_{mv}, comes from the relativistic variation of the mass, and the second term, H_{SO}, is due to the spin-orbit interaction. Note that in free space, where j is a good quantum number, the first-order perturbation energy of H_{fs} gives exactly the terms of order α^2 in Eq. 2.17. In order to get the terms of order α^4 in Eq. (2.17), we would have to include the terms of order $O(1/c^4)$ in H_{fs}, but we do not because they contribute only $\approx 2 \times 10^{-3}$ Hz to an energy level, as mentioned above.

Because the Stark effect due to the strong electric field lifts the degeneracy between the parabolic states connected by H_{fs}, we do not have to use degenerate first-order perturbation theory. The first-order perturbation energy due to H_{fs} is simply its expectation value:

$$E_{fs}^{(1)} = \langle nkm_\ell m_s|H_{fs}|nkm_\ell m_s\rangle. \tag{2.24}$$

To calculate this expectation value for a given parabolic state, we first decompose the parabolic state into spherical states of different ℓ.

$$|nkm_\ell m_s\rangle = \sum_\ell a_{nkm_\ell\ell}|n\ell m_\ell m_s\rangle, \tag{2.25}$$

where the coefficients $a_{nkm_\ell\ell}$ can be found[Par60] using Clebsch-Gordan coefficients. Because H_{fs} is diagonal in ℓ, the expectation value is just the sum of the contributions from each of the spherical states, without any cross terms:

$$E^{(1)}_{fs} = \sum_\ell |a_{nkm_\ell\ell}|^2\langle n\ell m_\ell m_s|H_{fs}|n\ell m_\ell m_s\rangle. \tag{2.26}$$

The expectation value of H_{fs} for a spherical basis state with $\ell \neq 0$ is calculated in Appendix C.

A circular state is a basis state in both the parabolic and spherical bases:

$$|n; k = 0; m_\ell = \pm(n-1); m_s\rangle = |n; \ell = n-1; m_\ell = \pm(n-1); m_s\rangle. \tag{2.27}$$

For a circular state, the sum in Eq. 2.26 reduces to just one term, and the coefficient $a_{nkm_\ell\ell}$ is equal to one. Using the results from Appendix C, the first-order fine structure energy for a circular state $|n, \ell = n-1, m_\ell = \pm(n-1)\rangle$ is

$$E_{fs\mu} = \underbrace{hcR_\infty \frac{\mu}{m_e}\frac{\alpha^2}{n^3}\left(\frac{3}{4n} - \frac{1}{n-1/2}\right)}_{E_{mv\mu}} + \underbrace{hcR_\infty \frac{\mu}{m_e}\frac{\alpha^2}{n^3}\frac{m_s m_\ell}{n(n-1/2)(n-1)}}_{E_{SO\mu}}, \tag{2.28}$$

where the factor of μ/m_e is the finite-mass correction[Eri77].

The first term $E_{mv\mu}$ is due to the relativistic mass variation, and is a simple energy contribution. For a circular state with $n = 30$

$$E_{mv\mu}/h \approx -6 \times 10^4 \text{ Hz}, \tag{2.29}$$

which is approximately the same size as $E^{(1)}_D$ in Eq. (2.18).

The second term $E_{SO\mu}$ is due to the spin-orbit interaction, and "splits" a state symmetrically into two fine structure states, corresponding to the two spin states

($m_s = \pm 1/2$). We label the energy splitting between the two spin states as $\Delta E_{SO\mu}$, and it is

$$\Delta E_{SO\mu} = hcR_\infty \frac{\mu}{m_e} \frac{\alpha^2 m_\ell}{n^4(n-1/2)(n-1)}. \tag{2.30}$$

For a circular state with $n = 30$ this energy splitting is

$$\Delta E_{SO\mu} \approx 7 \times 10^3 \text{ Hz}, \tag{2.31}$$

which is approximately the same size as $\Delta E_D^{(1)}$ in Eq. (2.19).

The spin-orbit energy $E_{SO\mu}$ is due to the interaction of the electron spin with the magnetic field arising from its motion in the Coulomb field[CTDL77]. We label the effective field that the electron "sees" as $\vec{B}_{SO\mu} = B_{SO\mu}\hat{z}$, and we call it the "spin-orbit field". The energy eigenvalues for a spin in the spin-orbit field are

$$\begin{aligned} E_{SO\mu} &= g_s \mu_B m_s B_{SO\mu} & (2.32)\\ &= 2\mu_B m_s B_{SO\mu}, & (2.33) \end{aligned}$$

where, according to the Dirac theory, we set the electron g-factor equal to 2. (We defer consideration of the anomalous magnetic moment to another section which discusses QED effects.) We find the size of the spin-orbit field by equating this expression for $E_{SO\mu}$ with the expression for $E_{SO\mu}$ in Eq. (2.28):

$$B_{SO\mu} = \frac{hcR_\infty \alpha^2}{2\mu_B} \frac{\mu}{m_e} \frac{1}{n^4(n-1/2)}. \tag{2.34}$$

For a circular state with $n = 30$, the size of $B_{SO\mu}$ is approximately 3 mG.

2.4.3 Transitions with fine structure in a strong electric field

The relativistic variation of the mass makes a simple contribution to the circular state transition frequencies. This contribution is calculated by finding the difference in $E_{mv\mu}$ (Eq. 2.28) between the two circular states involved in the transition:

$$\nu_{fs\mu}^{27\to 28} = 12\,188.30 \text{ Hz} \quad \text{and} \quad \nu_{fs\mu}^{29\to 30} = 8\,527.76 \text{ Hz} \tag{2.35}$$

These values were calculated using $\alpha = 7.297\,352\,533\,(27) \times 10^{-3}$ [MT00]. The uncertainty in α contributes a negligible uncertainty to these values ($< 10^{-4}$ Hz). The main uncertainty in these values for $\nu_{fs\mu}$ comes from the higher-order terms that we dropped. Their size is about 2×10^{-3} Hz, which is negligible.

The spin-orbit interaction splits each circular state into a spin doublet—one state for $m_s = +1/2$ and one state for $m_s = -1/2$. The selection rule for m_s is $\Delta m_s = 0$, and a circular state transition splits symmetrically into two transitions—one transition between states with spin up and one transition between states with spin down. We label the frequency difference between these two transitions as $\Delta\nu_{fs}$ and refer to it as the "fine structure splitting of the transition frequency". Using $E_{SO\mu}$ as given in Eq. (2.28) for the states involved in the transitions, we find that

$$\Delta\nu_{fs\mu}^{27\to 28} = 2\,074.10 \text{ Hz} \quad \text{and} \quad \Delta\nu_{fs\mu}^{29\to 30} = 1\,358.64 \text{ Hz}. \tag{2.36}$$

The uncertainty in these values due to the uncertainty in α is negligible ($\approx 10^{-5}$ Hz). We can write the fine structure splitting of the transition frequency in terms of the spin-orbit field $B_{SO\mu}$:

$$\Delta\nu_{fs\mu} = 2\mu_B \Delta B_{SO\mu}/h, \tag{2.37}$$

where $\Delta B_{SO\mu}$ is the small difference in $B_{SO\mu}$ between the two n-states in the transition. We see that the splitting $\Delta\nu_{fs\mu}$ arises from the difference in the spin-orbit field between the two n-states.

2.4.4 Fine structure in strong electric and magnetic fields

We now introduce the interaction of the electron spin with an external magnetic field. Without loss of generality, we take the perpendicular component of $\vec{B}$ to lie along the x-axis: $\vec{B} = B_{\|}\hat{z} + B_{\perp}\hat{x}$. The external magnetic field modifies the eigenstates of the spin, and hence modifies the spin-orbit interaction, which in the absence of a magnetic field is given by $E_{SO\mu}$ in Eq. (2.28). The expression for fine structure splitting of the transition frequency $\Delta\nu_{fs\mu}$, given in Eq. (2.36), is altered by in a magnetic field. In general, the splitting $\Delta\nu_{fs\mu}$ depends on the size and direction of the magnetic field.

The electron spin "sees" both the external magnetic field $\vec{B}$ and the spin-orbit field $B_{SO\mu}\hat{z}$. In an early incarnation of the experiment, we tried to shield the ambient magnetic fields in order to be in the weak magnetic field limit, $|\vec{B}| \ll B_{SO\mu}$, so that we could safely ignore the effects of $\vec{B}$ on the spin-orbit interaction. However, we found that the size of the residual fields were on the order of $B_{SO\mu}$, resulting in unpredictable dynamics for the electron spin. In the current incarnation of the experiment, we apply a uniform magnetic field $B \approx 150$ mG inside the magnetic shields, which overwhelms the residual fields. The effect of the applied magnetic field is to maintain the orientation of the electron spin. We refer to the applied magnetic field as "strong" because it is much larger than the spin-orbit field: $B \gg B_{SO\mu}$.

We align the coils which produce the magnetic field such that the angle between the applied magnetic field and the electric field is less than 0.1 radians. The magnetic field components are thus: $B_{\|} \approx 150$ mG and $B_{\perp} < 15$ mG. We first consider the effect of $B_{\|}$ on the spin eigenstates and transition frequencies, and then we treat $B_{\perp}$ as a perturbation.

With just the parallel component $B_{\|}$, the electron spin sees a total field of $B'_{\|}\hat{z} = (B_{SO\mu} + B_{\|})\hat{z}$. In this case, the Hamiltonian is $H'_{Zs\|} = 2\mu_B(S_z/\hbar)B'_{\|}$, and the eigenvalues are

$$E'_{Zs\|} = 2m_s\mu_B(B_{SO\mu} + B_{\|}), \tag{2.38}$$

where m_s is the eigenvalue of S_z. The interaction of $B_{\|}$ with the electron spin modifies the energy difference between states with different spin, but has no effect on the transition frequencies because the selection rule for m_s is $\Delta m_s = 0$. In contrast, recall that the spin-orbit field $B_{SO\mu}$ does have an effect on the transition frequencies because it is n-dependent. Thus, with the introduction of $B_{\|}$, the fine structure splitting in the transition frequency is still solely due to the spin-orbit field and is unchanged.

We use perturbation theory to find the effect of $B_\perp$ on the spin eigenstates and transition frequencies. The perturbation Hamiltonian is $H_{Zs\perp} = 2\mu_B(S_x/\hbar)B_\perp$. The eigenstates of the unperturbed Hamiltonian $H'_{Zs\|}$ are $|m_s = \pm 1/2\rangle$ and the eigenvalues are given in Eq. (2.38). The first-order perturbation energy of $H_{Zs\perp}$ vanishes ($E^{(1)}_{Zs\perp} = \langle m_s|H_\perp|m_s\rangle = 2\mu_B B_\perp \langle m_s|S_x|m_s\rangle = 0$) because the expectation of S_x vanishes, and we go to second-order perturbation theory.

The second-order perturbation energy of $H_{Zs\perp}$ is a sum over all other spin states, of which there is only one. The matrix element of $H_{Zs\perp}$ between the two spin states is $\langle m_s{=}\pm 1/2|H_{Zs\perp}|m_s{=}\mp 1/2\rangle = \mu_B B_\perp$, and from Eq. (2.38) the unperturbed energy separation between the two states is, $2\mu_B(B_{SO\mu}+B_\|)$. The second-order perturbation energy is then

$$E^{(2)}_{Zs\perp} = \pm\frac{\mu_B}{2}\frac{B_\perp^2}{B_\| + B_{SO\mu}}, \tag{2.39}$$

where the ($\pm$) sign depends on the spin state: (+) for spin up and (-) for spin down. Of course, $E^{(2)}_{Zs\perp}$ has the effect of repelling the two spin eigenstates; it increases the energy separation by an amount $\mu_B B_\perp^2/(B_\| + B_{SO\mu})$.

We now find the contribution to the transition frequencies due to the effect of $H_{Zs\perp}$ on the spin-orbit interaction. We calculate the difference in $E^{(2)}_{Zs\perp}$ between the two n-states involved in the transition. This difference in $E^{(2)}_{Zs\perp}$, which we label as $\Delta E^{(2)}_{Zs\perp}$, is due to the slight change in the spin-orbit field $B_{SO\mu}$, which depends on n via Eq. (2.34). We approximate $\Delta E^{(2)}_{Zs\perp}$ by differentiating $E^{(2)}_{Zs\perp}$ with respect to $B_{SO\mu}$:

$$\Delta E^{(2)}_{Zs\perp} \approx \mp\frac{\mu_B}{2}\frac{B_\perp^2}{(B_\| + B_{SO\mu})^2}\Delta B_{SO\mu}, \tag{2.40}$$

where $\Delta B_{SO\mu}$ is the change in $B_{SO\mu}$ between the two n-states involved in the transition, and the ($\mp$) sign depends on the spin state. The contribution to the fine structure splitting of the transition frequency is:

$$\Delta\nu_{Zs\perp} \approx -\mu_B\frac{B_\perp^2}{B_\|^2}\Delta B_{SO\mu}/h, \tag{2.41}$$

where we have approximated $B_{\|} + B_{SO\mu}$ as $B_{\|}$. We combine $\Delta\nu_{Zs\perp}$ with the unperturbed splitting $\Delta\nu_{fs\mu}$, as given in Eq. (2.37), in order to get the new splitting, which we label as $\Delta\nu'_{fs\mu}$:

$$\Delta\nu'_{fs\mu} \approx \left(1 - \frac{B_\perp^2}{2B_{\|}^2}\right) 2\mu_B \Delta B_{SO\mu}/h \tag{2.42}$$

$$\approx \left(1 - \frac{B_\perp^2}{2B_{\|}^2}\right) \Delta\nu_{fs\mu} \tag{2.43}$$

The effect of the magnetic field that we apply is to slightly reduce the fine structure splitting of the transition frequency. We align the coils which produce the magnetic field such that $B_\perp < 0.1 B_{\|}$. We (somewhat arbitrarily) take $B_\perp$ to be given by $B_\perp^2 = 0.005(5) B_{\|}^2$, so that the numerical values of the fine structure splitting are

$$\Delta\nu'^{27\to28}_{fs\mu} = 2\,068.9(52)\text{ Hz} \quad\text{and}\quad \Delta\nu'^{29\to30}_{fs\mu} = 1\,355.2(35)\text{ Hz}, \tag{2.44}$$

where the uncertainty is due entirely to the uncertainty in $B_\perp^2$

The resolution of our experiment is such that we do not entirely resolve the splitting $\Delta\nu_{fs\mu}$. We drive circular state transitions for both spin states simultaneously, and the resonance lineshapes are the sum of the spin up contribution and the spin down contribution. If the electron spins are unpolarized, then the transitions for both spin states have equal weights. In this case, the splitting $\Delta\nu_{fs\mu}$ does not bias the centroid of the composite lineshape, because it is symmetric. Thus, the exact size of the splitting, and hence the uncertainty in it, are unimportant to the centroid frequency. However, to the extent that the electron spins become slightly polarized, the size of the splitting becomes important.

In our experiment, we endeavor to populate both the spin up and spin down states equally. From fits of the data, the polarization ψ of the electron is always less than about 0.02. The uncertainty in the fitted centroid frequency depends on the uncertainty in the splitting, but only by an amount reduced by the polarization ψ. Thus, the uncertainty of 5.2 Hz for $\Delta\nu'^{27\to28}_{fs\mu}$ in Eq. (2.44) translates to an uncertainty in the transition frequency of less than about (5.2 Hz)(0.02) = 0.1 Hz, which is negligible.

2.5 Quantum electrodynamics effects

The quantum electrodynamics (QED) effects for the circular states with $n \approx 30$ are small and essentially negligible. Because of this, we ignore the corrections to the QED effects due to the finite mass of the proton. For states with $\ell \neq 0$, there are two lowest-order QED effects [Eri77]: self-energy and anomalous magnetic moment. (The vacuum polarization effect only applies to states with $\ell = 0$. [Eri77])

For states with $\ell \neq 0$, the self-energy contribution is [Eri77]

$$E_{SE} = hcR_\infty \frac{8\alpha^3}{3\pi n^3}\mathcal{L}, \tag{2.45}$$

where $\mathcal{L}$ is the Bethe logarithm. To evaluate the size of $\mathcal{L}$, we use an extrapolation from Ref. [Eri77]

$$\mathcal{L} = \frac{0.1623834}{2\ell+1}\left[\left(\frac{1}{\ell}\right)^{3/2} - \left(\frac{1}{n}\right)^{3/2}\right], \tag{2.46}$$

which has a fractional uncertainty of [Eri77]

$$\frac{d\mathcal{L}}{\mathcal{L}} = \frac{1}{2} - \frac{1}{4}\left(\frac{\ell+1}{n}\right)^{3/2}. \tag{2.47}$$

This fractional uncertainty in $\mathcal{L}$ is quite large (= 1/4 for circular states with $\ell = n-1$). However, this is not a problem because E_{SE} turns out to be negligible. For a circular state with $n = 30$, $E_{SE}/h \approx 0.035$ Hz, and the contribution to the frequency of a circular state transition is even smaller. For the $n = 29 \to 30$ transition, $\nu_{SE} \approx 0.01$ Hz, which is a fractional contribution of only 4×10^{-14}.

The anomalous magnetic moment of the electron is the largest QED effect for circular states with $n \approx 30$. In Dirac theory, the g-factor of the electron is $g_e = 2$. QED modifies the g-factor: $g_e = 2(1 + a_e)$ where to lowest order $a_e = \alpha/2\pi$. The anomalous magnetic moment contributes only to the symmetric fine structure splitting of the transition frequency $\Delta\nu'_{fs\mu}$. The expression for the fine structure splitting as given in Eq. (2.43) becomes

$$\Delta\nu'_{fs\mu+anom} \approx \left(1 + \frac{\alpha}{2\pi}\right)\left(1 - \frac{B_\perp^2}{2B_\parallel^2}\right)\Delta\nu_{fs\mu}. \tag{2.48}$$

The anomalous magnetic moment fractionally increases the splitting by about 1.2×10^{-3}.

2.6 Hyperfine structure

The interaction of the proton magnetic moment and the total electron magnetic moment causes hyperfine structure, and this structure is roughly a factor of m_e/m_p smaller than the spin-orbit fine structure. For the circular state transitions that we drive this structure is on the order of 1 Hz, and is well below the resolution of our apparatus. We have no reason to believe that the proton magnetic moment is polarized, so the structure should be symmetric and thus cause no net contribution.

2.7 Near-circular state transitions

In order to calculate the second-order Stark effect on circular state transitions, we measure the electric field by measuring the first-order Stark effect on "near-circular" state transitions. The near-circular state transitions that we drive are described by these quantum numbers:

$$(n_i; k = 1; |m_\ell| = n_i - 1; m_s) \rightarrow (n_f; k = 1; |m_\ell| = n_f - 1; m_s), \tag{2.49}$$

where $n_f = n_i + 1$ and $n_i = 27$ or 28. In this section, we discuss the frequency contributions to the near-circular state transitions which are necessary for our measurement of the first-order Stark effect. We consider each term in the Hamiltonian as given in Eq. (2.1). To set the scale for significant interactions, we determine the near-circular state transition frequency to about 100 Hz, and contributions which are less than 10

Hz are considered negligible.

The main contribution comes from the Balmer formula, given in Eq. (2.4). This contribution depends only on the principal quantum number and is the same for both circular and near-circular state transitions.

We use Eq. (2.5) for both states involved in order to find the Stark effect contribution to a near-circular state transition.

$$\nu_{S\mu}^{27\to 28} = 1\,920\,363\,F \text{ Hz/(V/cm)} - 13\,352\,F^2 \text{ Hz/(V/cm)}^2, \tag{2.50}$$

$$\nu_{S\mu}^{29\to 30} = 1\,920\,363\,F \text{ Hz/(V/cm)} - 18\,814\,F^2 \text{ Hz/(V/cm)}^2. \tag{2.51}$$

Note that the first-order Stark effect is the same for any near-circular state transition. We do not include the third-order Stark effect because it is negligible (less than 7 Hz at a field of 2 V/cm).

We eliminate the Zeeman effect for the near-circular state transitions in the same way as for the circular state transitions. We measure measure both the $\Delta m_\ell = \pm 1$ circular state transitions and take the average.

To calculate the fine structure contribution to the near-circular state energy levels, we decompose the near-circular state into spherical basis states and use the expectation values of H_{fs} as calculated in Appendix C. The results are

$$E_{mv\mu} = hcR_\infty \frac{\mu}{m_e}\frac{\alpha^2}{n^3}\left(\frac{3}{4n} - \frac{n-1}{(n-3/2)(n-1/2)}\right), \tag{2.52}$$

$$E_{SO\mu} = hcR_\infty \frac{\mu}{m_e}\frac{\alpha^2}{n^3} m_s \frac{n(n-1/2)+(n-3/2)(n-2)}{2n(n-1/2)(n-1)(n-3/2)}. \tag{2.53}$$

To find the effect of the relativistic mass variation on the near-circular transition, we use Eq. (2.52) for both n states involved:

$$\nu_{fs\mu}^{27\to 28} = 13\,298 \text{ Hz} \quad \text{and} \quad \nu_{fs\mu}^{29\to 30} = 9\,251 \text{ Hz}. \tag{2.54}$$

Next we find the fine structure splitting of the transition frequency $\Delta\nu_{fs\mu}$, which is due to the spin-orbit energy $E_{SO\mu}$ as given by Eq. (2.53). Recall that $\Delta\nu_{fs\mu}$ is the frequency difference between the transition with spin up ($m_s = +1/2$) and the transition with spin down ($m_s = -1/2$). We ignore the effects of the magnetic field on the spin-orbit energy because it contributes less than 10 Hz to the splitting. The splittings are

$$\Delta\nu_{fs\mu}^{27\to 28} = 2\,125 \text{ Hz} \quad \text{and} \quad \Delta\nu_{fs\mu}^{29\to 30} = 1\,389 \text{ Hz}. \tag{2.55}$$

The QED effects and the hyperfine structure contribute less than 10 Hz to the near-circular state transitions and are negligible.

Chapter 3

Time-Resolved Ramsey Resonance: Lineshape and Fitting Procedure

In this section we discuss our model of the lineshape for time-resolved Ramsey resonance and our procedure for fitting the data. First, we discuss some important points about the nature of the lineshape. Then, we describe the ideal Ramsey resonance lineshape and our basic lineshape model and fitting procedure. Then we consider modifications to the basic lineshape model due to a more realistic description of the oscillatory fields and the effects of shifts in the resonance frequency while the atoms interact with the oscillatory fields. Finally, we discuss effects which arise because we do not have a perfect two-level system and because of imperfections in our detection apparatus.

3.1 Nature of the lineshape

In typical atomic beam resonance experiments, the lineshape is written as $P_{i,f}(\omega)$, which is the transition probability as a function of the radiation frequency ω. We prefer to write the lineshape in terms of the "inversion", defined as $I(\omega) = 2P_{i,f}(\omega) - 1$. As discussed later in this chapter, the inversion is the vertical component of the Bloch vector.

Also, in typical atomic beam resonance experiments, the lineshape represents an average over the velocity distribution of the atomic beam—in other words, an average over the transit time distribution. The transit time is the time $\mathcal{T}$ that it takes for an atom with velocity v to travel the length $\mathcal{L}$ of the atomic beam ($\mathcal{T} = \mathcal{L}/v$). In our experiment, we define the transit time to be the time from production to detection. We produce the atoms in a pulsed fashion, and we measure the transit time for each atom. Consequently, we can analyze our lineshape in terms of the transit time, i.e., we can analyze a set of time-resolved lineshapes rather than one transit-time-averaged lineshape.

Experimentally, we count the number of atoms in the initial and final states, $C^i(\omega)$ and $C^f(\omega)$, as a function of the radiation frequency ω. We separate the counts into several time bins of width $\mathcal{T}_{bin}$, in order to form a time-resolved set of experimental lineshapes. Thus, we can analyze the experimental lineshape for each time bin individually. The j-th time bin contains the number of atoms in the initial and final states $C^i_j(\omega)$ and $C^f_j(\omega)$ as a function of frequency ω for atoms with transit times $\mathcal{T}$ satisfying $\mathcal{T}_j - \mathcal{T}_{bin}/2 < \mathcal{T} < \mathcal{T}_j + \mathcal{T}_{bin}/2$, where $\mathcal{T}_j$ is the center time of the j-th time bin. For the j-th time bin, the experimental lineshape $I_{exp,j}(\omega)$ is

$$I_{exp,j}(\omega) = \frac{C^f_j(\omega) - C^i_j(\omega)}{C^f_j(\omega) + C^i_j(\omega)}. \tag{3.1}$$

3.2 Two-level resonance and the Bloch vector

In this section, we lay out the basics of two-level resonance in terms of the Bloch vector for $\Delta m_\ell = \pm 1$ electric dipole transitions.

3.2.1 Wavefunction, matrix elements, and expectation values

We write the initial and final states as $|b\rangle$ and $|a\rangle$. The two states have energies $\hbar\omega_b$ and $\hbar\omega_a$, respectively. We write the wavefunction of an atom as

$$|\psi\rangle = Ae^{-i\omega_a t}|a\rangle + Be^{-i\omega_b t}|b\rangle, \tag{3.2}$$

where $A = ae^{-i\phi_a}$, $B = be^{-i\phi_b}$. We label the transition frequency as $\omega_0 = \omega_a - \omega_b$ and the phase between the states as $\phi_0 = \phi_a - \phi_b$,

From Bethe and Salpeter, Eq. 65.2 [BS77], we can find the matrix elements between adjacent circular states. In the limit of large principal quantum number n, for circular state transitions with $\Delta m_\ell = \pm 1$, the matrix elements of the position operators x, y, and z are (where $x_{ab} = \langle a|x|b\rangle$)

$$\begin{aligned} x_{ab} &= \frac{1}{2}a_0 n^2, & (3.3)\\ y_{ab} &= \mp\frac{i}{2}a_0 n^2, & (3.4)\\ z_{ab} &= 0, & (3.5) \end{aligned}$$

where the ($\mp$) sign depends on the sign of Δm_ℓ, a_0 is the Bohr radius, and n is the principal quantum number of the initial state.

We write the electric dipole operator as $\vec{p} = -e\vec{r}$, where e is the proton charge and $\vec{r}$ is the position operator. The expectation values of the cartesian components of the electric dipole operator are $\langle\psi|p_x|\psi\rangle$, $\langle\psi|p_y|\psi\rangle$, and $\langle\psi|p_z|\psi\rangle$. We can write them in terms of A and B and alternatively in terms of a, b, and ϕ_0:

$$\begin{aligned} \langle p_x\rangle &= -ex_{ab}2\mathrm{Re}\left[A^*Be^{i\omega_0 t}\right] = -2ex_{ab}ab\cos\left(\omega_0 t + \phi_0\right), & (3.6)\\ \langle p_y\rangle &= \mp ex_{ab}2\mathrm{Im}\left[A^*Be^{i\omega_0 t}\right] = \mp 2ex_{ab}ab\sin\left(\omega_0 t + \phi_0\right), & (3.7)\\ \langle p_z\rangle &= 0, & (3.8) \end{aligned}$$

where the ($\mp$) sign depends on the sign of Δm_ℓ. The expectation value $\langle\vec{p}\rangle$ rotates in the x-y (horizontal) plane. As viewed from above, it rotates counter-clockwise for $\Delta m_\ell = +1$ and clockwise for $\Delta m_\ell = -1$.

3.2.2 Form of the perturbation V

We now consider the form of the resonant perturbation V for $\Delta m_\ell = \pm 1$ electric dipole transitions. The perturbation Hamiltonian is given by $V = -\vec{p}\cdot\vec{E}$, where $\vec{p}$ is the dipole operator and $\vec{E}$ is the oscillating electric field. If we take the electric field to have amplitudes E_x and E_y (E_z is irrelevant), then we can write V in the following form:

$$V = e\left[xE_x\cos(\omega t+\phi_x) + yE_y\sin(\omega t+\phi_y)\right] = e\left[r^+E^-(t) + r^-E^+(t)\right], \qquad (3.9)$$

where x and y are position operators and the quantities $r^\pm$ and $E^\pm(t)$ are complex and given by

$$\begin{aligned} r^\pm &= \frac{1}{\sqrt{2}}(x \pm iy) && (3.10) \\ E^\pm(t) &= \frac{1}{\sqrt{2}}\left[E_x\cos(\omega t+\phi_x) \pm iE_y\sin(\omega t+\phi_y)\right] && (3.11) \end{aligned}$$

We can rewrite $E^\pm$(t) in terms of the circular basis:

$$E^\pm(t) = \frac{1}{2}\left[E_+e^{\pm i(\omega t+\phi_+)} + E_-e^{\mp i(\omega t+\phi_-)}\right], \qquad (3.12)$$

where, as in Eq. (6.1), $E_+e^{-i\phi_+}$ and $E_-e^{-i\phi_-}$ are the complex amplitudes for the circular basis. (Note the distinction between the $E^\pm(t)$ and $E_\pm$ variables.)

Using Eqs. (3.3–3.5) for the position matrix elements gives the matrix elements of $r^\pm$:

$$r^+_{ab} = r^-_{ba} = \begin{cases} \sqrt{2}x_{ab} & : \quad \Delta m_\ell = +1 \\ 0 & : \quad \Delta m_\ell = -1 \end{cases} \qquad (3.13)$$

$$r^-_{ab} = r^+_{ba} = \begin{cases} 0 & : \quad \Delta m_\ell = +1 \\ \sqrt{2}x_{ab} & : \quad \Delta m_\ell = -1 \end{cases} . \tag{3.14}$$

Using the matrix elements for $r^\pm$ and Eq. (3.9), the perturbation matrix elements are

$$V_{ab} = \sqrt{2}ex_{ab}E^{\mp}(t) \tag{3.15}$$

$$V_{ba} = \sqrt{2}ex_{ab}E^{\pm}(t), \tag{3.16}$$

where the $(\mp)$ and $(\pm)$ signs depend on Δm_ℓ.

3.2.3 The Bloch vector: definition, dynamics, interpretation

Now we introduce the Bloch vector picture and we derive the equation of motion for the Bloch vector subject to an oscillatory perturbation. Although most of the material in this section is well known,[FVH57] we rederive it here because we need to firmly establish the conventions for sign, phase, direction of rotation, et cetera. In addition, we need to keep some parameters slightly more general than in reference [FVH57].

We use the Bloch vector picture [FVH57] to describe the atomic wavefunction and its evolution under the perturbation V due to the resonant electric field. The Bloch vector picture is a geometrical description of a single two state system or a collection of non-interacting two-state systems. In the Bloch vector picture, the Schrödinger equation is transformed into a real three-dimensional equation: $\dot{\vec{s}} = \vec{\Omega} \times \vec{s}$, where $\vec{s}$ specifies the wavefunction and $\vec{\Omega}$ represents the perturbation. In the case of a spin $\frac{1}{2}$ system, the Bloch vector $\vec{s}$ is the expectation value of the spin and $\vec{\Omega}$ is proportional to the magnetic field. In our case, we have $\Delta m_\ell = \pm 1$ electric dipole transitions, and the vectors $\vec{s}$ and $\vec{\Omega}$ have different interpretations.

We first consider the Bloch vector in the lab frame and then in the frame rotating at the perturbation frequency. Then we consider the dynamics and the interpretation of the Bloch vector picture for $\Delta m_\ell = \pm 1$ electric dipole transitions.

Definition of the Bloch vector

In the lab frame, we label the components of the Bloch vector as $\vec{s}\,' = (s_1', s_2', s_3')$. We define the horizontal components, s_1' and s_2', to be proportional to the horizontal components of the expectation value of the electric dipole moment as given in Eqs. (3.6–3.7), and we define the vertical component s_3' to be the inversion of the two level system:

$$\begin{aligned} s_1' &= -2Re\left[A^* B e^{i\omega_0 t}\right] && (3.17) \\ s_2' &= \mp 2Im\left[A^* B e^{i\omega_0 t}\right] && (3.18) \\ s_3' &= A^*A - B^*B, && (3.19) \end{aligned}$$

where the $(\mp)$ sign depends on Δm_ℓ and A and B are the upper and lower state amplitudes, as in Eq. (3.2). The Bloch vector is of unit length when $|\psi\rangle$ is normalized: $\sqrt{s_1'^2 + s_2'^2 + s_3'^2} = A^*A + B^*B = 1$. Given the normalization, it only takes two parameters to specify the Bloch vector—the polar and azimuthal angles θ and ϕ, for example. In the absence of a perturbation, A and B are constant, and $\vec{s}\,'$ simply precesses around the vertical axis at the transition frequency ω_0, with the vertical component s_3' remaining constant.

When subject to a oscillating perturbation, the dynamics of the Bloch vector are easier to visualize and solve in a frame rotating at a frequency ω_r at or near the perturbation frequency ω. In the frame rotating at ω_r, the components of the Bloch vector $\vec{s}$ are (simply multiplying the horizontal components of $\vec{s}\,'$ by $e^{-i(\omega_r t + \phi_r)}$):

$$\begin{aligned} s_1 &= -2Re\left[A^* B e^{-i(\Delta_{0r} t + \phi_r)}\right] && (3.20) \\ s_2 &= \mp 2Im\left[A^* B e^{-i(\Delta_{0r} t + \phi_r)}\right] && (3.21) \\ s_3 &= A^*A - B^*B, && (3.22) \end{aligned}$$

where $\Delta_{0r} = \omega_r - \omega_0$ and the $(\mp)$ sign depends on Δm_ℓ. If the frame is rotating at the resonance frequency ($\Delta_{0r} = 0$) then, in the absence of a perturbation, $\vec{s}$ does not move. (Usually, the frequency of the rotating frame is set equal to the frequency of the perturbation: $\omega_r = \omega$, but we do not do this right away because we need a more general result for use in chapter 6.)

Equation of motion for the Bloch vector

To find the dynamics of $\vec{s}$ given a resonant perturbation V with matrix elements $V_{ab} = V_{ba}^* = \langle a|V|b\rangle$ and $V_{aa} = V_{bb} = 0$, we use the Schrödinger equation which gives

$$
\begin{aligned}
i\hbar\dot{A} &= Be^{i\omega_0 t}V_{ab} && (3.23)\\
i\hbar\dot{B} &= Ae^{-i\omega_0 t}V_{ba}. && (3.24)
\end{aligned}
$$

Using Eqs. (3.23–3.24) to find the differential equation for $\vec{s}$ gives the simple result:

$$\dot{\vec{s}} = \vec{\Omega} \times \vec{s}, \qquad (3.25)$$

where $\vec{\Omega}$ has three real components:

$$
\begin{aligned}
\Omega_1 &\equiv \mp 2Re\left[\frac{V_{ba}}{\hbar}e^{-i(\omega_r t+\phi_r)}\right] && (3.26)\\
\Omega_2 &\equiv -2Im\left[\frac{V_{ba}}{\hbar}e^{-i(\omega_r t+\phi_r)}\right] && (3.27)\\
\Omega_3 &\equiv \mp\Delta_{0r}, && (3.28)
\end{aligned}
$$

where the ($\mp$) sign depends on Δm_ℓ. We refer to $\vec{\Omega}$ as the pseudo-torque because it rotates the Bloch vector according to Eq. (3.25). The Bloch vector precesses around the instantaneous direction of $\vec{\Omega}$ with angular velocity $|\vec{\Omega}|$.

The pseudo-torque $\vec{\Omega}$

Plugging the matrix elements from Eqs. (3.2.2) into Eqs. (3.2.3) gives,

$$\Omega_1 = \mp 2\sqrt{2}ex_{ab}Re\left[\frac{E^\pm}{\hbar}e^{-i(\omega_r t+\phi_r)}\right] \qquad (3.29)$$

$$\Omega_2 = -2\sqrt{2}ex_{ab}Im\left[\frac{E^{\pm}}{\hbar}e^{-i(\omega_r t+\phi_r)}\right] \tag{3.30}$$

$$\Omega_3 = \mp\Delta_{0r}, \tag{3.31}$$

where the ($\pm$) and ($\mp$) signs depend on Δm_ℓ. If we: replace the $E^{\pm}$ in these equations with the expression in Eq. (3.12), take the rotating wave approximation, and define the Rabi frequency to be

$$\omega_{R\pm} \equiv \sqrt{2}ex_{ab}E_{\pm}/\hbar, \tag{3.32}$$

then these equations for $\vec{\Omega}$ become

$$\Omega_1 = \mp\omega_{R\pm}\cos(\Delta_r t + \phi_{r\pm}) \tag{3.33}$$

$$\Omega_2 = -\omega_{R\pm}\sin(\Delta_r t + \phi_{r\pm}) \tag{3.34}$$

$$\Omega_3 = \mp\Delta_{0r}, \tag{3.35}$$

where $\Delta_r = \omega - \omega_r$ is the detuning of the radiation frequency from the rotating frame frequency, $\phi_{r\pm} = \phi_{\pm} - \phi_r$ is the phase of the field with respect to the phase of the rotating frame, $\Delta_{0r} = \omega_r - \omega_0$ is the detuning of the rotating frame frequency from the resonance frequency, and the $\pm$ and $\mp$ signs depend on Δm_ℓ.

For the $\Delta m_\ell = +1$ transition, the pseudo-torque is given by $\vec{\Omega} = (-\omega_{R+}\cos(\Delta_r t + \phi_+), -\omega_{R+}\sin(\Delta_r t + \phi_+), -\Delta_{0r})$. Here the first two components are the negative of the x and y components of the field in the rotating frame. For the $\Delta m_\ell = -1$ transition, the pseudo-torque is given by $\vec{\Omega} = (\omega_{R-}\cos(\Delta_r t + \phi_-), -\omega_{R-}\sin(\Delta_r t + \phi_-), \Delta_{0r})$. In this case, *the first two components are equal to the x and y components of the field* in the rotating frame.

Frame rotating at the perturbation frequency

So far, we have kept arbitrary the frequency of the rotating frame, ω_r. We have done this to get a more general result for use in chapter 6. We now go to the frame rotating at the frequency of the perturbation where

$$\omega_r = \omega. \tag{3.36}$$

We take the phase of the rotating frame such that the pseudo torque lies along the x-axis:

$$\phi_r = \begin{cases} \phi_+ + \pi & : \quad \Delta m_\ell = +1 \\ \phi_- & : \quad \Delta m_\ell = -1 \end{cases} \tag{3.37}$$

The π is needed for the $\Delta m_\ell = +1$ transition because the azimuthal phase of the pseudo torque is opposite the phase of the electric field. The pseudo torque in this frame is very simple:

$$\Omega_1 = \omega_{R\pm} \tag{3.38}$$

$$\Omega_2 = 0 \tag{3.39}$$

$$\Omega_3 = \mp\Delta, \tag{3.40}$$

where $\Delta = \omega - \omega_0$ is the detuning of the perturbation from resonance. The relationship between the Bloch vector and the A and B coefficients is given by

$$s_1 = \pm 2Re\left[A^* B e^{-i(\Delta t + \phi_\pm)}\right] \tag{3.41}$$

$$s_2 = 2Im\left[A^* B e^{-i(\Delta t + \phi_\pm)}\right] \tag{3.42}$$

$$s_3 = A^* A - B^* B. \tag{3.43}$$

Visualizing the Bloch vector dynamics

The main benefit of the Bloch vector picture is that it is easy to visualize the motion of the Bloch vector. The Bloch vector equation of motion, $\dot{\vec{s}} = \vec{\Omega} \times \vec{s}$, is difficult to solve in general. For all but the simplest problems, the equation of motion must be integrated numerically. However, the Bloch vector picture can be used to visualize a difficult problem and gain insight into the problem.

The most basic motion of the Bloch vector s occurs if the direction of the pseudo torque $\vec{\Omega}$ is constant. In this case, the Bloch vector precesses around $\vec{\Omega}$ at the "effective Rabi frequency" $\Omega = |\vec{\Omega}| = \sqrt{\omega_{R\pm}^2 + \Delta_{0r}^2}$. where Δ_{0r} is defined after Eq. (3.35). Evolving the Bloch vector from time t_1 to time t_2, it rotates through a total angle of

$$\alpha = \int_{t_1}^{t_2} dt\, \Omega. \tag{3.44}$$

If the magnitude of Ω is also constant, then the angle is $\alpha = \Omega(t_2 - t_1)$. The rotation may be written as

$$\vec{s}(t_2) = \mathcal{R}(\hat{\Omega}, \alpha)\vec{s}(t_1) \tag{3.45}$$

where $\mathcal{R}(\hat{\Omega}, \alpha)$ is an operator denoting a right handed rotation about the direction $\hat{\Omega}$ through an angle α. In the frame rotating such that $\hat{\Omega}$ lies in the x-z plane, the direction of Ω can be specified by the angle χ between $\hat{\Omega}$ and the x-axis:

$$\sin\chi = \frac{\mp\Delta}{\Omega}, \quad \cos\chi = \frac{\omega_{R\pm}}{\Omega}. \tag{3.46}$$

With this definition of χ, $\mathcal{R}(\hat{\Omega}, \alpha)$ can be written in matrix form as

$$\mathcal{R}(\hat{\Omega}, \alpha) = \begin{bmatrix} \cos^2\chi + \sin^2\chi\ \cos\alpha & -\sin\chi\ \sin\alpha & \sin\chi\ \cos\chi\ (1 - \cos\alpha) \\ \sin\chi\ \sin\alpha & \cos\alpha & -\cos\chi\ \sin\alpha \\ \sin\chi\ \cos\chi(1 - \cos\alpha) & \cos\chi\ \sin\alpha & \sin^2\chi + \cos^2\chi\ \cos\alpha \end{bmatrix} \tag{3.47}$$

Four special cases of Eq. 3.47 are of interest. First, if $\Delta = 0$, then $\mathcal{R}(\hat{\Omega}, \alpha)$ is a rotation about the x axis, $\mathcal{R}(\hat{x}, \alpha)$, where

$$\mathcal{R}(\hat{x}, \alpha) = \begin{bmatrix} 1 & 0 & 0 \\ 0 & \cos\alpha & -\sin\alpha \\ 0 & \sin\alpha & \cos\alpha \end{bmatrix}, \tag{3.48}$$

and α is given by Eq. (3.44) with $\Omega = \omega_R$. The second case is if $\omega_R = 0$. Then

$\mathcal{R}(\hat{\Omega},\alpha)$ is a rotation about the z-axis, $\mathcal{R}(\hat{z},\alpha)$, where

$$\mathcal{R}(\hat{z},\alpha) = \begin{bmatrix} \cos\alpha & \pm\sin\alpha & 0 \\ \mp\sin\alpha & \cos\alpha & 0 \\ 0 & 0 & 1 \end{bmatrix}. \tag{3.49}$$

The third important case is if $\vec{\Omega}$ is constant. This corresponds to a pulse of radiation that is constant in time with constant detuning Δ and Rabi frequency $\omega_{R\pm}$. In this case, $\mathcal{R}(\hat{\Omega},\alpha)$ is given by Eq. (3.47) with $\alpha = \Omega(t_2 - t_1)$. The fourth case is if $|\Delta| \ll \omega_{R\pm}$. In this case we can take $\sin\chi \approx \mp\Delta/\omega_R$ and $\cos\chi \approx 1$ and Eq. (3.47) becomes

$$\mathcal{R}(\hat{\Omega},\alpha) \approx \begin{bmatrix} 1 & \pm\frac{\Delta}{\omega_R}\sin\alpha & \mp\frac{\Delta}{\omega_R}(1-\cos\alpha) \\ \mp\frac{\Delta}{\omega_R}\sin\alpha & \cos\alpha & -\sin\alpha \\ \mp\frac{\Delta}{\omega_R}(1-\cos\alpha) & \sin\alpha & \cos\alpha \end{bmatrix}, \tag{3.50}$$

where $\alpha = \Omega(t_2 - t_1) \approx \omega_R(t_2 - t_1)$.

3.3 Ideal Rabi resonance lineshape

In the Rabi resonance method, the atoms start in the initial state and travel with velocity v. They encounter a region of length l where they "see" a field oscillating at ω which couples the two states. The oscillatory field is on for a time $\tau = l/v$. After the atoms pass through the oscillatory field region, their inversion is measured.

In terms of the Bloch vector, the Rabi resonance method is represented as

$$\vec{s}(t=\tau) = \mathcal{R}(\hat{\Omega},\Omega\tau)\ \vec{s}(t=0), \tag{3.51}$$

where $\vec{\Omega} = (\omega_{R\pm}, 0, \mp\Delta)$. We write the lineshape $I(\omega)$ in terms of the inversion, which is the z-component of $\vec{s}$. If the atoms start out in the lower state, then the initial

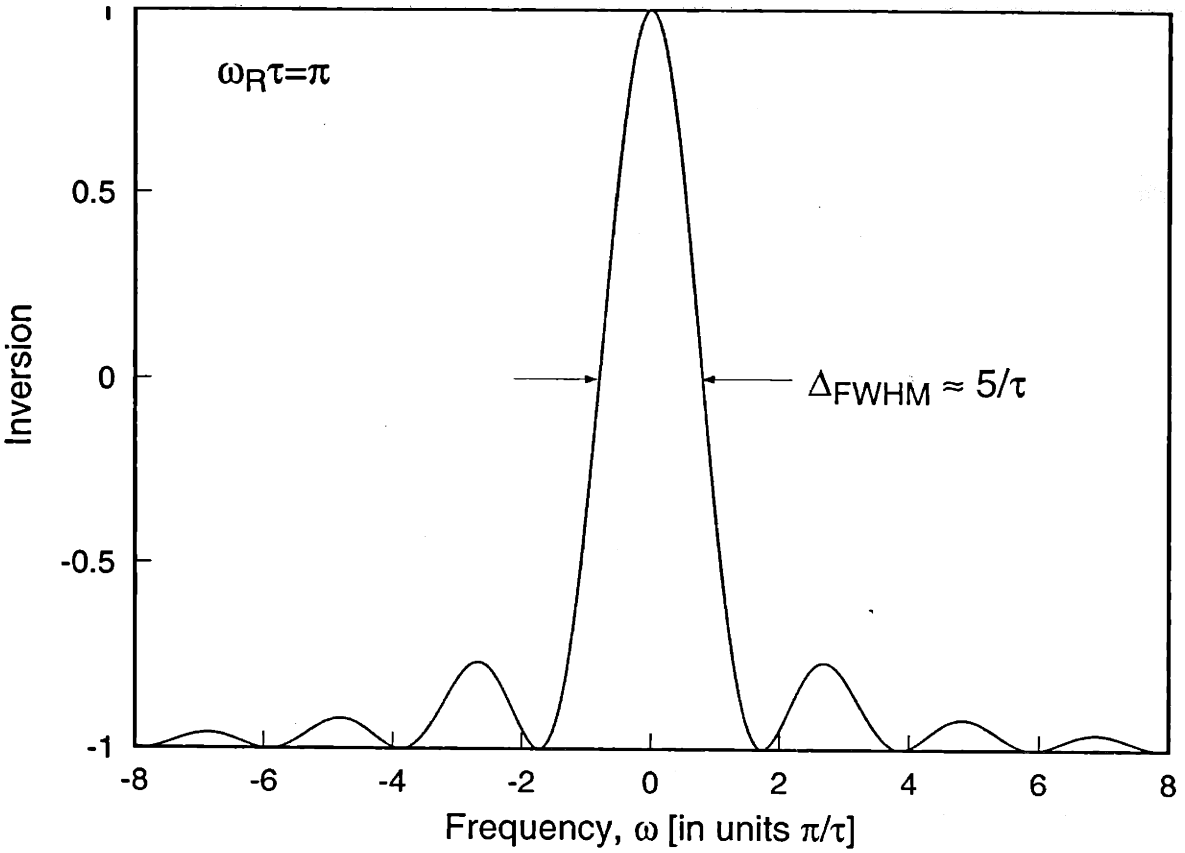

Figure 3-1: Rabi resonance lineshape, Eq. (3.53). The interaction time τ was chosen such that $\omega_R\tau = \pi$, yielding the maximum amplitude for the lineshape.

state is given by $\vec{s}(t = 0) = (0, 0, -1)$ and the inversion after time $t = \tau$ is

$$I(\omega) = -\sin^2\chi - \cos^2\chi\ \cos(\Omega\tau). \tag{3.52}$$

Using the definition of χ from Eq. (3.46), the lineshape is:

$$I(\omega) = -\frac{\Delta^2 + \omega_{R\pm}^2 \cos\left(\sqrt{\omega_{R\pm}^2 + \Delta^2}\ \tau\right)}{\omega_{R\pm}^2 + \Delta^2} \tag{3.53}$$

Note that this does not depend on the sign of Δm_ℓ: the lineshape is the same for both $\Delta m_\ell = +1$ and $\Delta m_\ell = -1$ transitions. Figure 3-1 shows the Rabi resonance lineshape as given in Eq. (3.53) for a π pulse, which gives the maximum amplitude.

The linewidth of the resonance is $\Delta_{FWHM} \approx 5/\tau$, in terms of angular frequency.

To decrease the linewidth and improve the precision of the Rabi method, we would have to increase the interaction time τ. With the velocity distribution of the atomic beam as a given, the way to increase τ is to lengthen the interaction region. However, it becomes impractical to maintain a uniform interaction region over a large distance. The Ramsey resonance method[Ram56] provides a practical technique for reducing the linewidth, and we turn to it next.

3.4 Ideal Ramsey resonance lineshape

In the Ramsey resonance method, the atoms start in the initial state and travel with velocity v. They first encounter a region of length l where they "see" a field oscillating at ω which couples the two states. They then travel a distance $L \gg l$ for which there is no oscillatory field. Finally, they again encounter a region of length l where they see another oscillatory field. In terms of time, the oscillatory field is on for a time τ, off for a time $T \gg \tau$ and then on again for a time τ. The relation between the lengths and times is given by $L = vT$ and $l = v\tau$. After the atoms pass through the second oscillatory field region, their inversion is measured.

In terms of the Bloch vector, the Ramsey resonance method is represented as

$$\vec{s}(t = T + 2\tau) = \mathcal{R}(\hat{\Omega}, \Omega\tau)\ \mathcal{R}(\hat{z}, \mp(\Delta T - \phi_0))\ \mathcal{R}(\hat{\Omega}, \Omega\tau)\ \vec{s}(t = 0). \tag{3.54}$$

Starting from the right, the first rotation represents the action of the first oscillatory field. The second rotation $\mathcal{R}(\hat{z}, \mp(\Delta T + \phi_\pm))$ corresponds to both the phase evolution of the atomic dipole moment, ΔT, and the phase difference between the two oscillatory fields:

$$\phi_0 = \phi_1 - \phi_2, \tag{3.55}$$

where ϕ_1 and ϕ_2 are the phases of the first and second oscillatory fields, respectively. The $\mp$ sign depends on the sign of Δm_ℓ and is for the different sense of rotation between the two transitions. The rotation through ϕ_0 takes the Bloch vector from the rotating frame appropriate to the first oscillatory field to the rotating frame appropriate to the second oscillatory field. Finally, the third rotation represents the action of the second oscillatory field, which is characterized by the same Rabi frequency and duration as the first.

If the atoms start out in the lower state, then the initial state is given by $\vec{s}(t = 0) = (0, 0, -1)$ and the inversion after time $t = T + 2\tau$ is

$$\begin{aligned} I(\omega) = \; & \cos^2\chi\Big\{-\sin^2\chi\,[1-\cos(\Omega\tau)]^2\cos(\Delta T-\phi_0) \\ & \qquad \mp 2\sin\chi\,\sin(\Omega\tau)\,[1-\cos(\Omega\tau)]\sin(\Delta T-\phi_0) \\ & \qquad + \sin^2(\Omega\tau)\cos(\Delta T-\phi_0)\Big\} \\ & - \Big[\sin^2\chi+\cos^2\chi\cos(\Omega\tau)\Big]^2 \end{aligned} \tag{3.56}$$

Note that this does not depend on the sign of Δm_ℓ. Although there is a $\mp$ sign, $\sin\chi$ has the same $\mp$ dependence so that they cancel. Thus, the lineshape is the same for both $\Delta m_\ell = +1$ and $\Delta m_\ell = -1$ transitions. Figure 3-2 shows the Ramsey resonance lineshape as given in Eq. (3.56) for $\omega_R\tau = \pi/2$, which gives the maximum amplitude. The lineshape $I(\omega)$ is sinusoidal in ω with a "period" of approximately $1/T$; a longer interaction time T leads to a lineshape which oscillates "faster" in ω. The amplitude and phase of the sinusoidal lineshape are modulated by the "Rabi envelope". The amplitude modulation of this envelope determines the gross structure of the lineshape, and its shape roughly corresponds to what the lineshape would look like for just one of the oscillatory fields.

The lineshape in Eq. (3.56) is quite complicated and not particularly useful to us. We can make it much simpler if we only consider detunings near the resonance where $|\Delta| \ll \omega_R$. In this case, to zeroth-order in Δ/ω_R, $\sin\chi = 0$ and $\cos\chi = 1$, and the lineshape simplifies to

$$I(\omega) = \sin^2(\omega_R\tau)\cos(\Delta T-\phi_0) - \cos^2(\omega_R\tau), \tag{3.57}$$

where the period is exactly $1/T$. In this approximation, the effects of the Rabi envelope are absent.

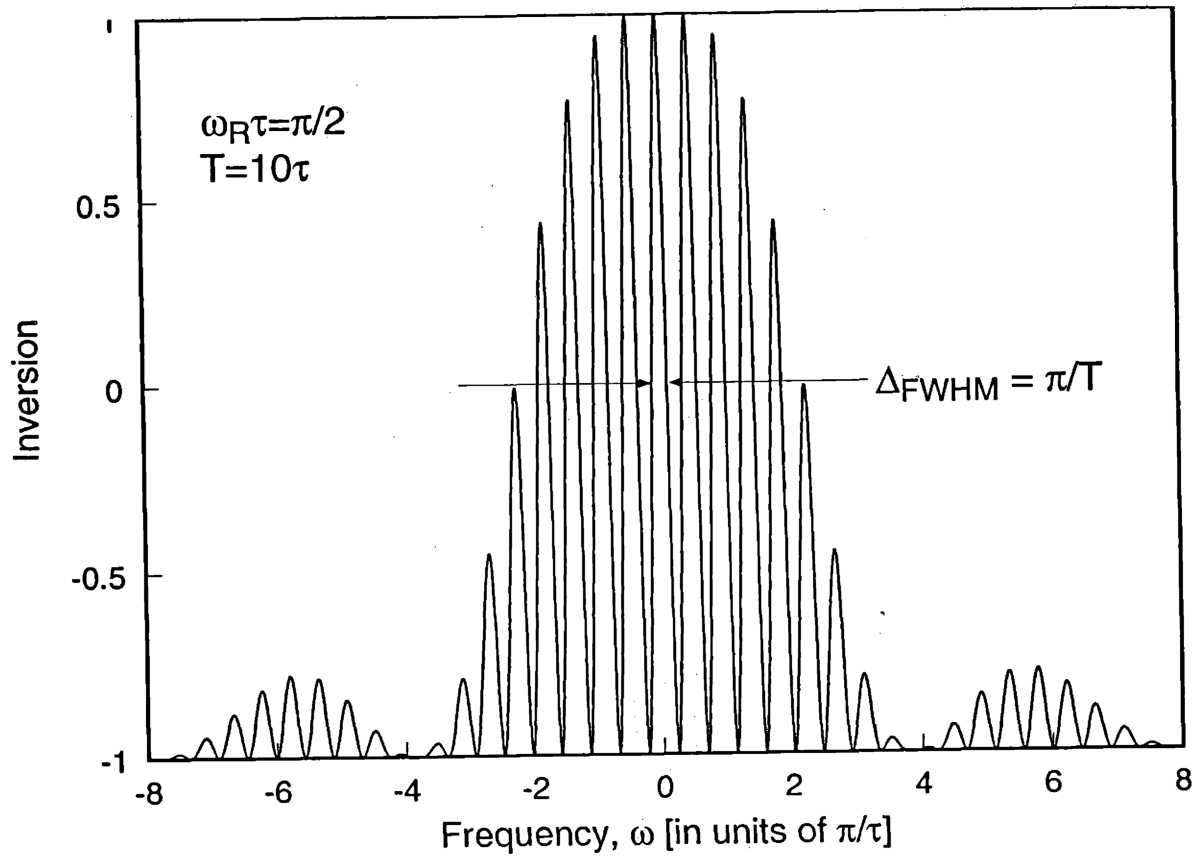

Figure 3-2: Ramsey resonance lineshape, Eq. (3.56). The interaction time τ was chosen such that $\omega_R \tau = \pi$, yielding the maximum amplitude for the lineshape.

In order to estimate the effects of the Rabi envelope on the Ramsey lineshape, we now go to first-order in Δ/ω_R. We allow the resonance frequency of the atom to vary: ω_1 during the first oscillatory field, ω_2 during the second oscillatory field, and ω_0 between the oscillatory fields. Now the condition for small detunings is:

$$|\Delta_1| \ll \omega_R, \quad |\Delta_2| \ll \omega_R, \quad |\Delta| \ll \omega_R, \tag{3.58}$$

where $\Delta_1 = \omega - \omega_1$ and $\Delta_2 = \omega - \omega_2$. In terms of the Bloch vector, we write

$$\vec{s}(t=\tau) = \mathcal{R}(\hat{\Omega}_2, \Omega_2 \tau)\ \mathcal{R}(\hat{z}, \mp(\Delta T - \phi_0))\ \mathcal{R}(\hat{\Omega}_1, \Omega_1 \tau)\ \vec{s}(t=0), \tag{3.59}$$

where $\vec{\Omega}_1$ and $\vec{\Omega}_2$ are the pseudo torques for the first and second oscillatory fields, respectively. We use the rotation matrix in Eq. (3.50) (which is good to first-order in Δ/ω_R) to evaluate the first and last rotations in Eq. (3.59). Taking $\vec{s}(t=0) = (0,0,-1)$, the inversion is, after some algebra

$$I(\omega) = \sin^2(\omega_R\tau)\cos\left[\Delta T - \phi_0 + 2\frac{\Delta_{12}}{\omega_R}\tan(\omega_R\tau/2)\right] - \cos^2(\omega_R\tau), \tag{3.60}$$

where $\Delta_{12} = (\Delta_1 + \Delta_2)/2$ is the average detuning during the oscillatory fields. The amplitude modulation due to the Rabi envelope is absent in this expression, and it is purely sinusoidal in ω. However, there is some phase modulation due to the Rabi envelope, given by the term involving the tangent function.

3.5 Effects due to the Rabi envelope

We now consider the small effect of the phase modulation due to the Rabi envelope, present in Eq. (3.60), but not in Eq. (3.57). If we set $\omega_{12} = \omega_0$, then the term in Eq. (3.60) which involves the tangent function modulates the phase in such a way that the period of the sinusoid is $1/T'$ rather than $1/T$, where $T' = T + \tan(\omega_R\tau/2)/(\omega_R/2)$. If we further consider just the interaction time for which $\omega_R\tau = \omega_R T(l/L) = \pi/2$, then $T' = T(1 + \frac{\pi}{4}\frac{l}{L})$. The phase modulation has the effect of making the period $1/T'$, slightly shorter than $1/T$. This can be seen as due to the evolution of the phase of the atom not just during the interaction time T, but also during the oscillatory field times τ.

If $\omega_{12} \neq \omega_0$, then the phase modulation due to the Rabi envelope not only modifies the period, but also, as we show below, has the effect of "pulling" (shifting) the line-shape. The frequency ω_{12} can differ from ω_0 for three main reasons: non-uniformity of the electric field, non-uniformity of the magnetic field, and the first-order Doppler effect. (The first-order Doppler effect can be viewed as a shift in the resonance frequency while the atoms interact with the oscillatory fields.) We write ω_{12} as

$$\omega_{12} = \omega_0 + \delta\omega_{Fields} + \delta\omega_{Dop}, \tag{3.61}$$

where $\delta\omega_{Dop}$ is due to the first-order Doppler effect and $\delta\omega_{Fields}$ is due to the nonuniformity of the external fields. The first-order Doppler effect depends on the velocity v, or equivalently on $1/T$, where $T = L/v$ is the interaction time. To make this T-dependence explicit, we write it as

$$\delta\omega_{Dop} = \delta\omega^0_{Dop}\frac{T_0}{T}, \tag{3.62}$$

where $\delta\omega^0_{Dop}$ is the first-order Doppler shift for an atom with (arbitrary) interaction time T_0. We calculate the value of $\delta\omega^0_{Dop}$ later in Sec. 3.8.2. In the present discussion we just need the T-dependence of $\delta\omega_{Dop}$.

In order to estimate the size of the "pulling" due to the Rabi envelope when $\omega_{12} \neq \omega_0$, we rewrite Eq. (3.60) with the above definitions of ω_{12} and $\delta\omega_{Dop}$:

$$\begin{aligned} I(\omega) = A\cos\Bigg[\quad & (\omega-\omega_0)\left(T + \frac{\tan(\omega_R\tau/2)}{\omega_R/2}\right) - \delta\omega_{Fields}\frac{\tan(\omega_R\tau/2)}{\omega_R/2} && (3.63) \\ & -\delta\omega^0_{Dop}\frac{T_0}{T}\frac{\tan(\omega_R\tau/2)}{\omega_R/2} + \phi_0\Bigg] + B, && (3.64) \end{aligned}$$

where $A = \sin^2(\omega_R\tau)$ and $B = \cos^2(\omega_R\tau)$. This expression is complicated and difficult to interpret. To simplify it, we perform a Taylor series expansion on the argument of the cosine function around $T = T_0$, and we let T_0 be the interaction time that satisfies $\omega_R T_0(l/L) = \pi/2$. (Note that before performing this expansion, we replace τ with $T(l/L)$.) We only keep terms up to first-order in the Taylor series, and we express the result in terms of new variables in order to compare it to Eq. (3.57):

$$I(\omega) = A\cos[(\omega-\omega_0')T' + \phi_0'] + B, \tag{3.65}$$

where we refer to ω_0', T', and ϕ_0' as the effective resonance frequency, effective interaction time, and the effective end-to-end phase, respectively. These new variables are given by:

$$\omega_0' \quad = \quad \omega_0 + 2\frac{l}{L}\delta\omega_{Fields} + \left(2 - \frac{4}{\pi}\right)\frac{l}{L}\delta\omega^0_{Dop}, \tag{3.66}$$

$$T' = T\left(1+2\frac{l}{L}\right) - \frac{\pi-2}{\omega_R}, \tag{3.67}$$

$$\phi_0' = (\pi-2)\frac{\delta\omega_{Fields}}{\omega_R} + (\pi-4)\frac{\delta\omega^0_{Dop}}{\omega_R} + \phi_0. \tag{3.68}$$

Now we can see the approximate effect of the pulling by examining these effective variables. The effective resonance frequency ω_0' is pulled from ω_0 by $\delta\omega_{Fields}$ and $\delta\omega^0_{Dop}$, but only by an amount which is reduced by $\approx l/L$. The end-to-end phase is also pulled by a small amount. The effective interaction time is slightly longer, but it is not affected by the pulling, i.e., it does not depend on $\delta\omega_{Fields}$ or $\delta\omega^0_{Dop}$.

3.6 Basic lineshape model and fitting procedure

Recall that our resonance data is not averaged over the entire transit time distribution—it is time-resolved resonance data. We bin the data into several time bins which we analyze individually. Later, in Sec. 3.11.2, we consider the effect of the finite width of the bins.

For the data that we take, the condition $\Delta \ll \omega_R$ always holds, and we use the approximate formula given in Eq. (3.57) as the starting point for our basic single-time-bin lineshape model. Later, we use the result in Eqs. (3.66–3.68) to show that, in our experiment, we can safely neglect the frequency pulling due to the fact that $\omega_{12} \neq \omega_0$.

It is useful to introduce two new variables for the radiation frequency and the atomic resonance frequency, which are both defined with respect to ω_C the experimentally chosen center frequency of a frequency scan. We write the radiation frequency as $\delta = \omega - \omega_C$ and the atomic resonance frequency as $\delta_0 = \omega_0 - \omega_C$. With these new variables, δ is precisely known, and the goal is to measure δ_0. Using the expression for $I(\omega)$ in Eq. (3.57), along with these variables, our single-time-bin lineshape model takes the form:

$$I(\delta) = \sin^2(\omega_R\tau)\cos[\delta T - (\delta_0 T + \phi_0)] - \cos^2(\omega_R\tau). \tag{3.69}$$

Rewriting this in terms of the parameters we actually use to fit the j-th time bin of resonance data, we have:

$$I_j(\delta) = A_j \cos(\delta T_j - \Phi_j) + B_j, \tag{3.70}$$

$$\text{where} \quad \Phi_j = \delta_0 T_j + \phi_0. \tag{3.71}$$

For each time bin j, our model has four fit parameters. The four parameters are: the amplitude A_j, the interaction time T_j, the phase Φ_j, and the baseline, B_j. The phases Φ_j and the interaction times T_j, for all the time bins j, are the important parameters because they contain information on the resonance detuning δ_0 through Eq. (3.71). Specifically, Eq. (3.71) states that Φ_j, which is the phase of the sinusoidal lineshape at the scan center for bin j, is a linear function of T_j, which is the of the interaction time for bin j, with slope δ_0 and "y-intercept" ϕ_0. In principle, for each time bin we could fix the three parameters A_j, B_j, and T_j, but instead we let them be fit parameters because they are modified by many effects which are difficult to predict, as discussed later in this section.

Our basic fit procedure, which we use to extract the resonance detuning δ_0, is as follows. The form of the experimental lineshape for each time bin is given by Eq. (3.1). We reprint this equation here, but for clarity we drop the subscripts j and the functional dependence on ω:

$$I_{exp} = \frac{C^f - C^i}{C^f + C^i}. \tag{3.72}$$

If we take the uncertainty in the counted number of atoms to be the square root of the number of atoms and then use the normal rule for error propagation, we find that the uncertainty in the measured inversion is

$$\Delta I_{exp} = \frac{2\sqrt{C^f C^i}}{(C^f + C^i)^{3/2}}. \tag{3.73}$$

Actually, the uncertainty in the number of counted atoms is greater than just the square root of the number of atoms because of fluctuations in the atomic hydrogen source, laser excitation, et cetera. These fluctuations, however, affect the number of atoms counted in both the initial and final states, causing no fluctuations in the measured inversion.

We fit the resonance data to Eqs. (3.70-3.71) in a two-part procedure: First, we perform a least-squares fit of the experimental lineshape for each time bin to Eq. 3.70, yielding both the phase Φ_j and the interaction time T_j for each time bin. (This fit also yields the amplitudes A_j and the baselines B_j, but these are not important in the analysis to follow.) Then, we perform a second least-squares fit of our measurements for Φ_j to Eq. 3.71; this equation shows that Φ_j is a linear function of T_j, with slope δ_0 and "y-intercept" ϕ_0. In this fit, we use two fit parameters, δ_0 and ϕ_0, and we fix the values of T_j because the uncertainties in the results for T_j from the first fit are negligible. (Unfortunately, we have no direct way to measure the end-to-end phase ϕ_0 so we must leave it as a fit parameter.) The resonance frequency ω_0 is then found from the result for the fit parameter δ_0 using: $\omega_0 = \delta_0 + \omega_C$, where ω_C is the (known) scan center-frequency.

3.7 Effects due to the nature of the oscillatory fields

3.7.1 Square pulses versus gaussian pulses

The ideal Ramsey resonance lineshape assumes that the amplitude of the oscillatory field as a function of time is described by two short square-pulses of time τ separated by a time $T \gg \tau$. In our experiment, the atoms traverse the waists of two separate gaussian beam modes, thus the atoms see two *gaussian* pulses—not square pulses. This change slightly affects the shape of the Rabi envelope. It turns out that there is no analytical solution for gaussian pulses, except for when $\omega = \omega_0$. For small detunings, however, the approximate form for the lineshape given in Eq. 3.57, on which our basic lineshape model is based, is valid for both square and gaussian pulses. In this equation, the amplitude and baseline depend on the *area* of each pulse (given by $\omega_R\tau$ for a square pulse), and there is no dependence on the *shape* of the pulses.

Because the amplitude and baseline are arbitrary fit parameters in the basic lineshape model, we do not need to change it.

3.7.2 Variations in the oscillatory field amplitude and phase

Another effect due to the nature of the oscillatory fields is that atoms with different trajectories see different oscillatory field amplitudes and phases. The oscillatory fields are actually gaussian beam modes of two separate near-confocal cavities. The absolute value of the amplitude varies like $|\sin(kz)|$, where k is the wave-vector and z is the distance along the axis of the gaussian beam mode, while the phase changes by π between neighboring anti-nodes. Hence, the amplitude seen by a particular atom depends on the z-coordinate at which that atom intersects the gaussian beam mode, and the phase differs by π depending on which anti-node the atom intersects. (Changes in phase if the atom has any motion in the z-direction and the field has a running-wave component result in a first-order Doppler effect, which is discussed later.)

We use slits to collimate the atomic beam such that it has a width of about 1/2 of a wavelength, equal to about 1/2 mm. We align the atomic beam so that the atoms tend to intersect just one anti-node of each of the two standing-waves. Almost all of the atoms "see" the same oscillatory field phase, but they "see" a range of oscillatory field amplitudes. The resulting lineshape is an average over sinusoidal lineshapes with the same phase Φ_j and period $1/T_j$, but with varying amplitude A_j and baseline B_j because these two parameters depend on the Rabi frequency, which in turn depends on the oscillatory field amplitude. Only the amplitude A_j and baseline B_j of the resultant sinusoidal lineshape are modified, and these effects are absorbed into the arbitrary fit parameters, A_j and B_j, of the basic model, given in Eqs. (3.70-3.71)

3.8 Pulling when $\omega_{12} \neq \omega_0$

If the average resonance frequency during the oscillatory fields, $\omega_{12} = (\omega_1 + \omega_2)/2$, is different from the average resonance frequency between the oscillatory fields, ω_0, then the Rabi envelope is shifted and it "pulls" the lineshape, i.e., it biases the fitted resonance frequency away from ω_0. The approximate effect of the pulling can be seen in Eqs. (3.66–3.68) We first consider the pulling due to non-uniformities in the electric and magnetic fields, and then due to the Doppler effect.

3.8.1 Pulling due to shifts in Stark and Zeeman effects

Circular state transitions exhibit a second-order Stark effect, and any difference between the stray electric fields in the two regions of the oscillatory fields and the stray electric fields in between the oscillatory fields contribute to $\delta\omega_{Fields}$. However, the Stark effect due to stray fields in all of the interaction region is estimated to be negligible, as described in Sec. 5.2, so that any pulling due to differences in the stray electric fields is also negligible.

Circular state transitions exhibit a first-order Zeeman effect, and we measure both the $\Delta m_\ell = \pm 1$ circular state transitions to eliminate it. If the lineshape is pulled one way for the $\Delta m_\ell = +1$ transition, then it will be pulled the other way for the $\Delta m_\ell = -1$ transition. Any pulling due to non-uniformity of the magnetic field is eliminated.

3.8.2 Pulling due to the first-order Doppler effect

The first-order Doppler effect occurs because of phase changes that an atoms "sees" as it travels across an oscillatory field. We interpret this effect as a shift in the resonance frequency of the atom. Two aspects of the geometry of our experiment combine to reduce the first-order Doppler effect $\delta\omega_{Dop}$ to a negligible level: 1) The atomic beam is nearly perpendicular to the direction in which the oscillatory fields travel, and 2) the oscillatory fields are nearly perfect standing-waves, produced by cavities.

We write the first-order Doppler effect for an atom with interaction time T_0 as

$$\delta\omega^0_{Dop} = \alpha\beta\frac{L}{cT_0}\omega_0, \tag{3.74}$$

where α is the angular deviation from perpendicularity and β characterizes the (small) size of the travelling wave component. We align the cavities such that $\alpha < 0.005$ rad. The factor β is defined by $\beta = (A_{inc} - A_{ref})/(A_{inc} + A_{ref})$, where A_{inc} and A_{ref} are the amplitudes of the two travelling waves in the cavity. The relative size of these amplitudes is determined by the reflectivity of the cavity end mirror: $A_{ref} = |r_e| A_{inc}$, where $|r_e| = 1 - \epsilon$ and $\epsilon \ll 1$, so that we can write $\beta \approx \epsilon/2$. From measurements of the cavity finesse, we find that $\epsilon \approx 5 \times 10^{-3}$. For the mean velocity of atoms in our experiment, the factor of $L/(cT_0)$ is $\approx 3 \times 10^{-6}$. Using these values and a resonance frequency of $\omega_0 \approx (2\pi)3 \times 10^{11}$, we find that $\delta\omega_{Dop}^0 < (2\pi)11$ Hz.

From Eq. (3.66), we see that the frequency pulling due to the Doppler effect is reduced by a factor of $\approx 0.7(l/L)$. This result is for a square pulse of radiation of length l, and the atoms in our experiment "see" a gaussian pulse with waist $\mathrm{w}_0 = 3.6$ mm. We model this gaussian pulse as a square pulse of length $l = 2.4\mathrm{w}_0$, so that $l = 8.6$ mm. The length between the oscillatory fields is $L = 508$ mm. The pulling due to the first-order Doppler effect is then $0.7(l/L)\delta\omega_{Dop}^0 < (2\pi)0.13$ Hz, which is negligible.

3.8.3 Pulling due to Bloch-Siegert and Millman effects

The Bloch-Siegert effect [Ram56] arises out of the rotating-wave approximation, where the counter-rotating wave is ignored. The counter-rotating wave perturbs the resonance frequency during the oscillatory fields, and contributes to $\delta\omega$ the following amount[Ram56]:

$$\delta\omega_{B-S} = \frac{\omega_R^2}{4\omega_0}. \tag{3.75}$$

Typically in our experiment, $\omega_R \tau = \pi/2$ when $\tau \approx 10\mu$s, so that $\omega_{B-S} \approx (2\pi)5 \times 10^{-4}$ Hz, which is a negligible contribution to $\delta\omega$.

The Millman effect [Ram56] contributes to $\delta\omega$ and can pull the resonance frequency. It arises if the direction of the oscillatory field rotates along the length of the oscillatory field region. In our experiment, the atoms cross the gaussian beam mode at an anti-node near its waist where the wave front is nearly planar, so that this effect should be small. Furthermore, we measure both the $\Delta m_\ell = \pm 1$ circular state transitions which are oppositely sensitive to rotations in the direction of the oscillatory field. By averaging these two transitions, we eliminate any residual pulling due to the Millman effect.

3.9 Second-order Doppler effect

The second-order Doppler effect, sometimes referred to as time-dilation, is easier to calculate than the first-order Doppler effect, since it does not depend on geometry. It is given by $\omega_{Dop}^{(2)} = -(1/2)(v/c)^2\omega_0$. Using $(v/c) \approx 3 \times 10^{-6}$ and $\omega_0/2\pi \approx 3 \times 10^{11}$, the approximate size is $\omega_{Dop}^{(2)}/2\pi \approx 1.4$ Hz. The second-order Doppler shift is easily included in our basic model lineshape by redefining Φ_j, given in (Eq. 3.71), to include an extra term: $\omega_{Dop}^{(2)}T_j = -(1/2)(L^2/(T_j c^2)\omega_0$.

3.10 Circular Rydberg atoms versus two-level atoms

We now discuss the modifications to our basic lineshape model which are necessary because there are more than just two levels in our atomic system.

3.10.1 Fine structure doublet

The most important modification to our basic lineshape model arises from the fact that we do not completely resolve the fine structure. As discussed in Sec. 2, we drive *two* two-level systems—one system for each spin state. For the $n = 29 \rightarrow 30$ transition, the fine structure splitting in the transition frequency (i.e., the splitting in the transition frequency between atoms with spin up and spin down) is $\Delta\nu_{fs} \approx 1.4$ kHz, and for the $n = 27 \rightarrow 28$, it is $\Delta\nu_{fs} \approx 2.1$ kHz. These splittings are comparable to the period of the sinusoidal lineshape, so when the lineshapes from the two spin components add, they interfere either constructively and destructively, depending on the period of the lineshape $1/T_j$ and the splitting $\Delta\nu_{fs}$. The interference is entirely destructive when the interaction time is given by: $T = m/(2\Delta\nu_{fs})$, where m is a positive, odd integer. As discussed in Sec. 7.3, we believe the two spin components have essentially equal weights. However, in the following discussion we allow the two spin components to have arbitrary weights.

When we include both spin components, the resultant lineshape for a given time bin is the sum of two component lineshapes, each of the form given in Eqs. (3.70-3.71) The two component lineshapes share the same period, amplitude, and baseline, but they have different phases. The resonance detunings for the two component lineshapes are $\delta_0 + \delta_{fs}/2$ and $\delta_0 - \delta_{fs}/2$, where $\delta_{fs} = 2\pi\Delta\nu_{fs}$ is the fine structure splitting in the transition frequency. The phases of the two component lineshapes are $\Phi_j = (\delta_0 + \delta_{fs}/2)T_j + \phi_0$ and $\Phi_j = (\delta_0 - \delta_{fs}/2)T_j + \phi_0$. Allowing for polarization of the electron spin, the two component lineshapes have different weights, P_+ and P_-, where P_+ is the fraction of states contributing to the high frequency fine structure component, and P_- is the fraction for the lower frequency component. Since the two component lineshapes have the same period, we can write their weighted sum as *one* cosine function in same form as Eq. 3.70, but with the cosine function being multiplied by a factor of C_{fs} and an additional term ϕ_{fs} added to the argument of the cosine function, where C_{fs} and ϕ_{fs} are given by

$$C_{fs} = \left(\frac{1}{2}\left[1 + \psi^2 + (1 - \psi^2)\cos(\delta_{fs}T_j)\right]\right)^{1/2} \tag{3.76}$$

$$\phi_{fs} = \arctan\left[\psi \tan\left(\frac{\delta_{fs}T_j}{2}\right)\right]. \tag{3.77}$$

Here, ψ is the polarization, defined as $\psi = P_+ - P_-$. Thus we can continue to use our basic model in Eq. 3.70, so long as we allow the arbitrary amplitude parameter A_j to absorb the factor of C_{fs}, and redefine the phase of the lineshape Φ_j, given in Eq. 3.71, to include the additional term: $\Phi_j = \delta_0 T_j + \phi_0 + \phi_{fs}$.

If we consider the case of completely polarized electrons ($\psi = \pm 1$), then $C_{fs} = 1$ and $\phi_{fs} = \pm\delta_{fs}T_j/2$, and the lineshape reverts to a single component lineshape with a resonance detuning (the detuning of the resonance from the scan center) of $\delta_0 \pm \delta_{fs}/2$. If we consider the case of completely unpolarized electrons, ($\psi = 0$), then $C_{fs} = \cos(\delta_{fs}T_j)/2$ and $\phi_{fs} = 0$. In this case, the interference of the two components modulates the amplitude sinusoidally in T_j by the factor C_{fs}, but the phase of the lineshape is left unchanged. In this case, the amplitude goes to zero at an interaction time T_C, given by

$$T_C = \frac{2\pi m}{2\delta_{fs}}, \tag{3.78}$$

where m is an odd positive integer. If there is some small amount of polarization ($\psi \ll 1$) then the interference is not total: C_{fs} never goes completely to zero, and the phase ϕ_{fs} deviates from zero, especially near the minima of C_{fs}.

It should be noted that there is also hyperfine structure, but this structure is on the order of 1 Hz, well below the resolution of our apparatus, and it is symmetric, so that it causes no net shift of the lineshape.

3.10.2 Spontaneous decay and thermal radiation

We now examine another way in which our system differs from a perfect two-level system. In addition to the transitions that we coherently drive between the lower and upper circular states in our system (which have quantum numbers n_i and $n_f = n_i+1$), there are incoherent transitions which occur due to spontaneous decay and thermal radiation. These incoherent processes drive transitions between the lower and upper circular states. They also drive transitions out of the two-level system to nearby states. In this section, we discuss the rates for these incoherent transitions and consider their effect on the lineshape. Peter Chang's thesis shows that the frequency shifts due to the thermal radiation are negligible (<0.2 Hz for any temperature less than 300 K).

A circular state with quantum number n spontaneously decays to the next lower circular state with quantum number $n-1$. This is the only spontaneous decay channel allowed. The spontaneous decay rate is given by the Einstein A coefficient. For $n \gg 1$, $A \approx \frac{2}{3}\alpha^3 n^{-5}(4\pi c R_\infty)$ for the $n \to n-1$ transition (and the $n+1 \to n$ transition). For the $n = 30 \to 29$ decay, $A \approx 5 \times 10^2\mathrm{s}^{-1}$, corresponding to a natural lifetime of $\tau_0 \approx 2$ ms. In our experiment we detect atoms over a wide range of the velocity distribution, and the interaction time T ranges from about 0.1 to 0.7 ms.

Thermal radiation mainly drives transitions to the next lower $(n-1)$ and next higher $(n+1)$ circular states. The rate for transitions driven by blackbody radiation at temperature T_r is $A\bar{n}$, where $\bar{n} = (e^{h\nu/kT_r} - 1)^{-1}$ is the mean photon occupation number for the transition frequency ν. For circular Rydberg state transitions, $\nu \approx n^{-3}(2cR_\infty)$.

Including both spontaneous decay and thermal radiation, the total rate for the $n \rightarrow n-1$ transition is $A(1+\bar{n})$, and the total rate for the $n \rightarrow n+1$ transition is $A\bar{n}$. Hence, the total decay rate out of a circular state is $A(1+2\bar{n})$. At room temperature, $\bar{n} \approx 25$, leading to a total decay rate about 50 times greater than spontaneous decay alone. To reduce the effects of thermal radiation, we cryogenically cool the environment to 4 K, and we find that $\bar{n} \approx 0.3$ for photons with the $n = 29 \rightarrow 30$ transition frequency, which corresponds to a blackbody temperature of ≈ 9 K. Further cooling would not increase the lifetime much, as the lifetime is dominated by spontaneous decay.

The thermally-driven transitions between the lower and upper circular states have the effect of reducing the amplitude A of the sinusoidal lineshape. The spontaneous decay from the upper circular state to the lower circular state both reduces the amplitude A and lowers the baseline B of the sinusoidal fringe. Incoherent transitions out of the two-level system to nearby states with $n \neq n_i$ and $n \neq n_f$ simply reduces our counting rate R because these states are not detected. Incoherent transitions out of the two-level system to near-circular states with $n = n_i$ or $n = n_f$ have the effect of reducing the amplitude and modifying the baseline of the sinusoidal lineshape because our detectors do not discriminate a near-circular state with principal quantum number n from a circular state with principal quantum number n.

For a given atom in our experiment, the processes described above can happen multiple times and in different combinations. It is difficult to model the exact effect of these processes, and we do not attempt to do this. Instead, we allow the parameters for the amplitude and the baseline for each time bin, A_j and B_j, to be arbitrary fit parameters, and the net effect of these incoherent processes is absorbed into A_j and B_j.

We are limited by the natural lifetime from using much longer interaction times.

Longer interactions times not only reduce the number of atoms detected, because more atoms spontaneously decay out of the two-level system, but also reduce the amplitude of the lineshape for the atoms that are detected, because spontaneous decay from the upper level to the lower level reduces the phase coherence between the two levels.

3.11 Effects due to the detection apparatus

3.11.1 Imbalance of the detector efficiencies

The atoms are detected by two channeltrons; one channeltron detects the atoms in the initial (lower) state, and the other detects those in the final (upper) state. The resolution between the initial and final states is practically perfect. However, the two detectors have different efficiencies, e_i, and e_f. After a little algebra, the detected inversion I_d can be written as

$$I_d = \frac{(1+I) - a(1-I)}{(1+I) + a(1-I)} \tag{3.79}$$

where a is the relative efficiency, $a = e_i/e_f$. If $a \neq 1$ there is a baseline shift and the shape of the fringe is slightly distorted. Typically, $a = 0.7 \rightarrow 0.8$. This effect, does not bias Φ_j, the phase of the lineshape. Nevertheless, we include this effect in our data analysis.

3.11.2 Finite width of the time bins

The sinusoidal lineshape model given in Eqs. (3.70-3.71) is actually for a discrete interaction time T_j which depends on the time bin j. The relationship between the transit time $\mathcal{T}_j$ and the interaction time T_j depends on the ratio of the length L between the two oscillatory fields and the length $\mathcal{L}$ of the atomic beam: $T_j = \mathcal{T}_j(L/\mathcal{L})$.

We separate our Ramsey resonance data into about 20 time bins of width $\mathcal{T}_{bin} = 50$ μs so that the experimental lineshape for each time bin j is an average over a narrow range of transit times around $\mathcal{T}_j$. To model this effect, we average Eq. (3.70) over a range $T_{bin} = \mathcal{T}_{bin}(L/\mathcal{L})$ around T_j. We assume that the center of the frequency scan is close to the resonance frequency (so that $\delta_0 \cdot T_{bin} \ll 1$), and we get:

$$I_j = \frac{\sin\left(\frac{T_{bin}}{2}\delta\right)}{\left(\frac{T_{bin}}{2}\delta\right)} A_j \cos\left(\delta T_j - \Phi_j\right) + B_j. \tag{3.80}$$

The new factor is of the form $\sin x/x$ and tends to wash out the lineshape for large detunings from the resonance, but it does so in a symmetric manner. For our data, at the largest detunings, the $\sin x/x$ factor is never less than about 0.9. This factor does not bias the phase or period of the lineshape—the parameters important to our fit results—but we include it in our fit function anyway because it increases the goodness of the fit.

It should be noted that this equation doesn't include the varying weight of lineshapes with different interaction times. The amplitude of the lineshape varies slightly over the bin width, and in addition the number of atoms contributing varies due to the velocity distribution. These two effects tend to bias the the period of the lineshape $1/T_j$ away from the period corresponding to the center of the time bin. Rather than try to model this, we simply allow T_j to be a fit parameter.

3.12 Summary of our lineshape model

In this section we summarize our lineshape and fitting procedure. Not including the differing efficiency of the two detectors, the single-time-bin lineshape is given by:

$$I_j = \frac{\sin(\frac{T_{bin}}{2}\delta)}{(\frac{T_{bin}}{2}\delta)} A_j \cos\left(\delta T_j - \Phi_j\right) + B_j. \tag{3.81}$$

$$\text{where} \quad \Phi_j = \delta_0 T_j + \phi_0 - \frac{L^2\omega_0}{2c^2 T_j} + \arctan\left[\psi \tan\left(\frac{\delta_{fs} T_j}{2}\right)\right]. \tag{3.82}$$

Including the relative detector efficiency a, the lineshape is:

$$I_j^d = \frac{(1+I_j) - a(1-I_j)}{(1+I_j) + a(1-I_j)} \tag{3.83}$$

To find the resonance detuning δ_0, we fit all the time bins in a data set to Eq. 3.83 with a as a global fit parameter, as well as the four fit parameters for each bin: A_j, B_j, Φ_j, and T_j. We then fit our results for Φ_j to Eq. 3.82 using our results for T_j and three fit parameters: ψ, δ_0, and ϕ_0. The frequency of the transition ω_0 is given by δ_0 through its definition: $\omega_0 = \omega_C + \delta_0$ where ω_C is the experimentally chosen center of the frequency scan.

Chapter 4

Experimental Apparatus

4.1 Atomic hydrogen beam

4.1.1 Hydrogen source

We produce atomic hydrogen by dissociating molecular hydrogen in an RF discharge contained in a water cooled Pyrex tube. The atoms then flow through a teflon tube and into the thermalizer, which is a channel (≈ 2.3 mm in diameter and ≈ 9.5 mm in length) in an aluminum block. We cool the thermalizer to 80 K. Each atom tends to make several collisions with the walls of the channel, which thermalizes the atoms at 80 Kelvin. The flux Q out of the thermalizer follows a cosine distribution[Ram56]: $dQ(\theta)/d\Omega = (Q/\pi)\cos\theta$. By measuring relevant gas pressures and volumes we estimate the forward flux out of the thermalizer to be (assuming 100% dissociation)

$$\frac{dQ(0)}{d\Omega} = \frac{Q}{\pi} = 8 \times 10^{17}\ \mathrm{sr}^{-1}\mathrm{s}^{-1}. \qquad (4.1)$$

The mean speed of the atomic beam at 80 K is $\bar{v} = 1.41$ mm/μs.

4.1.2 Vacuum design

Our vacuum apparatus has three separate chambers, each with its own pump. The source chamber contains the hydrogen source, the main chamber contains the interaction region, and these two chambers are connected by a differentially pumped chamber. We keep the pressure of the background gas low so that it does not attenuate the atomic beam or significantly perturb the transition frequencies.

A cryopump (pumping speed of 2000 l/s) maintains the source chamber pressure at about 10^{-5} torr when the beam is on. The differentially pumped chamber is pumped by a small turbo pump (pumping speed of 50 l/s). The pressure in this differentially pumped region is about 2×10^{-6} torr. The main vacuum chamber contains the interaction region, which is a long copper enclosure that we cool to 4 K, and it is surrounded by a cryogenic shield which we cool to 80 K. The main chamber is pumped on by a larger turbo pump (pumping speed of 170 l/s). The pressure outside the cryogenic shield is about 1×10^{-8} torr when the beam is on and 1×10^{-9} torr when the beam is off. Inside the interaction region, however, the main pumping mechanism is the walls of the interaction region which cryogenically pump the hydrogen gas load, and the pressure of the background gas should be much lower.

4.1.3 Beam collimation

We collimate the atomic beam, mainly so that it "sees" only a limited distribution of the oscillatory fields' amplitude and phase. In this section, we first describe the geometry of the oscillatory fields, and then the horizontal and vertical collimation of the atomic beam.

Each oscillatory field is the fundamental gaussian beam mode of a near-confocal cavity. The axis of the atomic beam is horizontal. The axis of each cavity is horizontal and perpendicular to the atomic beam. The atomic beam intersects the two gaussian beam modes near their waists. Along the axis of each gaussian beam mode, the field amplitude and phase vary on the scale of 1/2 a wavelength, or about 0.5 mm. The waist of each gaussian beam mode is about 3.6 mm, so the field is much more uniform along directions perpendicular to the gaussian beam mode axis.

The horizontal collimation is illustrated in Fig. 4-1. 4-1. The atomic beam exits the thermalizer hole (diam. = 2.3 mm) and travels for 37 cm before we collimate it in the horizontal direction with an adjustable slit (typically 0.7 mm wide). As described

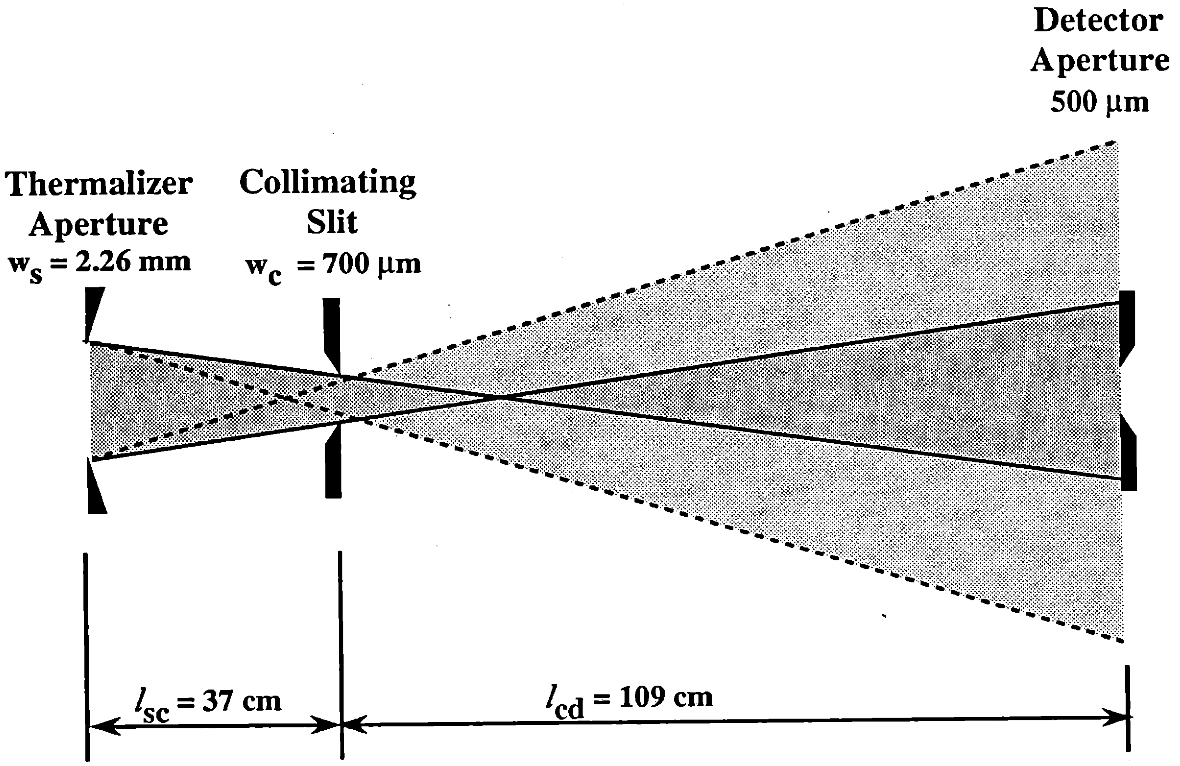

Figure 4-1: Horizontal Collimation. The four lines drawn are the limiting trajectories between the thermalizer aperture and the collimating slit. This diagram is roughly to scale, but the vertical scale has been expanded by about a factor of one hundred relative to the horizontal.

in[Ram56], this produces a trapezoidal intensity distribution. At position x_c, which is the position along x with respect to the collimator, the upper and lower widths of the trapezoid are

$$p_H = \left| \mathrm{w}_c + (\mathrm{w}_c - \mathrm{w}_s)\frac{x_c}{l_{sc}} \right| \tag{4.2}$$

$$d_H = \left| \mathrm{w}_c + (\mathrm{w}_c + \mathrm{w}_s)\frac{x_c}{l_{sc}} \right|, \tag{4.3}$$

respectively, where w_s and w_c are the source and collimator widths, and l_{sc} is the source-collimator distance. The FWHM of the trapezoid is $(p_H + d_H)/2$. The detector, located 109 cm from the adjustable slit, has a fixed aperture (0.5 mm wide) which accepts only a small portion of the horizontal distribution. The combination of the adjustable slit and the detector aperture restrict the trajectories of the detected atoms

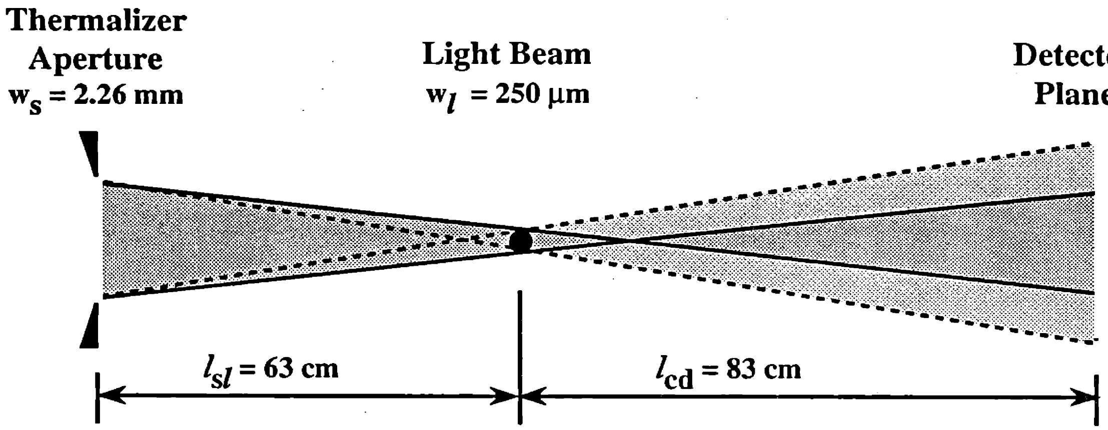

Figure 4-2: Vertical Collimation. The four lines drawn are the limiting trajectories between the thermalizer aperture and the outer dimensions of the light beam. This diagram is roughly to scale, but the vertical scale has been expanded by about a factor of one hundred relative to the horizontal.

so that they tend to "see" just one anti-node at each gaussian beam mode. At the detector, we calculate the FWHM of the trapezoidal distribution to be 6.7 mm, so that the detector only accepts $0.5/6.7 \approx 8\%$ of the horizontal atomic beam distribution.

The vertical collimation is illustrated in Fig. 4-2. The adjustable slit and the detector aperture do not limit the distribution of the atomic beam in the vertical direction. However, the optical excitation light that we use to produce Rydberg atoms effectively collimates the excited portion of the atomic beam in the vertical direction. The optical excitation light intersects the atomic beam from the side and at a distance of 63 cm from the thermalizer. The diameter of the optical excitation light beam is effectively $w_l \approx 0.25$ mm. The combination of the thermalizer and the optical excitation light restrict the vertical distribution of the excited portion of the atomic beam. The vertical distribution has a trapezoidal shape and has widths p_V and d_V similar to Eqs. (4.2–4.3). At position x_l, which is the position with respect to the laser, we have

$$\begin{aligned} p &= \left| \mathrm{w}_l + (\mathrm{w}_l - \mathrm{w}_s)\frac{x_l}{l_{sl}} \right| && (4.4) \\ d &= \left| \mathrm{w}_l + (\mathrm{w}_l + \mathrm{w}_s)\frac{x_l}{l_{sl}} \right|, && (4.5) \end{aligned}$$

where w_s and w_l are the source and light widths and l_{sl} is the source-light distance. The FWHM of the vertical distribution is ≈ 0.5 mm at the first oscillatory field, ≈ 2.4 mm at the second oscillatory field, and ≈ 3.1 mm at the detector. The aperture of the detector does not restrict the vertical distribution of the atomic beam; the entire vertical distribution is detected. The vertical distribution does not contribute much to the distribution in field amplitudes "seen" by the excited portion of the atomic beam because the waist of the gaussian beam modes is ≈ 3.6 mm. At the second oscillatory field, the upper and lower limits of the vertical distribution "see" a field amplitude reduced by about 70%.

4.1.4 Number of atoms

In this section, we make an order of magnitude estimate of both the number of atoms in a pulse of the atomic beam and the number of atoms detected per pulse.

We use pulsed light to excite the atoms from the ground state to the Rydberg state. The number of atoms excited in a single pulse is given by

$$N = \rho_E V_E \eta_E, \tag{4.6}$$

where ρ_E is the density of ground state atoms at the point of optical excitation, V_E is the volume of the intersection of the light with the atomic beam, and η_E is the excitation efficiency. The number of detected atoms per pulse is given by

$$N_D = \rho_E V_E \eta_E \eta_D, \tag{4.7}$$

where η_D is the detection efficiency. As discussed below, we fold several different factors into the detection efficiency, which we estimate to be $\eta_D = 0.025$.

The density of the atomic beam at a distance r from the thermalizer is given by

$$\rho(r) = \frac{1}{r^2 \bar{v}} \frac{dQ(0)}{d\Omega}, \tag{4.8}$$

where, as discussed in Sec. 4.1.1, $\bar{v} = 1.41$ mm/μs is the mean speed and $dQ(0)/d\Omega =$

8×10^{17} sr^{-1} s^{-1} is the forward flux. The actual density is less than this because of the imperfect dissociation fraction of roughly 75%. Also, the entrance to the interaction region is covered by a fine mesh with a 60% open area. Including these factors, the density at the excitation point is $\rho_E = 0.45\rho(r = 63\text{ cm}) = 6 \times 10^8\text{ cm}^{-3}$.

The excitation volume V_E is the overlap of the atomic beam and the excitation light. The horizontal width of the atomic beam at the point of excitation is restricted to approximately 0.7 mm by the adjustable slit, and the diameter of the excitation light is about 0.25 mm. The volume V_E is a column of atoms which is 0.25 mm in diameter and 0.7 mm long, and $V_E = 3 \times 10^{-5}\text{ cm}^3$. Combining these results, we estimate the number of atoms per pulse to be on the order of $N = 5000$.

We include several factors in the detection efficiency η_D: As discussed in a previous section, the width of the detector aperture is such that it only accepts 8% of the excited atoms. The detector aperture is covered with a 60% transmission mesh, further reducing η_D. Also, we include the effects of spontaneous decay and thermal transfer, which put roughly a quarter of the Rydberg atoms into undetected states. Assuming that the channeltron detectors themselves are 70% efficient, the detection efficiency is only $\eta_D = 0.025$.

Combining these results, we estimate the number of detected atoms per pulse to be $N_D = 130$. Experimentally, when all the subsystems are working well, we observe $N_D \approx 300$, which is in reasonable agreement with this estimate.

We run the experiment at $f = 61.00$ Hz. The relationship between the counting rate R and the average number of atoms per pulse N is

$$R = fN\eta_D \qquad \text{or} \qquad N = \frac{R}{f\eta_D}. \tag{4.9}$$

4.2 Production region

In the production region, we make circular Rydberg atoms from ground state atoms. We cannot optically excite a circular Rydberg state directly because it has $n - 1$ units of angular momentum, and one photon can supply at most one unit of angular momentum. Instead, we optically excite an $m_\ell = 0$ Stark sub-state of an n manifold, and then transfer the population to the circular state using a rotating RF field and a slowly varying DC field.

4.2.1 Optical excitation to Rydberg level

The atomic beam enters the production region in the ground state, $1S_{1/2}$. A 10 ns pulse of L_α radiation nearly saturates the $1S_{1/2} \rightarrow 2P_{3/2}$ transition. Simultaneously, a 10 ns pulse of radiation at 366 nm fully saturates the transition from the $2P_{3/2}$ state to a Rydberg state with $n = 27$ or 29. If both transitions were fully saturated, the population in the three states involved would be equalized, and the efficiency of the optical excitation would be 1/3. We do not fully saturate the $1S_{1/2} \rightarrow 2P_{3/2}$ transition, and we estimate that $\eta_E = 0.25$.

We excite the lowest energy Stark state of the $n = 27$ or 29 manifold, which has parabolic quantum numbers $m_\ell = 0$ and $k = -(n-1)$. The linewidth of the light for the $2P_{3/2}$ to n transition is about 1 GHz. In order to resolve the lowest energy Stark state of the n-manifold, we perform the optical excitation in an electric field of about 100 V/cm, which separates the Stark energy levels by about 6 GHz but does not cause level-crossing between states with different n.

The two optical excitation pulses are counter-propagating light beams which are perpendicular to the atomic beam and lie in the horizontal plane of the atomic beam. The diameter of the L_α light beam is ≈ 0.25 mm, and the other beam is larger in diameter, ≈ 1.0 mm, for ease of overlap.

The excitation light is linearly polarized in the vertical direction. This is important because elliptically polarized excitation light can polarize the electron spins, causing an imbalance in the fine structure of the Ramsey resonance data.

4.2.2 Laser system

The two radiation pulses are produced using two UV dye lasers which we built and are described in the thesis of Robert Lutwak[Lut97]. These are high power dye lasers, utilizing both a grating and an etalon for frequency selectivity. Both dye lasers operate at around 365 nm, use DMQ dye dissolved in P-Dioxane, and have linewidths of about 1 GHz.

One UV dye laser produces about 10mJ/pulse, and its frequency is subsequently tripled by four-wave mixing in a Kr/Ar gas mixture, resulting in the L_α radiation needed for the $1S$ to $2P$ excitation. The other produces about 1mJ/pulse for the $2P$ to Rydberg transition. After the light exits the dye lasers, we ensure its linear polarization by using Glan-laser polarizing prisms and by paying attention to the birefringence of the optics.

Both dye lasers are pumped by the same XeCl excimer gas laser, which operates at 308 nm and provides about 300 mJ/pulse. We set the repetition rate of the excimer laser to be 61.00 Hz. We use 61.00 Hz and not, say, 60 Hz, because, as discussed in Sec. 7.4, this limits the sensitivity of the spectroscopy to the 60 Hz noise on the millimeter-waves.

4.2.3 Circularization

About 2 μs (or about 2 mm) after the optical excitation, we begin the circularization process which lasts for about 2 μs. We transfer the population from the $m_\ell = 0$, $k = -(n-1)$ Rydberg state to the $|m_\ell| = n-1$, $k = 0$ circular Rydberg state. The circularization process and apparatus are described in detail in a previous paper [LHC+97].

Basically, we apply a rotating RF field and a slowly changing DC field (≈ 30 V/cm), and the atoms absorb $n-1$ circularly polarized RF photons, leaving the atoms in the circular state with $m_\ell = \pm(n-1)$, where the ($\pm$) sign depends on the sense of the RF field rotation. It is important that we can produce either the $m_\ell = +(n-1)$ or the $m_\ell = +(n-1)$ circular state, because we use both in order to eliminate the first-order Zeeman effect.

4.2.4 Near-circular state production

In addition to populating the circular state with n, $k = 0$, and $m_\ell = \pm(n-1)$, we can also populate the "near-circular" states with n, $k = \pm1$, and $m_\ell = \pm(n-2)$. We populate near-circular states in order to drive near-circular state transitions that we use to calibrate the electric field, as discussed in Sec. 5.2.

To populate a near-circular state with quantum number n, we laser excite the two states with quantum numbers $(n, k = (n-2), m_\ell = \pm1)$ rather than the one state with $(n, k = (n-1), m_\ell = 0)$. Then, the circularization process leaves the atoms in the near-circular states. For some reason, we produce more $k = +1$ near-circular states than $k = -1$ near-circular states, so we perform spectroscopy on the $k = +1$ states.

4.3 Separated fields region

After the atoms are circularized, they go into the separated fields region, where they pass through the separated oscillatory fields which we use to perform Ramsey resonance spectroscopy. Throughout this region, we apply uniform electric and magnetic fields. These applied fields maintain the orientation of the electron's orbital and spin motion, respectively, as discussed in Secs. 2.2 and 2.4.4.

4.3.1 Static fields

In the separated fields region, we apply a uniform, vertical electric field by biasing the top plate with $+V$ Volts and the bottom plate with $-V$ Volts, where V is on the order of 0.25 V. The top and bottom plates are separated by ≈ 2.4 cm, and the side walls are separated by ≈ 7.6 cm and are grounded. In order to reduce stray electric fields, we coat the interior surfaces of the interaction region with Aerodag, which is micron-sized graphite that is in the form of an aerosol.

We shield the entire interaction region from the ambient magnetic field using two long cylindrical magnetic shields with endcaps. The residual fields are on the order of

1 mG. Inside the shields we produce a magnetic field over the length of the interaction region with four wires which run the length of the shields. The connections between these wires and to the power supply leads are located outside the endcaps. The geometry of the wires was chosen for optimal uniformity over the region of the atomic beam. We use a current of ≈ 1 A through the wires, which produces a magnetic field of about 150 mG.

4.3.2 Oscillatory Fields

The separated fields region contains two identical near-confocal Fabry-Perot cavities for the millimeter-wave radiation. We use the fundamental gaussian beam modes of the cavities as the two oscillatory fields for performing Ramsey spectroscopy. The separation between the centers of the cavities is 50.8 cm. We use standing-waves in cavities rather than running-waves in order to reduce the first-order Doppler effect and ensure a well defined spatial distribution of the radiation.

Each cavity has an input coupler made of a 500 line/inch copper mesh with a 60% open area. Each mesh is epoxied to the concave surface of a plano-concave fused silica lens with 25 mm diameter and 92 mm radius of curvature. To avoid unwanted focusing of the input beam, the plano-concave lens is sandwiched against a plano-convex lens of the same curvature. The end mirrors of the cavities are machined from copper, and also have a 92 mm radius of curvature.

The length of each cavity is $D \approx 80.4$ mm. The copper end mirrors are each mounted on three 80 pitch screws, using three springs to keep the assembly together. The three screws each have a 24 tooth gear which are meshed with one central 12 tooth gear. This gear, in turn, is coupled to a handle outside the vacuum chamber via a rotational feedthrough. One degree on the handle corresponds to about 0.4 μm of translation for the end mirror. The cavity resonance is about 2 μm wide.

We fine tune each cavity length by hand from outside the vacuum chamber while watching the atomic signal. We send about enough radiation for a $\pi/2$–pulse into the cavity to be tuned. We block the radiation into the other cavity. We then tune the cavity length such that the measured inversion is maximized. We estimate that this tuning procedure is accurate to less than or about one quarter of a degree, which translates to about 0.1 μm or approximately 5% of the cavity width. After tuning a cavity, we disengage the central gear from the cavity in order to avoid accidental mistunings. Note that because we cool the entire interaction region (including the cavities) to liquid helium temperature, the thermal expansion due to temperature fluctuations is negligible.

Using "Gaussian Beam Mode Analysis" [KL66] the frequencies of the cavity modes are given by

$$\nu_{mnq} = \frac{c}{2d}\left[q + 1 + \frac{1}{\pi}(1 + m + n)\cos^{-1}(1 - d/R)\right], \tag{4.10}$$

where m and n are the rectangular transverse mode numbers, q is the longitudinal mode number, R is the radius of curvature for the mirrors, and d is the cavity length. For the $n = 29 \to 30$ (256.3 GHz) transition we tune the length of the cavities to ≈ 80.43 mm and use the $TEM_{0,0,136}$ mode. For the $n = 27 \to 28$ (316.4 GHz) transition we tune the length of the cavities to ≈ 80.33 mm and use the $TEM_{0,0,168}$ mode. In the above two cases, the waist of the mode is 3.8 mm and 3.4 mm, respectively.

The size of the residual first-order Doppler effect depends on the size of the amplitude imbalance between the two counter-propagating running waves which form the standing-wave. As discussed in Sec. 3.8.2, this imbalance is determined by the reflectivity of the end mirror, r_e, and we now make an estimate for r_e. From measurements of the power reflected from the cavities as a function of the cavity length, we estimate that the finesse is about 300. Assuming that the reflectivities of the end mirror r_e and the input coupler r_i are approximately equal, $r_e = r_i = r$, we can write the cavity finesse as $\mathcal{F} = \pi/(1 - r^2)$. Solving for r when $\mathcal{F} = 300$, we find that $r \approx 0.995$. For more on the Doppler shift, see Sec. 3.8.2.

4.4 Millimeter-wave system

The millimeter-wave system produces the radiation which we couple into the cavities to form the oscillatory fields. We use the 4th and 5th harmonics of a Gunn diode to produce radiation at 256 GHz and 316 GHz, respectively. These two frequencies correspond to the $n = 27 \rightarrow 28$ and $n = 29 \rightarrow 30$ transition frequencies. We operate the Gunn diode at 64 GHz, and we phase lock it to a cesium clock (HP 5061A) using a frequency synthesizer (HP 8662), multipliers, and harmonic mixers.

4.4.1 Frequency chain

For the $n = 29 \rightarrow 30$ transition, the Gunn diode operates around $f_{Gunn} = 64{,}075.5$ MHz, and we use the fourth harmonic of this, about 256.3 GHz. For the $n = 27 \rightarrow 28$, the Gunn diode operates around $f_{Gunn} = 63{,}283.1$ MHz, and we use the fifth harmonic of this, about 316.4 GHz. We first consider the various frequencies involved in the chain for the $n = 29 \rightarrow 30$ transition, and then consider one small modification to the chain which is necessary for the $n = 27 \rightarrow 28$ transition.

We use the cesium clock output (10 MHz) as the frequency standard for the frequency synthesizer which produces two signals: one at a fixed frequency of exactly 640 MHz and another frequency f_{synth} that we tune near 75.5 MHz.

We multiply the 640 MHz signal by 10 up to 6.4 GHz and send it into the LO port of a harmonic mixer. The RF port of the harmonic mixer samples the Gunn diode frequency f_{Gunn}. The IF signal f_{IF} of the harmonic mixer comes from the mixing of the tenth harmonic of the LO with the RF. Thus, $f_{IF} = f_{Gunn} - 64$ GHz. When the frequency chain is locked, the $f_{IF} \approx 75.5 MHz$.

We send the f_{IF} signal, along with the f_{synth} signal, to a home-built "phase lock box". The function of the phase lock box is to maintain the control voltage to the Gunn diode such that the f_{IF} signal is phase locked with the f_{synth} signal. Thus, the phase lock box ensures that the frequency of the Gunn f_{Gunn} is exactly equal to 64 GHz + f_{synth}.

For the $n = 27 \rightarrow 28$ transition, there is one minor modification that we make to the frequency chain. For this transition frequency, the IF frequency is near $f_{IF} =$ 716.9 MHz, which is outside the bandwidth of the phase lock box. Before we send the IF signal to the phase lock box, we mix it with the 640 MHz signal in order to downconvert it to 76.9 MHz, which is within the bandwidth of the phase lock box. In this case, the phase lock box ensures that f_{Gunn} is exactly equal to 63.36 GHz - f_{synth}.

4.4.2 Millimeter-wave optics

We use both waveguide and quasi-optical techniques. To adjust the overall power, we use two wire-grid polarizers in conjunction with a waveguide attenuator. In order to mode-match the radiation into the two cavities, we pass the radiation through a cavity to reject unwanted modes. We balance the power in the two cavities by using a Frustrated Total Internal Reflection (FTIR) prism beamsplitter to adjust the relative input power to the two cavities.

4.5 Detection region

We detect the Rydberg atoms by selective electric field ionization. We use a field of about 1 kV/cm to ionize the atoms and then detect the ions with a charged particle detector. Since circular states of different n ionize at different fields, we are able to discriminate the upper circular state from the lower one. To accomplish this, we ramped the ionization field plates at a 4 degree angle, so that the upper circular state ionizes about 2 cm before the lower circular state. Two channeltrons detect the ions from the two different states, and the resolution between the two states is practically perfect.

We use a multi-channel scaler to group the counts into time bins based on the transit time, which is the time between laser excitation and detection. The time bins are 50 μs wide, and the atoms that we detect have transit times that range from about 0.2 ms to about 1.2 ms, for a total of about 20 time bins.

Chapter 5

Stark and Zeeman Effects

In this section we describe our experimental procedures for dealing with the Stark and Zeeman effects. The dependence of these two effects on the external electric and magnetic fields is discussed in Sec. 2.

5.1 Correction for Zeeman effect

To eliminate the first order Zeeman effect (see Sec. 2.3) we must alternate between taking data on the $\Delta m = +1$ and the $\Delta m = -1$ transitions and then take the average of the two results. To drive the $\Delta m = +1$ transition, we use the $m = +(n-1)$ circular state as the initial state. Similarly, to drive the $\Delta m = -1$ transition, we use the $m = -(n-1)$ circular state as the initial state. We perform two essentially simultaneous frequency scans on the $\Delta m = +1$ and the $\Delta m = -1$ circular state transitions, thus reducing our data's sensitivity to long term variations in the magnetic field. The scans are each about 15 kHz wide and are separated by about 400 kHz which is the first order Zeeman difference between them due to the applied field of $\approx$ 150 mG. The two frequency scans are made up of 60 points each, for a total of 120 points. We spend one second on each point and switch between the two transitions after each point. Finally, we typically average over ten such scans during a 20 minute run.

5.2 Correction for Stark effect

Circular state transitions are shifted by the second-order Stark effect. (There are no odd-order shifts, and the fourth-order shift is negligible.) In a field of magnitude F, the shift is

$$\nu_S = \alpha F^2, \tag{5.1}$$

where the constant α is computed from perturbation theory. We must apply a field $F > 50$ mV/cm in order to overwhelm the stray fields and keep the orientation of the circular states stable. Because the stray fields are non-uniform, the magnitude of the total field $F(x)$ is a function of x, the distance along the atomic beam. For Ramsey spectroscopy, the shift is averaged over the region between the two oscillatory fields, yielding $\overline{\nu_S} = \alpha\overline{F(x)^2}$, where $\overline{F(x)^2}$ is the average of $F(x)^2$ over the SOF region. We cannot measure $\overline{F(x)^2}$, but we can measure $\overline{F(x)}$ by performing Ramsey spectroscopy on a "near-circular" transition, which has a first-order Stark shift, as described in Sec. 2.2. Unfortunately, $\overline{F(x)^2} \neq \overline{F(x)}^2$ due to the non-uniformity of the stray fields.

To examine the difference between $\overline{F(x)^2}$ and $\overline{F(x)}^2$, we define $\vec{F}(x) = (V/d)\hat{z} + \vec{f_s}(x)$, where V is the voltage between the plates, d is the effective plate spacing, and $\vec{f_s}(x)$ is the field due to stray charge. We further define $\vec{f_s}(x) = [f_0 + f_{||}(x)]\hat{z} + \vec{f_\perp}(x)$, where $\vec{f_\perp}(x)$ is the perpendicular component of the field and $f_{||}(x)$ satisfies $\overline{f_{||}(x)} = 0$. If we assume that $f_s << V/d$, then we find:

$$\begin{aligned}
\overline{F(x)^2} &= \left(\frac{V}{d} + f_0\right)^2 + \overline{f_{||}(x)^2} + \overline{f_\perp(x)^2} && (5.2)\\
\overline{F(x)} &\approx \left(\frac{V}{d} + f_0\right) + \frac{1}{2}\frac{\overline{f_\perp(x)^2}}{V/d} && (5.3)\\
\overline{F(x)}^2 &\approx \left(\frac{V}{d} + f_0\right)^2 + \overline{f_\perp(x)^2} && (5.4)\\
\overline{F(x)^2} - \overline{F(x)}^2 &\approx \overline{f_{||}(x)^2}. && (5.5)
\end{aligned}$$

The difference is due to the variation in the $\hat{z}$ component of the stray field.

What we typically do to correct for the Stark effect is measure $\overline{F(x)}$ for four different biases: $V = \pm 1, \pm 0.1$ Volts. Then, by fitting this data to Eq. 5.3, we determine d, f_0, and $\overline{f_\perp(x)^2}$. Besides these values, we also need to know $\overline{f_\parallel(x)^2}$ in order to evaluate the second-order Stark correction by using Eq. 5.2. Unfortunately, we have no way to measure $\overline{f_\parallel(x)^2}$. For this reason, we have made efforts to keep it so small that the uncertainty in the shift due to it is negligible.

To keep the stray fields small, we thoroughly cleaned the plate surfaces and coated them with "Aerodag", which is made of graphite. We can perform a "spot check" on the level of the stray fields by measuring $f_\parallel(x)$ in the area of each oscillatory field. We do this by performing Rabi spectroscopy on the first-order Stark shifted near-circular transition. We measure the first-order Stark effect for positive and negative V, and we extract a value for $f_\parallel(x)$ in these regions which is in the range of 1-3 mV/cm. We find that the stray field in the area of each oscillatory field does not change significantly from day to day. From Ramsey resonance data on the near-circular state transition, we find values for f_0 and $\overline{f_\perp(x)^2}$. Typical sizes for these values are are: $|f_0| \approx 0.2$ mV/cm and $\overline{f_\perp(x)^2} \approx (4\ \text{mV/cm})^2$, and these values do not change significantly from day to day.

We cannot measure $\overline{f_\parallel(x)^2}$ itself; we simply assume that $\overline{f_\parallel(x)^2} \approx (3\ \text{mV/cm})^2$. We use this value because it is about the same size as $f_\parallel(x)$ as measured in the areas of the oscillatory fields, and also about the same size as f_0 and $\overline{f_\perp(x)^2}$. We assign a fractional uncertainty of 50% to the assumed value for $\overline{f_\parallel(x)^2}$. Explicitly, the value we use to correct for the Stark effect is

$$\overline{f_\parallel(x)^2} = 9.0(45)\ (\text{mV/cm})^2. \tag{5.6}$$

This value results in a correction of $\nu_{S\parallel} \approx 0.11(6)$ Hz for the $n_i = 27 \to n_f = 28$ transition and $\nu_{S\parallel} \approx 0.16(8)$ Hz for the $n_i = 29 \to n_f = 30$ transition. These shifts are almost negligible, and the uncertainty in them is negligible.

The above analysis leaves out the variation in the field due to any non-uniformity in the plate spacing d. For the small biases V that we use, this non-uniformity introduces a negligible error. From the construction of the plates, we expect the fractional difference between the RMS spacing and the average spacing to be less than 3×10^{-3}. For a typical bias of $V = 0.5$, the RMS value of the field due to the variation in the plate spacing is: $f_{RMS} \approx (3 \times 10^{-3})(0.5 \text{ V})/(2.443 \text{ cm}) = 0.6 \text{ mV/cm}$, which is negligible.

Another technique we use to correct for the Stark effect is simply to measure the circular state transition frequency for several different values of the bias V. These results fall on an upside-down parabola due to the second-order Stark shift. We fit the results to a parabola with d, f_0, and ν_0 as fit parameters, where ν_0 is the "field-free" frequency or "top" of the parabola. This technique is slightly less accurate than using the first-order Stark shifted transition to measure the field because it is unable to yield up either $\overline{f_\perp(x)^2}$ or $\overline{f_\parallel(x)^2}$. Also, it is slightly less precise for a given amount of running time.

In conclusion for this section, we can measure the average magnitude of the field $\overline{F(x)}$ but not the average of the squared magnitude of the field $\overline{F(x)^2}$. This means that we cannot measure the term $\overline{f_\parallel(x)^2}$ in Eq. 5.2. We do, however, have indirect indications of the size of this unknown term. From these indications, we estimate its effect to be about 0.4 Hz (which is at about the 1 part in 10^{12} level), and thus we consider it negligible and ignore it. If this term is much larger than we estimate then our results will be in considerable error.

Chapter 6

Lineshape with Interaction between Dipoles in the Atomic Beam

Our Ramsey resonance data exhibits a distortion which increases with the density of the atomic beam. We believe this distortion is due to the interaction between the coherent dipoles in the atomic beam that are created when the atoms pass through the first oscillatory field. This is a collective effect, closely related to super-radiance.

In this chapter we develop an approximate model for this effect and present a numerical model lineshape which semi-quantitatively accounts for the distortion in the resonance data. The geometry of our experiment is such that the dipole interactions are too complex to allow accurate modeling, and we can not use this model to extract cR_∞ with any confidence, especially from the data taken at higher densities.

This chapter culminates with a fit of the model lineshape to data on both the $n = 29 \rightarrow 30$ and $n = 27 \rightarrow 28$ transitions. We use data with the highest atomic densities that we achieved, for which the distortion is well pronounced. The model lineshape fits quite well to the data for the $n = 29 \rightarrow 30$ transition. The least-squares fitting routine converges readily and the goodness-of-fit parameter χ_r^2 is close to one. However, for some reason the model lineshape does not work well the $n = 27 \rightarrow 28$ transition. For this transition, the fitting routine does not converge reliably, and the

the χ_r^2 is not much better than a simple straight-line fit. The difference in the model performance is likely related to the difference in the fine structure splitting $\Delta\nu_{fs}$, which plays a large role in this effect.

As far as we know, this coherent dipole-dipole interaction has not been observed in any other precision resonance experiment. However, as discussed later in Sec. 6.5.4, we anticipate that the effect should be observable in atomic clocks based on hyperfine transitions at fractional accuracies greater than 10^{-15} and atomic densities greater than 10^9 cm^{-3}, under certain conditions.

6.1 Overview

6.1.1 Nature of the observed distortion

As an example of what the distortion in the resonance data can look like, Fig. 6-1 shows data for the lineshape phase Φ versus the interaction time T for both the $\Delta m_\ell = +1$ and $\Delta m_\ell = -1$ transitions. This data represents the highest atomic beam densities that we achieved, and the distortion is quite pronounced: ideally, the data should lie along an almost straight line. The model for the fit is that given in Eq. (3.82), assuming zero spin polarization ($\psi = 0$). The two data sets in Fig. 6-1 were fit simultaneously, and the reduced chi-square for the fit is $\chi_r^2 = 15.4$, which is unacceptable.

The shape of the distortion is similar to the shape produced by spin polarization, but we believe that spin polarization is not involved. We have three main reasons for believing this. First, we believe that the spin polarization is negligible, as is discussed in Sec. 7.3. Second, any imbalance between fine structure components caused by spin polarization would switch sign when the sign of Δm_ℓ is reversed. This is because the sign of the $\vec{L} \cdot \vec{S}$ interaction should change sign. However, we observe that the distortion to the phase Φ is the same for $\Delta m_\ell = +1$ and $\Delta m_\ell = -1$, as can be seen by comparing the residuals in Fig. 6-1. Third, our model for the lineshape with spin polarization, given in Eq. (3.82), does not fit the data well: If, for the fit shown in

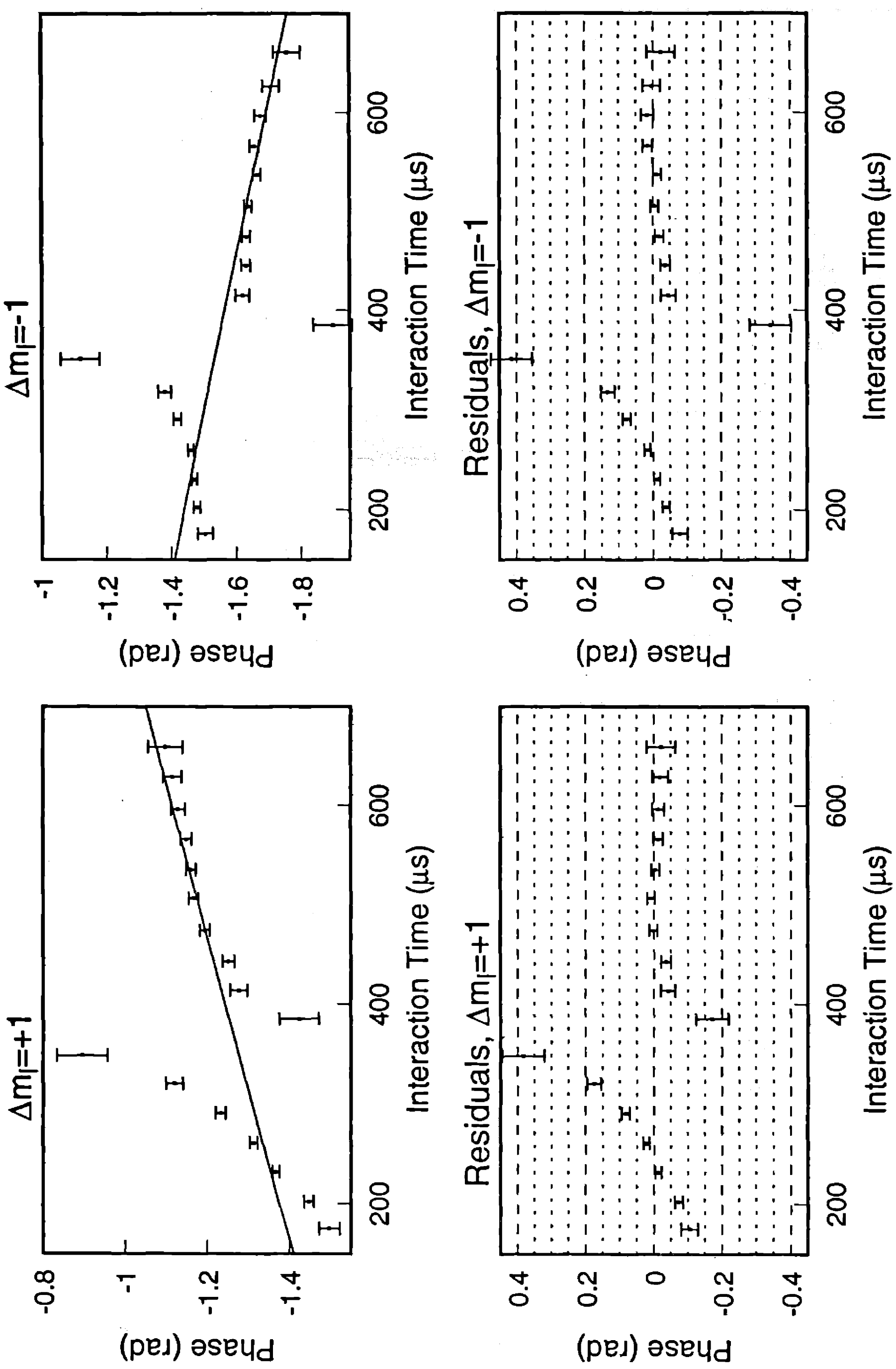

Figure 6-1: Example of distortion to phase of lineshape. This data represents the highest atomic beam densities that we achieved, and the distortion is quite pronounced. The data deviates markedly from the fit. The model for the fit, given in Eq. (3.82), does not include dipole interactions. The two data sets, the one on the left and the one on the right, were fit simultaneously and the reduced chi-square is $\chi_r^2 = 15.4$.

Fig. 6-1, we allow the spin polarization ψ to be fit, then the reduced chi-square for the fit is $\chi_r^2 = 5.59$, which is still unacceptable. Finally, as shown at the end of this chapter, our model for the lineshape with the dipole interactions produces a good fit.

6.1.2 Basic physical picture

Our basic physical picture is as follows: The first oscillatory field puts the atoms into a coherent superposition of the initial and final circular states, which have $\Delta m_\ell = +1$ or $\Delta m_\ell = -1$. Each atom has an electric dipole moment which rotates in the x-y (horizontal) plane. The dipoles rotate at the transition frequency. As an atom passes between the two oscillatory fields, it "sees" a field due to the distribution of other rotating electric dipoles. This field oscillates on resonance and perturbs the atoms, modifying the phase and inversion of the atoms, thereby distorting the Ramsey resonance data.

The fact that we do not entirely resolve fine structure complicates this picture. The lineshape that we detect is the sum the lineshapes for atoms with electron spin up and down. As discussed in section 2.4.4, the resonance frequency of atoms with electron spin up and atoms with electron spin down differ by the fine structure splitting $\Delta\nu_{fs}$. This means that the phase of the electric dipole for an atom with electron spin up evolves at a rate different by $\Delta\nu_{fs}$ from the same atom with electron spin down. Thus, the field "seen" by an atom is the sum of the field due to the electric dipoles of atoms with electron spin up and down. Also, the perturbation to an atom due to the field depends on its own spin state. This is because the perturbation to an atom depends not only on the phase and magnitude of the perturbing field, but also on the phase and magnitude of the atom's electric dipole.

6.1.3 Nature of the model

The model we present in this chapter is a perturbative model and good only to first-order: i.e., we calculate the perturbation to the atoms due to the field of the unperturbed atoms. A second-order model would go on to to calculate the "new" field due to the perturbed atoms and then determine the effect of the new field on the atoms. In an "exact" model, on the other hand, the state of the atoms and the fields they produce would be consistent. We have not developed an exact model or even a second order model because the geometry of the atomic beam makes the problem too complex. Because our model is only first-order, it is only good when the perturbations to the atoms are small, where the meaning of "small" is defined later in Eqs. (6.33–6.34). The geometry of the atomic beam complicates the problem, making it necessary to numerically calculate the electric field due to the distribution of dipoles.

For reasons of simplicity and also because of the time-consuming nature of the numerical integration, we make gross approximations in order to make the problem tractable. Perhaps the biggest approximation is that the model only considers the perturbation to atoms which travel exactly along the axis of the atomic beam. In other words, while we calculate the field due to all the unperturbed atoms, we calculate the perturbation to only the atoms on the axis of the atomic beam. Experimentally, we detect a range of trajectories—not just trajectories exactly along the axis. We find that atoms which are near the axis see fields with, for the most part, similar amplitudes and phases to atoms which are on-axis. Hence, we expect that this approximation is fairly good.

6.2 The field due to atomic electric dipoles

In this section, we find an integral expression for the rotating field due to a distribution of rotating dipoles. First, however, we derive an expression for the rotating electric field of a single rotating dipole.

6.2.1 The co-rotating field of a rotating dipole

We start by giving an expression for the electric field of a rotating electric dipole. In the rotating-wave approximation, we are interested only in the "co-rotating" component of the electric field. For example, for the $\Delta m_\ell = +1$ transition, all the dipoles are rotating in the counter-clockwise direction as viewed from above, and at any given point we are interested only in the counter-clockwise component of the electric field; the clockwise component is the "counter-rotating" component and has essentially no effect on the atoms. In other words, if we write the electric field at a given point $\vec{r}$ as

$$\vec{E}(\vec{r},t) = \left(E_+ e^{-i\phi_+}\hat{\epsilon}_+ + E_- e^{-i\phi_-}\hat{\epsilon}_-\right) e^{-i\omega_0 t} \tag{6.1}$$

then we are interested only in the projection of $\vec{E}(\vec{r},t)$ along $\hat{\epsilon}_+$: $\hat{\epsilon}_+^* \cdot \vec{E}(\vec{r},t) = E_+ e^{-i(\omega_0 t+\phi_0)}$.

From Jackson[Jac98], the electric field at position $\vec{r}$ due to an electric dipole at the origin is given by

$$\vec{E}(\vec{r},t) = \frac{1}{4\pi\epsilon_0}\left\{k^2(\hat{r}\times\vec{p})\times\hat{r}\frac{1}{r} + [3\hat{r}(\hat{r}\cdot\vec{p})-\vec{p}]\left(\frac{1}{r^3}-\frac{ik}{r^2}\right)\right\}e^{ikr}, \tag{6.2}$$

where $k = \omega_0/c$ is the wavenumber and $r = |\vec{r}|$. We take the dipole to be complex:

$$\vec{p} = \hat{\epsilon}_\pm p_0 e^{-i\omega_0 t}, \tag{6.3}$$

where p_0 is the real magnitude of the dipole and the ± sign depends on the sign of Δm_ℓ.

We label the co-rotating field amplitude as $\mathcal{E}(\vec{r},t)$ and define it as $\mathcal{E}(\vec{r},t) \equiv (\hat{\epsilon}_\pm e^{-i\omega_0 t})^* \cdot \vec{E}(\vec{r},t)$, where the $(\pm)$ sign depends on the sign of Δm_ℓ. Using some vector algebra and the properties of the $\hat{\epsilon}_\pm$ unit vectors, the co-rotating field amplitude at position $\vec{r}$ due to a rotating dipole at the origin is, regardless of the sign of Δm_ℓ,

$$\mathcal{E}(\vec{r},t) = \sqrt{2}\frac{p_0}{4\pi\epsilon_0}\left[\left(1-\frac{\sin^2\theta}{2}\right)\frac{k^2}{r} + \left(\frac{3}{2}\sin^2\theta - 1\right)\left(\frac{1}{r^3}-\frac{ik}{r^2}\right)\right]e^{ikr}, \tag{6.4}$$

where p_0 is the magnitude of the rotating dipole and θ is the polar angle, i.e. the angle of $\vec{r}$ from $\hat{z}$ where $\hat{z}$ points up. It is easy to show that Eq. (6.4) also gives the co-rotating field at the origin due to a rotating dipole at position $\vec{r}$.

Eq. (6.4) gives the co-rotating field amplitude of a *classical* rotating dipole of magnitude p_0. What we actually need to consider, however, are quantum mechanical atomic dipoles. For the classical dipole magnitude p_0 in Eq. (6.4), we use the magnitude of the expectation value of the electric dipole moment, $|\langle\vec{p}\rangle|$. Specifically, we use

$$p_0 = \sqrt{\langle p_x\rangle^2 + \langle p_y\rangle^2 + \langle p_z\rangle^2}. \tag{6.5}$$

Using the expectation value of the dipole as given in Eqs. (3.6–3.6) and the matrix elements from Eqs. (3.3–3.5), the dipole magnitude is

$$p_0 = ea_0 n^2 ab. \tag{6.6}$$

6.2.2 The co-rotating field due to a distribution of rotating dipoles

Next, we discuss our procedure for calculating the co-rotating electric field amplitude $\mathcal{E}(\vec{r},t)$ due to all the atomic dipoles in the atomic beam. What we actually calculate is the *macroscopic* electric field: i.e., the electric field averaged over some small volume centered on the point in question, where the length scale of the averaging volume is much smaller than both the smallest length scale of the atomic beam and the wavelength of the radiation. This amounts to treating the atomic beam as a continuous, polarized medium (thereby ignoring the microscopic structure of the electric field) and integrating over the entire polarized medium.

Expression for the field at the origin

To calculate the amplitude of the co-rotating field at the origin we must integrate Eq. (6.4) over the volume of the atomic beam, weighted by the atomic beam density. The integral is, taking the origin to be the point where we wish to calculate the field,

$$\mathcal{E}(t) = \frac{\sqrt{2}}{4\pi\epsilon_0}\int d\vec{r}\; \rho(\vec{r},t)p_0(\vec{r},t)\left[\left(1-\frac{\sin^2\theta}{2}\right)\frac{k^2}{r} + \left(\frac{3}{2}\sin^2\theta - 1\right)\left(\frac{1}{r^3}-\frac{ik}{r^2}\right)\right]e^{ikr}, \tag{6.7}$$

where $\rho(\vec{r},t)$ is the atomic density, $p_0(\vec{r},t)$ is the expectation value of the dipole magnitude, and both $\rho(\vec{r},t)$ and $p_0(\vec{r},t)$ are complicated functions of position $\vec{r}$ and time t. The density $\rho(\vec{r},t)$ depends on the geometry of the atomic beam. Because the beam is pulsed, $\rho(\vec{r},t)$ also depends on time t and the velocity distribution of the atomic beam. The dipole magnitude at point $\vec{r}$ and time t, $p_0(\vec{r},t)$, depends on which part of the standing-wave oscillatory field an atom at point $\vec{r}$ and time t went through. Also, $p_0(\vec{r},t)$ depends on how long the atom spent in the first oscillatory field.

Behavior of the integral near $r = 0$

The integrand has a singularity at $r = 0$. Near $r = 0$ we can consider $\rho(\vec{r},t)$ and $p_0(\vec{r},t)$ as constants, so that we can write the integral in terms of r and θ. The radial integrals for the $1/r$ and $1/r^2$ terms are integrable, but the radial integral for the $1/r^3$ term is not integrable—it blows up. However, the angular dependence of the $1/r^3$ (and the $1/r^2$ term) is such that the angular integral vanishes, so that the end result of the integral for the $1/r^3$ term is indeterminate.

The $1/r^3$ term is the "static" term of the oscillating dipole field. It gives rise to the *contact interaction* between dipoles, which is described by a Dirac delta function potential. Perhaps the most familiar example of the contact interaction is the hyperfine interaction for the ground state of hydrogen which is exclusively due to the contact interaction. We believe that in our case, we can ignore the contact interaction. We expect that there should be little overlap of two atomic wavefunctions because as two hydrogen atoms approach each other, the Coulomb repulsion between the protons should prevent any contact.

Co-rotating field at arbitrary point $\vec{r}_0$

The co-rotating field at the origin is given by the integral in Eq. (6.7). We generalize this expression to give the field at point $\vec{r}_0$:

$$\mathcal{E}(\vec{r}_0,t) = \frac{\sqrt{2}}{4\pi\epsilon_0}\int d\vec{r}\,'\ \rho(\vec{r},t)p_0(\vec{r},t)\left[\left(1-\frac{\sin^2\theta'}{2}\right)\frac{k^2}{r'} + \left(\frac{3}{2}\sin^2\theta' - 1\right)\left(\frac{1}{r'^3} - \frac{ik}{r'^2}\right)\right]e^{ikr'}, \tag{6.8}$$

where the integral is over $\vec{r}\,' = \vec{r} - \vec{r}_0$, θ' is the polar angle of $\vec{r}\,'$, and $r' = |\vec{r}\,'|$.

6.3 First-order solution to the Bloch vector equation of motion

In this section we examine the first-order solution of the Bloch vector equation of motion. From Eq. (3.25), the Bloch vector equation of motion is $\dot{\vec{s}} = \vec{\Omega} \times \vec{s}$. The general expression for the pseudo torque $\vec{\Omega}$ for a $\Delta m_\ell = \pm 1$ electric dipole transition in a frame rotating at frequency ω_r is given in Eqs. (3.33–3.35).

We take ω_r to be equal to the resonance frequency ω_0. We take the phase of the rotating frame such that the unperturbed Bloch vector lies in the x-z plane. We take the frequency of the field ω to be equal to the resonance frequency ω_0. Hence, the variables Δ_{0r} and Δ_r in Eqs. (3.33–3.35) are given by $\Delta_{0r} \equiv \omega_r - \omega_0 = 0$ and $\Delta_r \equiv \omega - \omega_r = 0$. (In general, ω is only loosely the "frequency of the field". This is because in general we allow the phase of the field, ϕ, to be time-dependent. If Φ is the phase of the field, then the instantaneous frequency is strictly defined as the time-derivative of Φ: $\dot{\Phi} = \omega + \dot{\phi}$.) With these values, the pseudo torque is

$$\Omega_1 = \mp\omega_{R\pm}\cos[\oplus\,\delta_{fs}t/2 + \phi_\pm] \tag{6.9}$$

$$\Omega_2 = -\omega_{R\pm}\sin[\oplus\,\delta_{fs}t/2 + \phi_\pm] \tag{6.10}$$

$$\Omega_3 = 0, \tag{6.11}$$

where the $\mp$ operand and the $\pm$ subscripts depend on the sign of Δm_ℓ, the $\oplus$ operand depends on the fine structure component, $\phi_\pm$ is the phase of the co-rotating field amplitude $\mathcal{E}(t)$, and $\omega_{R\pm}$ is the Rabi frequency. The Rabi frequency $\omega_{R\pm}$ is given by the expression in Eq. (3.32), where $E_\pm$ is the absolute value of the co-rotating field amplitude $|\mathcal{E}|$.

We now expand the equation of motion in terms of the Rabi frequency $\omega_{R\pm}$, and keep terms up to first-order. To do this, we replace $\omega_{R\pm}$ with $\lambda\omega_{R\pm}$, where λ is a dimensionless constant which we will later set equal to one. The expression for the pseudo-torque in Eqs. (6.9–6.11) becomes

$$\begin{aligned} \Omega_1 &= \mp\lambda\omega_{R\pm}\cos[\oplus\, \delta_{fs}t/2 + \phi_\pm] && (6.12)\\ \Omega_2 &= -\lambda\omega_{R\pm}\sin[\oplus\, \delta_{fs}t/2 + \phi_\pm] && (6.13)\\ \Omega_3 &= 0, && (6.14) \end{aligned}$$

We expand the Bloch vector in terms of λ:

$$\vec{s} = \vec{s}^{\,(0)} + \lambda\vec{s}^{\,(1)} + \lambda^2\vec{s}^{\,(2)} + \cdots. \tag{6.15}$$

We plug Eqs. (6.12–6.15) into the equation of motion, and we keep only up to first-order in λ. Then, separating the powers of λ, we arrive at equations for $\vec{s}^{\,(0)}$ and $\vec{s}^{\,(1)}$.

The zeroth-order equations of motion are simple:

$$\dot{s}_1^{(0)}(t=0) = 0, \quad \dot{s}_2^{(0)}(t=0) = 0, \quad \dot{s}_3^{(0)}(t=0) = 0, \tag{6.16}$$

Without the perturbation, the Bloch vector is constant. We write the initial conditions as

$$s_1^{(0)}(t=0) = A_1, \quad s_2^{(0)}(t=0) = A_2 = 0, \quad s_3^{(0)}(t=0) = A_3. \tag{6.17}$$

As mentioned earlier, we take $A_2 = 0$ corresponding to the Bloch vector to starting out in the x-z plane. The zeroth-order solution is

$$s_1^{(0)}(t) = A_1, \quad s_2^{(0)}(t) = 0, \quad s_3^{(0)}(t) = A_3, \tag{6.18}$$

The first-order equations of motion are:

$$\dot{s}_1^{(1)} = -A_3\omega_{R\pm} \sin[\bigoplus \delta_{fs}t/2 + \phi_\pm] \tag{6.19}$$

$$\dot{s}_2^{(1)} = \pm A_3\omega_{R\pm} \cos[\bigoplus \delta_{fs}t/2 + \phi_\pm] \tag{6.20}$$

$$\dot{s}_3^{(1)} = +A_1\omega_{R\pm} \sin[\bigoplus \delta_{fs}t/2 + \phi_\pm]. \tag{6.21}$$

If we ignore fine structure by taking $\delta_{fs} = 0$ and if we also assume that $\omega_{R\pm}$ and $\phi_\pm$ are independent of time t, then the change in $\vec{s}^{\,(1)}$ is linear in time:

$$s_1^{(1)} = -tA_3\omega_{R\pm} \sin\phi_\pm \tag{6.22}$$

$$s_2^{(1)} = \pm tA_3\omega_{R\pm} \cos\phi_\pm \tag{6.23}$$

$$s_3^{(1)} = +tA_1\omega_{R\pm} \sin\phi_\pm. \tag{6.24}$$

In this case, given $\vec{s}^{\,(0)}$ and $\vec{s}^{\,(1)}$, we find the first-order solution from Eq. (6.15) to be the following sum $\vec{s} = \vec{s}^{\,(0)} + \lambda\vec{s}^{\,(1)}$. Setting $\lambda = 1$, the components of $\vec{s}$ are to first-order:

$$s_1 = A_1 - tA_3\omega_{R\pm} \sin\phi_\pm \tag{6.25}$$

$$s_2 = \pm tA_3\omega_{R\pm} \cos\phi_\pm \tag{6.26}$$

$$s_3 = A_3 + tA_1\omega_{R\pm} \sin\phi_\pm. \tag{6.27}$$

In general, when $\omega_{R\pm}$ and $\phi_\pm$ are time-dependent and $\delta_{fs} \neq 0$, the solution is found by integrating Eqs. (6.19–6.21).

6.4 Nature of the effect on the Ramsey resonance data

6.4.1 Overview of the effect on the resonance data

Recall the method that we use for determining the transition frequency from the Ramsey resonance data, which is summarized in Sec. 3.12. Basically, we measure the phase Φ_j of the sinusoidal lineshape for several different time bins j and then find the slope of Φ_j versus interaction time, which determines the transition frequency.

The interactions between the atomic dipoles (that occur while the atoms are between the oscillatory fields) perturb the phase of the sinusoidal lineshape. The effect of these interactions is not as straightforward as a simple frequency shift, which would only perturb the slope of the phase Φ_j versus interaction time. Instead, the perturbation to the phase Φ_j is a complicated function of the interaction time. The effect can be broken down into two somewhat distinct mechanisms for perturbing the phase of the lineshape.

The first mechanism is relatively straightforward: The interactions perturb the phase of the dipoles, and hence the phase of the lineshape. However, this mechanism is complicated in that the size of the phase perturbation is a complicated function of the interaction time.

The second mechanism is less straightforward: The interactions effectively last on the order of 100 μs, which corresponds to a time-limited bandwidth of $(2\pi\, 100\ \mu\text{s})^{-1} \approx 1.6$ kHz. This bandwidth is comparable to the fine structure frequency difference, given in Eq. (2.44). Hence, the fine structure plays a role in the interaction between dipoles that cannot be ignored: the perturbation resolves the fine structure so that the inversion and the phase of the atoms depends on which fine structure state is occupied. In other words, the effect can give an atom with electron spin up a different inversion than the same atom with electron spin down. This results in different lineshape amplitudes for the two spin states. The difference in lineshape amplitude for atoms with spin up and spin down mimics the effects that polarized electrons have on the Ramsey resonance lineshape.

The second mechanism can be viewed as generating a "pseudo polarization"

$$\psi = \frac{A_+ - A_-}{A_+ + A_-}, \tag{6.28}$$

where A_+ and A_- are the lineshape amplitudes for the high and low frequency fine structure components, respectively. Recall that in the case of real spin polarization, $\psi = P_+ - P_-$ where P_+ and P_- are the probabilities for the two spin components.

6.4.2 Perturbation to the Bloch vector angles Θ and Φ

As described in Sec. 3.2.3, we define the Bloch vector angles Θ and Φ to be the polar and azimuthal angles:

$$\begin{aligned} \Theta &\equiv \cos^{-1} s_3 && (6.29) \\ \Phi &\equiv \tan^{-1} \frac{s_2}{s_1}. && (6.30) \end{aligned}$$

When we perform the Ramsey resonance method, the atoms start out in the lower energy state $|b\rangle$. In the rotating frame (and in the lab frame) the Bloch vector points straight down: $\vec{s} = (0, 0, -1)$. The polar angle is π and the azimuthal angle is undefined. The first oscillating field induces a rotating electric dipole in each atom. At this point, the Bloch vector phase (or equivalently, the dipole phase) Φ of every atom is determined solely by the phase of the oscillatory field, and the polar angle Θ of each atom is determined by how much a of pulse the atom "saw". For example, a $\pi/2$–pulse would rotate Θ from π to $\pi/2$, (from down to horizontal). How much of a pulse a particular atom gets depends on its velocity and on which part of the standing wave the atom intersects. For instance, an atom intersecting at a node gets no pulse at all.

What we are interested in is the perturbation to the Bloch vector after the time T that it takes for an atom to travel from the first oscillatory field to the second. Because we have two fine structure components, we need two Bloch vectors to describe the

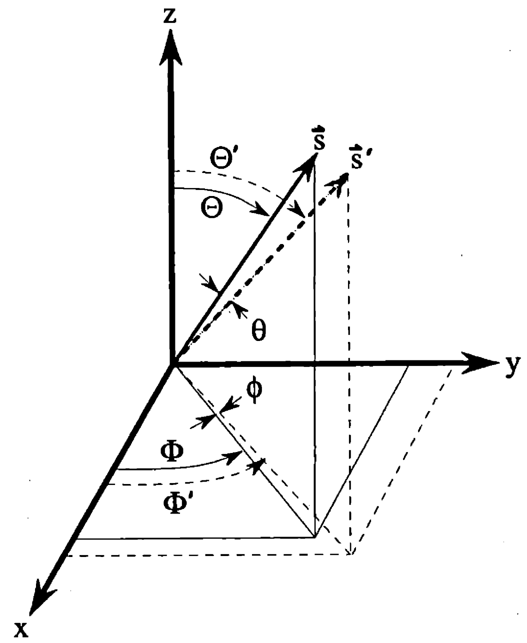

Figure 6-2: Bloch vector angles. The angles Φ and Θ are for the unperturbed Bloch vector $\vec{s}$. The angles Φ' and Θ' are for the perturbed Bloch vector $\vec{s}\,'$. The perturbation angles ϕ and θ are the difference: $\phi = \Phi' - \Phi$ and $\theta = \Theta' - \Theta$.

evolution of the atoms between the oscillating fields. We use subscripts to denote the two fine structure components. We label the unperturbed Bloch vector angles at time T as $\Theta_\pm$ and $\Phi_\pm$, where $+/-$ is for the high/low frequency component. Similarly, to denote the perturbed angles at time T, we use $\Theta'_\pm$ and $\Phi'_\pm$. We define new variables to be the difference between the perturbed and unperturbed Bloch vector angles:

$$\theta_\pm = \Theta'_\pm - \Theta_\pm \tag{6.31}$$

$$\phi_\pm = \Phi'_\pm - \Phi_\pm. \tag{6.32}$$

These variables isolate the perturbation, and we refer to these angles as the perturbation angles. Figure 6-2

In the limit of small perturbations, which is a requirement for our first-order model, the perturbation angles are generally much less than one:

$$\theta_\pm \ll 1 \tag{6.33}$$

$$\phi_\pm \ll 1. \tag{6.34}$$

We also define new variables to be the average and difference of the the perturbation angles:

$$\bar{\theta} = \frac{\theta_+ + \theta_-}{2} \tag{6.35}$$

$$\bar{\phi} = \frac{\phi_+ + \phi_-}{2} \tag{6.36}$$

$$\delta\theta = \frac{\theta_+ - \theta_-}{2} \tag{6.37}$$

$$\delta\phi = \frac{\phi_+ - \phi_-}{2}. \tag{6.38}$$

We use these variables later, in Eqs. (6.46—6.49).

6.4.3 Model for the phase of the lineshape, Φ_j as a function of the interaction time T_j

The Bloch vector representation of the Ramsey resonance method is given in Eq. (3.54). For purposes here, we use an approximate version of this equation. We assume that $\Delta \ll \omega_R$. Then, to zeroth-order in Δ/ω_R, the Bloch vector representation in Eq. (3.54) simplifies to

$$\vec{s}(t = T + 2\tau) = \mathcal{R}(\hat{x}, \omega_R\tau)\ \mathcal{R}(\hat{z}, \mp(\Delta T - \phi_0))\ \mathcal{R}(\hat{x}, \omega_R\tau)\ \vec{s}(t = 0). \tag{6.39}$$

Now we modify this equation to include the perturbation angles $\phi_\pm$ and $\theta_\pm$. Assuming that the initial state is the lower state, $\vec{s}(t = 0) = (0, 0, -1)$, we can write

$$\vec{s}(t = T + 2\tau) = \mathcal{R}(\hat{x}, \omega_R\tau)\ \mathcal{R}(\hat{z}, \mp(\Delta T - \phi_0) + \phi_\pm))\ \mathcal{R}(\hat{x}, \omega_R\tau - \theta_\pm)\ \vec{s}(t = 0). \tag{6.40}$$

Going from right to left, the first rotation represents the action of the first oscillatory field plus the perturbation to the polar angle, $\theta_\pm$ where the ± subscript depends on the fine structure component. The second rotation $\mathcal{R}(\hat{z}, \mp(\Delta T - \phi_0) + \phi_\pm)$ corresponds to both the unperturbed evolution of the dipole moment and the perturbation to the phase $\phi_\pm$. The ± subscript depends on the fine structure component, while the ∓

operator depends on the sign of Δm_ℓ. Finally, the third rotation represents the action of the second oscillatory field, which is characterized by the same Rabi frequency and duration as the first.

The inversion after time $T + 2\tau$ is given by the z-component of the Bloch vector:

$$I(\omega) = \sin(\omega_R\tau - \theta_\pm)\sin(\omega_R\tau)\cos(\Delta T - \phi_0 \mp \phi_\pm) - \cos(\omega_R\tau - \theta_\pm)\cos(\omega_R\tau), \quad (6.41)$$

where the $\mp$ operator depends on the sign of Δm_ℓ. We rewrite this in the form of the basic lineshape model, given in Eqs. (3.70-3.71). The perturbed lineshape model for a single time bin j and a single fine structure component is:

$$I_{j\pm}(\delta) = A_{j\pm}\cos(\delta T_j - \Phi_{j\pm}) + B_{j\pm} \quad (6.42)$$

$$\text{where} \quad \Phi_{j\pm} = \delta_0 T_j \oplus \frac{\delta_{fs}T_j}{2} \pm \phi_\pm + \phi_0, \quad (6.43)$$

where the $\oplus$ operator depends on the fine structure component and the $\pm$ operator depends on the sign of Δm_ℓ. The lineshape amplitude $A_{j\pm}$ and offset $B_{j\pm}$ are

$$A_{j\pm} = \sin\left(\frac{\pi T_j}{2T_0} - \theta_\pm\right)\sin\left(\frac{\pi T_j}{2T_0}\right), \quad (6.44)$$

$$B_{j\pm} = \cos\left(\frac{\pi T_j}{2T_0} - \theta_\pm\right)\cos\left(\frac{\pi T_j}{2T_0}\right), \quad (6.45)$$

where T_0 is the interaction time for which atoms receive a $\pi/2$–pulse at each oscillatory field.

Summing the two fine structure components, we find the total lineshape, $I_j(\delta) = I_{j+}(\delta) + I_{j-}(\delta)$, and write it in terms of the angles in Eqs. (6.35–6.38):

$$I_j(\delta) = A_j\cos(\delta T - \Phi_j) + B_j \quad (6.46)$$

$$\text{where} \quad \Phi_j = \delta_0 T_j + \phi_{fs} \pm \bar{\phi} + \phi_0, \quad (6.47)$$

where A_j and B_j are arbitrary fit parameters, the "fine structure phase" ϕ_{fs} is given by

$$\phi_{fs} = \tan^{-1}\left[\psi \tan\left(\frac{\delta_{fs}T_j}{2} \pm \delta\phi\right)\right], \tag{6.48}$$

and the pseudo polarization ψ is given by

$$\psi = \frac{A_+ - A_-}{A_+ + A_-} = -\cot\left(\frac{\pi T_j}{2T_0} - \bar{\theta}\right)\tan\delta\theta. \tag{6.49}$$

6.5 Application of model in a simple case

In order to illustrate the essentials of our model, we now apply it to a simple case which can be solved analytically. For simplicity, we ignore fine structure. We assume the distribution of circular atoms is a sphere of fixed radius R; and we consider the perturbation to an atom located at the center only. We take the density to be

$$\rho(\vec{r}, t) = \begin{cases} \rho_0 & : \quad r < R \\ 0 & : \quad r >= R \end{cases}. \tag{6.50}$$

We take the expectation value of the dipole magnitude to be constant

$$p_0(\vec{r}, t) = p_0. \tag{6.51}$$

6.5.1 The co-rotating field amplitude $\mathcal{E}(t)$

The co-rotating electric field is given by $\vec{E}_\pm = \mathcal{E}(t)\hat{\epsilon}_\pm$, where the ($\pm$) sign depends on the sign of Δm_ℓ, which we leave arbitrary. To find the amplitude $\mathcal{E}(t)$ of the co-rotating field at the center of the spherical distribution, we plug $\rho(\vec{r}, t)$ and $p_0(\vec{r}, t)$ into Eq. (6.7). We integrate over the angles first. Because the sphere is uniform, the angular integrals for the $1/r^2$ and $1/r^3$ terms vanish. Of course, the $1/r^3$ radial integral blows up at the origin, but we ignore this because we assume that there is a hard core interaction which prevents overlap of the atoms. Thus we are left with the

$1/r$ term:

$$\begin{aligned}
\mathcal{E}(t) &= \frac{\sqrt{2}}{4\pi\epsilon_0}\rho p_0(2\pi)\left(\frac{4}{3}\right)k^2\int_0^R dr\ r^2\frac{e^{ikr}}{r} && (6.52)\\
&= \frac{2\sqrt{2}}{3\epsilon_0}\rho p_0\left[-1+e^{ikR}\left(1-ikR\right)\right]. && (6.53)
\end{aligned}$$

If we take the radius to be $R = 1/k$, then the amplitude of the co-rotating field is

$$\mathcal{E}(t) \approx \frac{2\sqrt{2}}{3\epsilon_0}\rho p_0\left[0.486e^{-i(-0.668)}\right]. \qquad (6.54)$$

In our experiment, the highest density of circular atoms is on the order of 10^5 cm^{-3}. For a $\pi/2$–pulse, the magnitude of the dipole moment, p_0, takes on a maximum value of $p_0 = ea_0n^2/2 = 3.7 \times 10^{-27}$C·m. Using these values, the absolute value of the field amplitude is $|\mathcal{E}(t)| = (1.9 \times 10^{-5})$ V/m. Examining Eq. (6.3) and Eq. (6.54), the phase of the rotating field lags behind the rotating dipoles by 0.668 radians.

6.5.2 First-order solution to the Bloch vector equation of motion

In this section we examine the first-order solution. The general first-order solution is discussed in Sec. 6.3.

First we consider the pseudo torque $\vec{\Omega}$. The form of the pseudo torque is given in Eqs. (6.9–6.11). From Eq. (6.54), the phase is $\phi_\pm = -0.668$. The Rabi frequency $\omega_{R\pm}$ is given by the expression in Eq. (3.32), where $E_\pm = |\mathcal{E}|$. We have

$$\begin{aligned}
\omega_{R\pm} &= \frac{4\rho}{3\epsilon_0\hbar}\left(\frac{1}{2}ea_0n^2\right)^2(0.486) && (6.55)\\
&\approx (9\times 10^2)\ \mathrm{s}^{-1}.
\end{aligned}$$

(This value for $\omega_{R\pm}$ is actually on the same order of magnitude as $\omega_{R\pm}$ in our experiment at the highest densities.) The pseudo torque is then

$$\vec{\Omega} = (9\times 10^2)\ \mathrm{s}^{-1}(\mp 0.785, -0.619, 0), \qquad (6.56)$$

or equivalently,

$$\Omega_1 = \mp 707\ \mathrm{s}^{-1}, \quad \Omega_2 = -557\ \mathrm{s}^{-1}, \quad \Omega_3 = 0. \tag{6.57}$$

Given that $\vec{\Omega}$ is constant, we can use the first-order solution as given in Eqs. (6.25–6.27). The solution depends on the initial conditions via A_1 and A_3 ($A_2 = 0$). Next, we examine two different cases.

Case 1: $\pi/2$–pulse

If the first oscillatory field gives the atoms a $\pi/2$–pulse, then the initial conditions are $s_1^{(0)} = 1$ and $s_2^{(0)} = s_3^{(0)} = 0$, so that $A_1 = 1$ and $A_2 = A_3 = 0$. To first-order, the phase of the Bloch vector, given by $\Phi(t) = \tan^{-1}\frac{s_2(t)}{s_1(t)}$, is unperturbed. The phase Φ starts at zero and remains at zero. The inversion of the Bloch vector, given by the vertical component $s_3(t)$, is perturbed to first-order. Given the pseudo torque in Eq. (6.57), we calculate the inversion at $t = 0.5$ ms, which is a typical interaction time in our experiment. we find: $s_3(t = 0.5\ \text{ms}) = -\Omega_2 t = 0.279$. The perturbation angles are: $\theta \approx -0.283$ and $\phi = 0$, which loosely satisfy the "small perturbation" criterion in Eqs. (6.33–6.34) (ignoring the ± sign in this equation which corresponds to fine structure). This perturbation to the inversion does not affect the phase of the Ramsey resonance lineshape—it affects only the amplitude.

Case 2: $\pi/4$–pulse

If the first oscillatory field gives the atoms a $\pi/4$–pulse, then the initial conditions are $s_1^{(0)} = 1/\sqrt{2}$, $s_2^{(0)} = 0$, $s_3^{(0)} = -1/\sqrt{2}$. To first-order, the phase at time t is $\Phi(t) = \Omega_1 t$ and the inversion is $s_3 = -\frac{1}{\sqrt{2}}(1 + \Omega_2 t)$. Because the atoms are given only a $\pi/4$–pulse, their dipole moments are weaker by a factor of $\sqrt{2}$. This means that the electric field is weaker by a factor of $\sqrt{2}$, and hence the Ω_1 and Ω_2 components of the pseudo torque are weaker by a factor of $\sqrt{2}$ compared to Eq. (6.57). Using this weaker pseudo torque, the phase at time $t = 0.5$ ms is: $\Phi(t = 0.5\ \text{ms}) = \mp 0.250$, where the $\mp$ sign depends on Δm_ℓ, and the inversion is $s_3(t = 0.5\ \text{ms}) = -0.568$. The perturbation angles are then: $\phi = \mp 0.250$ and $\theta \approx -0.139$. which loosely satisfy the "small perturbation" criterion in Eqs. (6.33–6.34) (ignoring the ± sign in this equation which corresponds to fine structure).

6.5.3 Perturbation to the Ramsey resonance data

In the case presented here, the effect on the resonance data is quite simple. The lineshape is given by Eqs. (6.42–6.43), but with the ± subscripts dropped and $\delta_{fs} = 0$ because we are ignoring fine structure.

The polar perturbation angle, θ, only has the effect of perturbing the amplitude of the lineshape, which is a benign effect. However, the azimuthal perturbation angle, ϕ, causes an apparent shift in the transition frequency. We label this shift as ν_{d-d}, where the subscript "*d-d*" stands for dipole-dipole. The shift arises because the perturbation $\delta\phi$ modifies the slope of the lineshape phase Φ_j with respect to the interaction time T_j (where j denotes the time bin).

We now consider the ν_{d-d} for "case 2" above ($\pi/4$–pulse). The new slope, which we label as δ_0', is given by

$$\begin{aligned} \delta_0' &= \delta_0 \pm \frac{d}{dT}\delta\phi \qquad (6.58) \\ &= \delta_0 \pm \Omega_1. \qquad (6.59) \end{aligned}$$

This corresponds to a frequency shift of

$$\nu_{d-d} = \pm\Omega_1/(2\pi) \approx -10^2 \text{ Hz.} \qquad (6.60)$$

Given that the transition frequency is about 3×10^{11} Hz, this is a fractional shift of about -3×10^{-10}. The frequency shift is independent of the sign of Δm_ℓ.

6.5.4 Application to a hyperfine fountain clock

We can apply the idea of the simple case discussed in the previous section to the case of a fountain clock based on a hyperfine transition in Rubidium. In order to calculate the field, we consider the atoms to be a spherical cloud with magnetization

$$\vec{M} = \rho\mu_B e^{-i\omega_0 t}\hat{z} \tag{6.61}$$

where ρ is the density of atoms and μ_B is the Bohr magneton. We take the radius of the cloud to be $R = 1/k \approx 0.7$ cm, where $k = 2\pi/\lambda$ is the wavenumber of the hyperfine transition. One can show that the magnetic field at the center of a atomic cloud is

$$\vec{B} = \frac{2}{3}\rho\mu_0\mu_B(0.486)e^{-i(\omega t-0.668)}\hat{z}, \tag{6.62}$$

where μ_0 is the permeability of free space. One can also show that the Rabi frequency for this field is

$$\omega_R = \frac{2}{3}\rho\mu_0\mu_B^2(0.486)/\hbar. \tag{6.63}$$

If we take $\rho = 10^9/\text{cm}^3$, (this density is used under some circumstances[FG00] then

$$\omega_R = 3.2 \times 10^{-4}\ \text{s}^{-1}. \tag{6.64}$$

If we take an interaction time of $T = 1$ second, then the total angle through which the Bloch vector precesses is $\alpha = \omega_R T = 3.2 \times 10^{-4}$ radians. The direction of rotation depends on the phase of the field and the direction of the Bloch vector. If we take the worst-case scenario, then all the precession is in the azimuthal direction, and the apparent frequency shift is

$$\omega_{d-d} = \frac{\alpha}{T} \approx \frac{3.2 \times 10^{-4}\ \text{rad}}{1\ \text{s}} = (2\pi)(5 \times 10^{-5}\ \text{Hz}). \tag{6.65}$$

For a Rubidium clock, this corresponds to a fractional frequency shift of

$$\frac{\omega_{d-d}}{\omega} = \frac{5 \times 10^{-5}\ \text{Hz}}{6.8\ \text{GHz}} = 8 \times 10^{-15}, \tag{6.66}$$

which should be observable. (It's not actually possible for all of the precession to be in the azimuthal direction, but almost all of it can be.)

6.6 Application of model to the atomic beam

In this section we apply the model to a rough representation of the atomic beam: i.e., the expressions that we use for the density $\rho(\vec{r},t)$ and the expectation value of the dipole moment $p_0(\vec{r},t)$ are rough approximations.

6.6.1 The atomic density $\rho(\vec{r},t)$

The density is a function of position $\vec{r}$ and time t. We take the time t to be the time after the optical excitation. We take the origin of the coordinate system to be the intersection of the atomic beam axis and the axis of the excitation light. We let the x-axis point in the direction of the atomic beam and the z-axis to point up.

We write the density in terms of simpler functions:

$$\rho(\vec{r},t) = \Lambda(x,t) f(y,x) g(z,x). \tag{6.67}$$

The function $\Lambda(x)$ is the longitudinal density of the atomic beam, defined such that the number of atoms between x and $x + dx$ is equal to

$$\begin{aligned} dN &= \Lambda(x)dx \qquad (6.68) \\ &= N\lambda(x)dx, \qquad (6.69) \end{aligned}$$

where N is the total number of atoms in the pulse and $\lambda(x)$ is the longitudinal density for a pulse with only one atom. The functions $f(y,x)$ and $g(z,x)$ are the probability distributions describing the transverse dependence of the density. They are normalized such that

$$\int_{-\infty}^{\infty} f(y,x)\, dy = 1 \tag{6.70}$$

$$\int_{-\infty}^{\infty} g(z,x)\, dz = 1. \tag{6.71}$$

Given the x-coordinate of an atom, the probability P that the atom is located between

y and $y + dy$ and also between z and $z + dz$ is given by:

$$P = f(y,x)g(z,x)\,dy\,dz. \tag{6.72}$$

Transverse dependence of $\rho(\vec{r},t)$

The probability densities $f(y,x)$ and $g(z,x)$ are determined by the collimation of the atomic beam as discussed in Sec. 4.1.3. The transverse dependence is trapezoidal in the y and z directions. The upper and lower widths of the trapezoids are given by p and d in Eqs. (4.2–4.5). For simplicity, we make the crude approximation that the widths of the collimators are zero: $w_c = w_l = 0$. We rewrite Eqs. (4.2–4.3), which give p and d in the horizontal direction:

$$p_H = d_H = \mathrm{w}_s \frac{|x_c|}{l_{sc}}, \tag{6.73}$$

where x_c is the position along the x-axis with respect to the collimator. In the vertical direction Eqs. (4.4–4.5) become:

$$p_V = d_V = \mathrm{w}_s \frac{|x_l|}{l_{sl}}, \tag{6.74}$$

where x_l is the position along the x-axis with respect to the excitation light. With $w_c = w_l = 0$, the transverse dependence is rectangular, not trapezoidal. From the normalization of $f(y,x)$ and $g(z,x)$, as given in Eq. (6.70), we find that their heights are $1/p_H$ and $1/p_V$, respectively.

Longitudinal dependence of $\rho(\vec{r},t)$

The longitudinal density $\lambda(x,t)$ is determined by the velocity distribution of the atomic beam. We define $P^V(v)dv$ to be the probability that an atom in the beam has velocity between v and $v + dv$. For a thermal atomic beam, we have[Ram56]

$$P^V(v) = \frac{2v^3}{\alpha^4} e^{-\left(\frac{v}{\alpha}\right)^2}, \tag{6.75}$$

where $\alpha = \sqrt{2k_BT/m}$ is the most probable velocity for an atom in a gas. For a gas of atomic hydrogen at 80 K, $\alpha = 1150$ m/s. We find $\lambda(x,t)$ from Eq. (6.75) by setting $\lambda(x,t)dx = P^V(v)dv$ and using $x = vt$ and $dx/dv = t$. The result is:

$$\lambda(x,t) = \frac{2x^3}{\alpha^4 t^4} e^{-(x/\alpha t)^2}. \tag{6.76}$$

At time the time of excitation, $t = 0$, this blows up. The actual linear density does not blow up at $t = 0$ because of the excitation volume has finite size. This is not a problem because we are only concerned with the atomic density for times t after the atoms pass through the first oscillatory field.

6.6.2 The expectation of the dipole moment $p_0(\vec{r}, t_a)$

We take the expectation value of the dipole moment to be a function of position $\vec{r}$ and time t_a. We take the time t_a to be the time since the atom passed through the first oscillatory field. In terms of t_a, the time t since optical excitation is given as

$$t = t_a + vl_{la} = t_a + \frac{l_{la}}{L}T, \tag{6.77}$$

where v is the atomic velocity, l_{la} is the distance between the excitation light and the first oscillatory field, L is the distance between the oscillatory fields, and T is the time between the oscillatory fields. As in the previous section, we take the origin of the coordinate system to be the intersection of the atomic beam axis and the axis of the excitation light. We let the x-axis point in the direction of the atomic beam and the z-axis to point up.

Dipole induced by the oscillatory field

The first oscillatory field induces a dipole moment in each atom. The strength of the dipole moment depends on the angle α through which the first oscillatory field rotates the Bloch vector. The dipole moment is proportional to $\sin\alpha$, where $\alpha = \omega_R\tau$. Here, ω_R the Rabi frequency and τ is the time spent in the field.

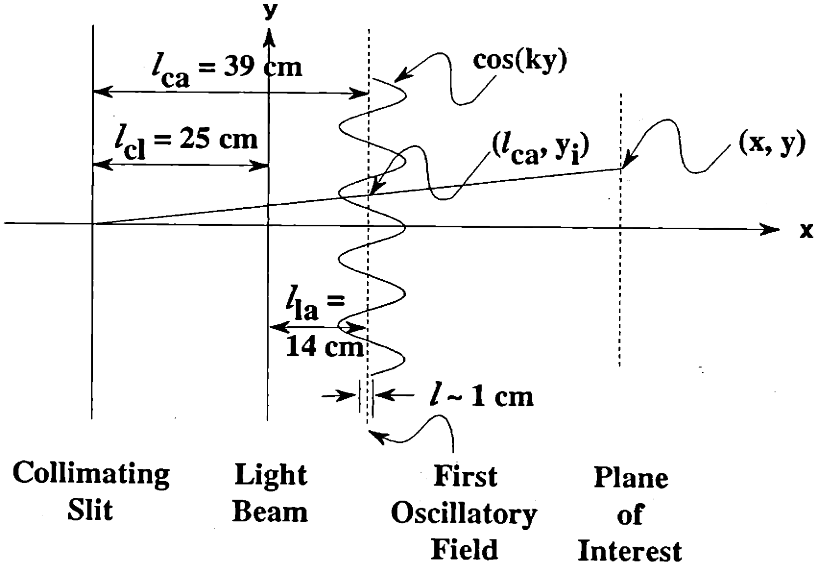

Figure 6-3: Path through oscillatory field, as viewed from above. The path starts at the collimating slit and ends at point (x,y). The path intersects the first oscillatory field at point (l_{ca}, y_i), where y_i is given in Eq. 6.78. This diagram is roughly to scale, but the vertical scale has been expanded by about a factor of one hundred relative to the horizontal.

The Rabi frequency ω_R is proportional to the amplitude of the oscillatory field. The oscillatory field is a standing wave perpendicular to the atomic beam axis, and hence the amplitude varies as $\cos(ky)$, where y is the position along the axis of the oscillatory field and $k = 2\pi/\lambda$. We take the Rabi frequency to be $\omega_R = \omega_R^0 \cos(ky_i)$, where ω_R^0 is the Rabi frequency for an atom passing exactly through an antinode of the standing wave. We ignore the amplitude variation of the oscillatory field in the vertical direction because the range of amplitudes sampled vertically is small.

In Fig. 6-3, we consider the trajectory of an atom through the first oscillatory field, as viewed from the top. As in the previous section, we make the crude approximation that the width of the collimator is zero: $w_c = 0$. Hence, the trajectory begins at the zero-width collimating slit, at point $(-l_{cl}, 0)$. We consider the trajectory which ends at point (x, y). We ignore the vertical component of the trajectory. We label the distance from the atomic beam axis at the first oscillatory field as y_i. In terms of x and y, y_i is given by

$$y_i = y\frac{l_{ca}}{x + l_{cl}}. \tag{6.78}$$

The angle α through which the Bloch vector rotates is

$$\alpha = \omega_R^0 \tau \cos\left(ky\frac{l_{ca}}{x + l_{cl}}\right). \tag{6.79}$$

Given that an atom traveled a distance $x - l_{la}$ in a time t_a, where l_{la} is the distance from the excitation light to the first oscillatory field, we find that

$$\tau = \frac{lt_a}{x - l_{la}}, \tag{6.80}$$

where l is the width of the oscillatory field. We can now write the expectation of the dipole moment as a function of position and time:

$$p_0(x, y, z, t_a) = p_0 \sin\left[\omega_R^0 \frac{lt_a}{x - l_{la}} \cos\left(ky\frac{l_{ca}}{x + l_{cl}}\right)\right], \tag{6.81}$$

where $p_0 = (1/2)ea_0n^2$ is the maximum magnitude of the rotating dipole moment.

Spontaneous and thermal decay

Once a dipole has been induced in the atoms, a significant portion of the atoms spontaneously decay or undergo a transition driven by thermal radiation. These atoms do not contribute coherently to the field rotating at the transition frequency, and we can ignore them. Hence the expectation value of the dipole moment in Eq. (6.81) decays in time as $e^{-\Gamma t}$, where Γ is the rate of incoherently driven transitions out of a given circular state, averaged over the two circular states involved in the transition.

We find Γ from the expressions in Sec. 3.10.2. Instead of averaging over the n and $n + 1$ circular states as mentioned above, we just use the average value of n in the expressions of Sec. 3.10.2. For a radiation temperature of $T = 9$ K we have

$$\Gamma = A(1 + 2\bar{n}) \approx \begin{cases} 1030\ \mathrm{s}^{-1} & : \quad n = 27.5 \\ 840\ \mathrm{s}^{-1} & : \quad n = 29.5 \end{cases}, \tag{6.82}$$

where for the $n = 27 \rightarrow 28$ transition we have used $n = 27.5$ and for the $n = 29 \rightarrow 30$ transition we have used $n = 29.5$.

Beating of the fine structure components

Another significant effect is the beating of the fine structure components. The two components, one corresponding to spin up and the other to spin down, oscillate at slightly different frequencies. The amplitude of the expectation value of the dipole moment is modulated sinusoidally at the difference frequency $\Delta\nu_{fs} \approx 2$ kHz. Precise values of $\Delta\nu_{fs}$ are given in Eq. (2.44). We take the two spin states to have equal populations. The expression for the expectation value of the dipole moment in Eq. (6.81) needs a factor of $\cos(\delta_{fs}t_a/2)$, where $\delta_{fs} = 2\pi\Delta\nu_{fs}$.

Final expression for $p_0(x, y, z, t_a)$

Including the variation in oscillatory field strength, incoherent transitions, and fine structure beating, the expectation value of the dipole moment is

$$p_0(x,y,z,t_a) = p_0 \sin\left[\omega_R^0 \frac{lt_a}{x-l_{la}} \cos\left(ky\frac{l_{ca}}{x+l_{cl}}\right)\right] e^{-\Gamma t_a} e^{-\Gamma l_{la}T/L} \cos(\delta_{fs}t_a/2). \quad (6.83)$$

We make a crude approximation to this equation, separating the position variable y from the time t:

$$p_0(x,y,z,t_a) = p_0 \sin\left(\omega_R^0 \frac{lt_a}{x-l_{la}}\right) \cos\left(ky\frac{l_{ca}}{x+l_{cl}}\right) e^{-\Gamma t_a} e^{-\Gamma l_{la}T/L} \cos(\delta_{fs}t_a/2). \quad (6.84)$$

The latter expression is not totally accurate, but using it allows the integral in Eq. (6.85) to be made time-independent, removing a level of complexity and significantly simplifying the calculation. In the next two paragraphs, we examine the justification for this approximation.

Figure 6-4 shows two density/contour plots which illustrate the difference between Eq. (6.83) and Eq. (6.84). One plot is for $\sin[\pi u\cos(\pi v)]$ and the other plot is for the simpler expression $\sin(\pi u)\cos(\pi v)$. Here $\pi u = \omega_R^0 lt_a/(x-l_{la})$ and $\pi v = kyl_{ca}/(x+l_{cl})$. We can also write $\pi u = (\pi/2)(T/T_0)$, where T is the interaction time and and T_0 is the interaction time for which $\pi u = \pi/2$, i.e., the speed for which atoms travelling down the axis of the atomic beam get a $\pi/2$-pulse. The range in u corresponds

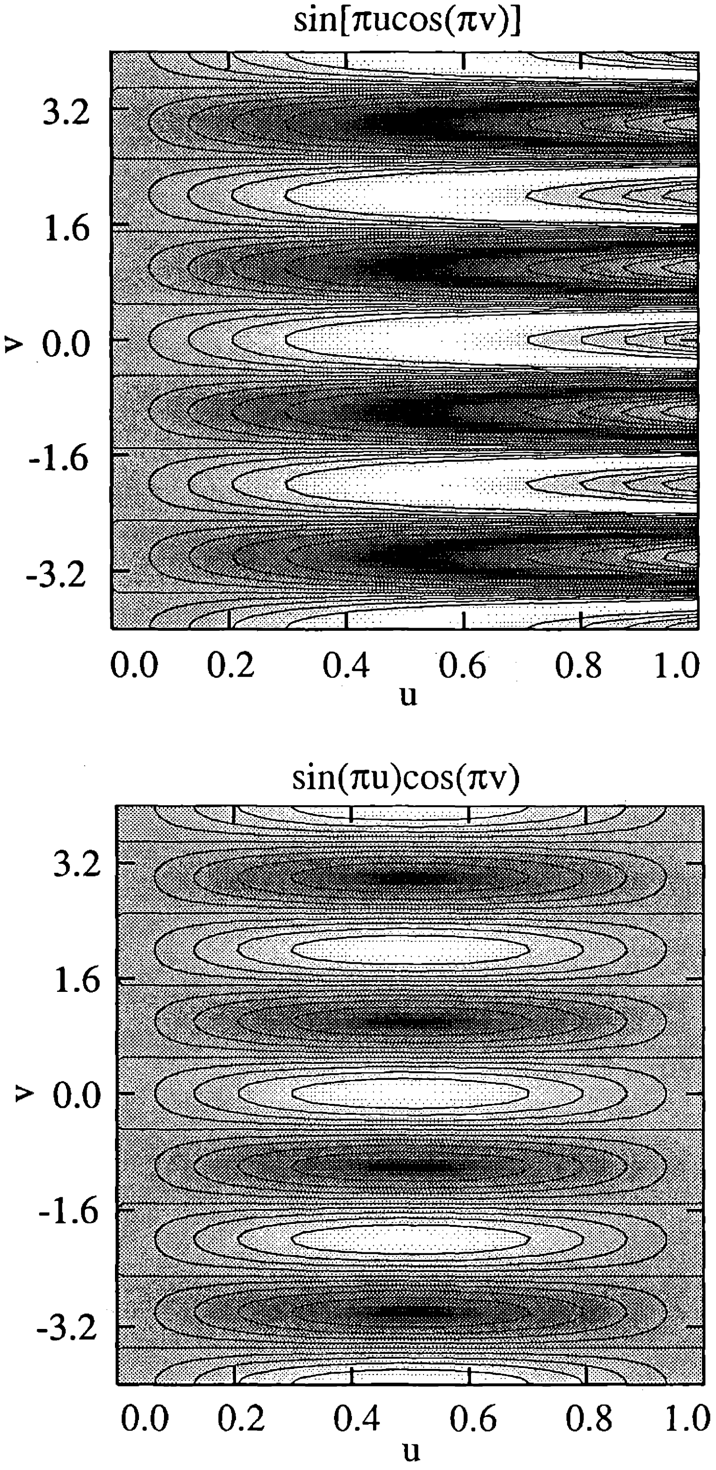

Figure 6-4: Plot of $\sin[\pi u \cos(\pi v)]$ and $\sin(\pi u)\cos(\pi v)$. The two plots share the same contour intervals and greyscale scheme. White corresponds to +1.0 and the black corresponds to -1.0. The contour interval is 0.2. These plots demonstrate that approximating the upper plot by the lower plot is quite good for $u < 0.6$ and good to about 30% for $0.6u < 0.8$. For $u > 0.8$, the dipole interactions are small and the quality of the approximation not so important.

to the range of interesting beam velocities: $u \approx 0$ corresponds to the very fastest atoms and $u \approx 1$ corresponds to the atoms which are travelling so slowly that they are getting a π–pulse. The range in v corresponds to a distance in y_i of a couple of wavelengths (a couple of millimeters), which is the approximate range of interest in the experiment. The two plots share the same contour intervals and greyscale scheme. White corresponds to +1.0 and the black corresponds to -1.0. The contour interval is 0.2.

Figure 6-4 shows that over a large range, $u < 0.6$, the approximation of Eq. (6.83) by Eq. (6.84) is quite good. Over the range $0.6 < u < 0.8$, the approximation is good to roughly 30%. For $0.8 < u < 1.0$, the approximation bears little resemblance to the actual function. However, this small range, corresponding to the slowest atoms, is unimportant: as $u \rightarrow 1$ both the atomic density and the size of the induced dipole go to zero. Hence the dipole-dipole interactions are unimportant in this range.

6.6.3 The co-rotating field along the atomic beam axis

In this section, we find an integral expression for the co-rotating field at an arbitrary point along the axis of the atomic beam (the x-axis). We then describe our procedure for numerical evaluation of the integral.

Expression for the co-rotating field

Eq. (6.8) gives the expression for the co-rotating field at an arbitrary point $\vec{r_0} = (x_0, y_0, z_0)$ and time t. We are interested in points along the x-axis with $y_0 = z_0 = 0$. Inserting the expressions for $\rho(\vec{r}, t)$ and $p_0(\vec{r}, t_a)$ from Eq. (6.67) and Eq. (6.84), respectively, we have

$$\begin{aligned} \mathcal{E}(x_0, t_a) \;=\; & \frac{\sqrt{2}}{4\pi\epsilon_0} p_0 e^{-\Gamma t_a} e^{-\Gamma l_{la} T/L} \cos(\delta_{fs} t_a/2) \\ & \int d\vec{r}\,' \left\{ \Lambda(x, t = t_a + \frac{l_{la}}{L} T) f(y, x) g(z, x) \sin(\omega_R^0 \frac{l t_a}{x - l_{la}}) \cos[k y l_{ca}/(x + l_{cl})] \right. \\ & \left. \left[\left(1 - \frac{\sin^2\theta'}{2}\right) \frac{k^2}{r'} + \left(\frac{3}{2}\sin^2\theta' - 1\right) \left(\frac{1}{r'^3} - \frac{ik}{r'^2}\right) \right] e^{ikr'} \right\}, \end{aligned} \tag{6.85}$$

where the transverse dependence of the atomic density, $f(y,x)$ and $g(z,x)$, is rectangular in y and z with widths given by Eq. (6.73) and Eq. (6.74), respectively. The integral is over $\vec{r}' = \vec{r} - \vec{r}_0$, θ' is the polar angle of $\vec{r}'$, and $r' = |\vec{r}'|$.

Approximations/simplifications to the integral

Equation (6.85) is difficult to evaluate because it requires numerical integration of a three-dimensional integral, where the integrand is oscillatory and has a singularity. Furthermore, evaluating it once gives the electric field at only one point in space and time; the evaluation must be performed at several points in space and time along a given trajectory in order to calculate the perturbation to an atom. To make the numerical integration manageable, we make three simplifications:

1. Along the longitudinal direction, we cut the integral off after 5 wavelengths ($\sim$5 mm). Beyond this, we find that the contributions to the integral wash out because the integrand oscillates as $e^{ikr'}$.

2. We ignore the longitudinal dependence of both the density $\rho(\vec{r},t)$ and the dipole magnitude $p_0(\vec{r},t_a)$ because these functions are approximately constant over the 5 wavelengths involved in the integration. Ignoring the longitudinal dependence of $\rho(\vec{r},t)$ and $p_0(\vec{r},t_a)$ makes the integrand even in the longitudinal direction, reducing the integration space by a factor of two.

3. Since we are limiting our consideration to points along the beam axis, the integrand is even along the two transverse directions, further reducing the integration space by a factor of four.

With these three changes, the expression for the co-rotating field becomes

$$\begin{aligned}\mathcal{E}(x_0,t_a) \;=\;& \frac{\sqrt{2}}{4\pi\epsilon_0} p_0 e^{-\Gamma t_a} e^{-\Gamma l_{la} T/L} \cos(\delta_{fs} t_a/2) \Lambda(x, t = t_a + \frac{l_{la}}{L} T) \sin(\omega_R^0 \frac{l t_a}{x - l_{la}}) \\ & \frac{8}{p_H p_V} \int_0^{5\lambda} dx' \int_0^{p_H/2} dy' \int_0^{p_V/2} dz' \left\{ \cos[k y' l_{ca}/(x_0 + l_{cl})] \right. \\ & \left. \left[\left(1 - \frac{\sin^2\theta'}{2}\right) \frac{k^2}{r'} + \left(\frac{3}{2}\sin^2\theta' - 1\right)\left(\frac{1}{r'^3} - \frac{ik}{r'^2}\right) \right] e^{ikr'} \right\}. \qquad (6.86)\end{aligned}$$

A result of these simplifications is that the integral in Eq. (6.86) is independent of the time t_a. This means that, for each position x_0, it only has to be evaluated once—not repeatedly for different times t_a.

We split the expression in Eq. (6.86) into two functions:

$$\mathcal{E}(x_0, t_a) = \mathcal{E}_1(x_0)\mathcal{E}_2(x_0, t_a), \tag{6.87}$$

where $\mathcal{E}_1(x_0)$ contains the integral and $\mathcal{E}_2(x_0, t_a)$ the time-dependent portion:

$$\begin{aligned} \mathcal{E}_1(x_0) &\equiv \sqrt{2}\frac{p_0}{4\pi\epsilon_0}\frac{8}{p_H p_V}\int_0^{5\lambda} dx' \int_0^{p_H/2} dy' \int_0^{p_V/2} dz' \left\{ \cos[ky' l_{ca}/(x_0 + l_{cl})] \right. \\ &\qquad \left. \left[\left(1 - \frac{\sin^2\theta'}{2}\right)\frac{k^2}{r'} + \left(\frac{3}{2}\sin^2\theta' - 1\right)\left(\frac{1}{r'^3} - \frac{ik}{r'^2}\right)\right] e^{ikr'} \right\} \qquad (6.88) \\ \mathcal{E}_2(x_0, t_a) &\equiv e^{-\Gamma t_a} e^{-\Gamma l_{la} T/L} \cos(\delta_{fs} t_a/2)\Lambda(x, t = t_a + \frac{l_{la}}{L}T)\sin(\omega_R^0 \frac{l t_a}{x - l_{la}}). \qquad (6.89) \end{aligned}$$

Note that $\mathcal{E}_2(x_0, t_a)$ is real, and hence $\mathcal{E}_1(x_0)$ contains all the phase information. The units for $\mathcal{E}_1(x_0)$ are Volts and the units for $\mathcal{E}_2(x_0)$ are m^{-1}, giving Volts/m for $\mathcal{E}(x_0, t)$. We now turn to the evaluation of $\mathcal{E}_1(x_0)$, the time-independent portion containing the integral.

Numerical Integration

As discussed in Sec. 6.2.2, we do not expect any contribution from the $1/r'^2$ and $1/r'^3$ terms near $r' = 0$. We cut off the numerical integration for the $1/r'^3$ and $1/r'^2$ terms below small value of r' (typically $r' = 1/k$). To cut off the integration, we simply set the value of the integrand equal to zero for $r' < 1/k$. We find the results of the numerical integration to be essentially the same for small changes in the cut off position.

We use Mathematica to perform the numerical integration at about 10 points along the beam axis. The points are equally spaced, and they cover the range between the two oscillatory fields. The calculation for the ten or so points takes only a few minutes on a 500 MHz G3 Apple computer. Figure 6-5 shows the mathematica results for

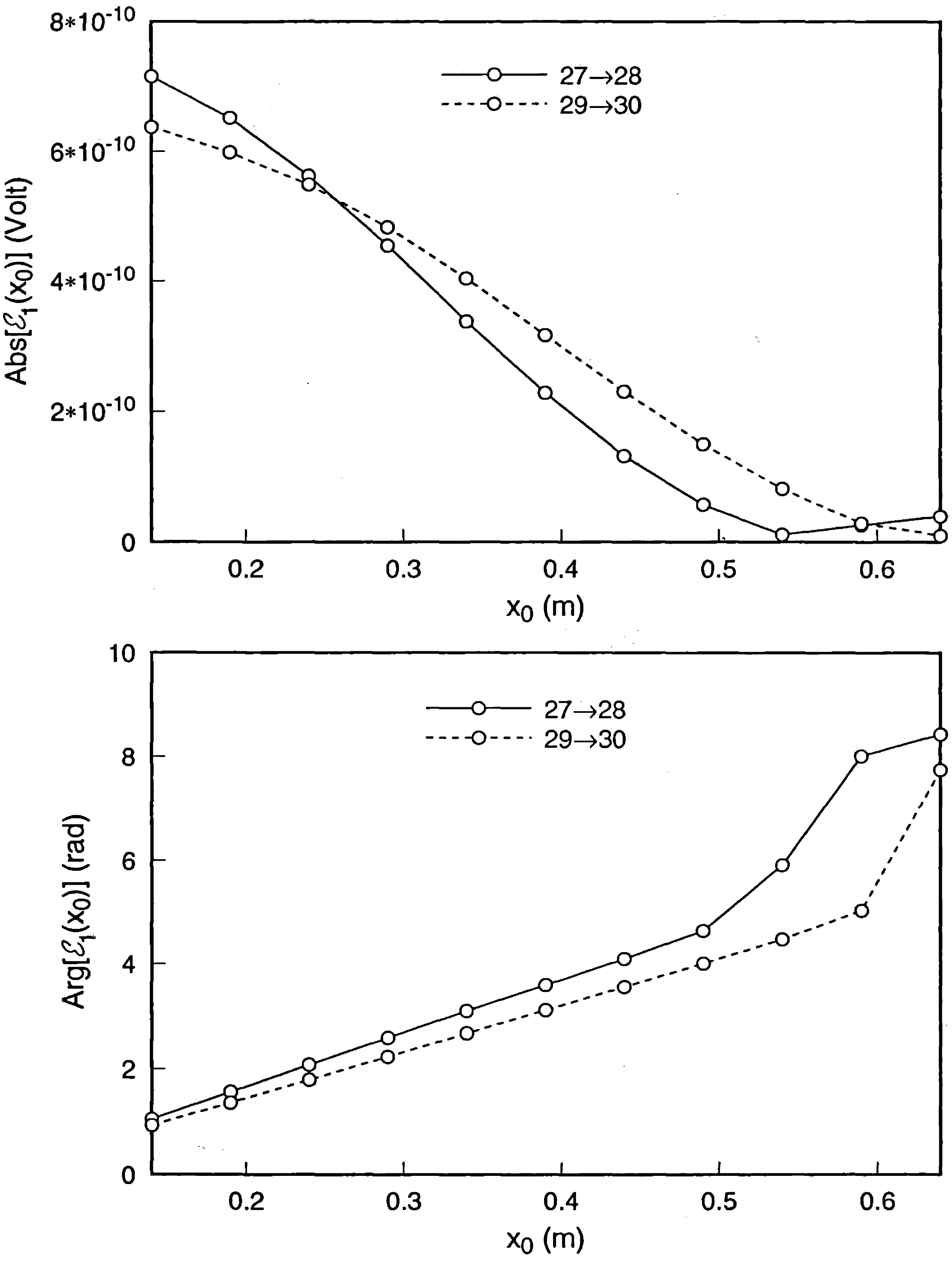

Figure 6-5: Numerical results from Mathematica for $\mathcal{E}_1(x_0)$, which is defined in Eq. (6.88). The top graph is the absolute value of $\mathcal{E}_1(x_0)$, and the bottom graph is the phase of $\mathcal{E}_1(x_0)$. In other words, if we write $\mathcal{E}_1(x = 0) = ae^{ib}$, where a and b are real, then the top graph is of a and the bottom graph is of b. Multiplying $\mathcal{E}_1(x_0)$ by $\mathcal{E}_2(x_0, t)$, as given in Eq. (6.89), yields the field amplitude $\mathcal{E}(x_0, t)$ at point x_0 and time t.

$\mathcal{E}_1(x_0)$. The top graph shows the absolute value and the bottom graph shows the phase. Results are shown for both the $n = 27 \to 28$ and the $n = 29 \to 30$ transitions. The absolute value of $\mathcal{E}_1(x_0)$ decreases with x_0 because the interatomic distances increase as the beam diverges.

Field "seen" by a given atom along the beam axis

We now consider the field "seen" by an atom travelling down the beam axis at velocity v with a corresponding interaction time of $T = L/v$, where L is the distance between the two oscillatory fields.

In the previous section we found the field as a function of x_0, the position along the beam axis, and t_a, the time after the first oscillatory field. The position is given by

$$x_0 = l_{la} + \frac{L}{T} t_a. \tag{6.90}$$

We can write the field as a function of T and t_a rather than as a function of x_0 and t_a, and we can write it in terms of the functions $\mathcal{E}_1(x_0)$ and $\mathcal{E}_2(t)$. We have

$$\mathcal{E}(T, t_a) = \mathcal{E}_1(x_0 = l_{la} + Lt_a/T)\mathcal{E}_2(x_0 = l_{la} + Lt_a/T, t_a). \tag{6.91}$$

Thus, an atom with interaction time T sees the field $\mathcal{E}(T, t_a)$ as a function of time t_a.

6.6.4 First-order solution to the Bloch vector equation of motion

In this section we examine the first-order solution to the Bloch vector equation of motion. The general first-order solution is discussed in Sec. 6.3. The form of the pseudo torque $\vec{\Omega}$ is given in Eqs. (6.9–6.11), where $\phi_\pm$ is the phase of $\mathcal{E}(T, t)$ and $\omega_{R\pm}$ is the Rabi frequency, given by the expression in Eq. (3.32), where $E_\pm = |\mathcal{E}(T, t)|$.

We now consider the solution, given in Eq. (6.18), to the zeroth-order equations of motion. The solution is static and is given by the initial conditions, i.e., the conditions right after the first oscillatory field, which rotates the Bloch vector from $(0, 0, -1)$ to

$(\sin\frac{\pi T}{2T_0}, 0, -\cos\frac{\pi T}{2T_0})$, where T_0 is the interaction time for a $\pi/2$–pulse. We have for the solution to the zeroth-order equations:

$$s_1^{(0)}(t) = \sin\frac{\pi T}{2T_0}, \quad s_2^{(0)}(t) = 0, \qquad \text{and} \quad s_3^{(0)}(t) = -\cos\frac{\pi T}{2T_0}, \tag{6.92}$$

which are independent of t.

Moving on to the the first-order equations of motion, given in Eqs. (6.19–6.21), we find the solution for $\vec{s}^{\,(1)}(t)$ for an atom with interaction time T is given by the following integrals:

$$\begin{aligned} s_1^{(1)}(t) &= -\cos\frac{\pi T}{2T_0}\int_0^t dt' \;\; \omega_{R\pm}\sin[\oplus\, \delta_{fs}t'/2 + \phi_\pm] && (6.93) \\ s_2^{(1)}(t) &= \mp\cos\frac{\pi T}{2T_0}\int_0^t dt' \;\; \omega_{R\pm}\cos[\oplus\, \delta_{fs}t'/2 + \phi_\pm] && (6.94) \\ s_3^{(1)}(t) &= +\sin\frac{\pi T}{2T_0}\int_0^t dt' \;\; \omega_{R\pm}\sin[\oplus\, \delta_{fs}t'/2 + \phi_\pm], && (6.95) \end{aligned}$$

where $\omega_{R\pm}$ and $\phi_\pm$ are considered to be functions of the dummy variable t'.

We now rewrite Eqs. (6.93–6.95) at time $t = T$. We replace $\omega_{R\pm}$ with the expression in Eq. (3.32), where $E_\pm = |\mathcal{E}(T,t)|$. We write $|\mathcal{E}(T,t)|$ in terms of both $|\mathcal{E}_1(x_0 = l_{la} + Lt_a/T)|$, shown in Fig. 6-5, and $|\mathcal{E}_2(x_0 = l_{la} + Lt_a/T, t_a)|$ given in Eq. (6.89). We have

$$\begin{aligned} s_1^{(1)}(t=T) &= -\frac{ea_0n^2}{\sqrt{2}\,\hbar}e^{-\Gamma l_{la}T/L}N\frac{2L^3}{\alpha^4T^3}e^{-[L/(\alpha T)]^2}\sin\frac{\pi T}{2T_0}\cos\frac{\pi T}{2T_0} \\ &\quad \int_0^T dt' \;\; |\mathcal{E}_1(x_0 = l_{la} + Lt'/T)|\frac{e^{-\Gamma t'}\cos(\delta_{fs}t'/2)}{t' + l_{la}T/L}\sin[\oplus\, \delta_{fs}t'/2 + \phi_\pm] && (6.96) \\ s_2^{(1)}(t=T) &= \mp\frac{ea_0n^2}{\sqrt{2}\,\hbar}e^{-\Gamma l_{la}T/L}N\frac{2L^3}{\alpha^4T^3}e^{-[L/(\alpha T)]^2}\sin\frac{\pi T}{2T_0}\cos\frac{\pi T}{2T_0} \\ &\quad \int_0^T dt' \;\; |\mathcal{E}_1(x_0 = l_{la} + Lt'/T)|\frac{e^{-\Gamma t'}\cos(\delta_{fs}t'/2)}{t' + l_{la}T/L}\cos[\oplus\, \delta_{fs}t'/2 + \phi_\pm] && (6.97) \\ s_3^{(1)}(t=T) &= +\frac{ea_0n^2}{\sqrt{2}\,\hbar}e^{-\Gamma l_{la}T/L}N\frac{2L^3}{\alpha^4T^3}e^{-[L/(\alpha T)]^2}\sin^2\frac{\pi T}{2T_0} \\ &\quad \int_0^T dt' \;\; |\mathcal{E}_1(x_0 = l_{la} + Lt'/T)|\frac{e^{-\Gamma t'}\cos(\delta_{fs}t'/2)}{t' + l_{la}T/L}\sin[\oplus\, \delta_{fs}t'/2 + \phi_\pm]. && (6.98) \end{aligned}$$

Here the variable $\phi_\pm$ refers to the phase of the field. Below we use ϕ and $\phi_\pm$ to refer to the phase of the Bloch vector.

The Bloch vector angles at time T are given by Eqs. (6.29–6.30) with $t = T$: $\Theta = \cos^{-1}[s_3(t = T)]$ and $\Phi = \tan^{-1} \frac{s_2(t=T)}{s_1(t=T)}$. The perturbation angles, θ and ϕ, are defined in Eqs. (6.31–6.32). We write θ and ϕ in terms of $\vec{s}^{(0)}(t = T)$ and $\vec{s}^{(1)}(t = T)$

$$\begin{aligned} \theta &= \cos^{-1}[s_3^{(0)}(t = T) + s_3^{(1)}(t = T)] - \cos^{-1}[s_3^{(0)}(t = T)] & (6.99) \\ \phi &= \tan^{-1} \frac{s_2^{(1)}(t = T)}{s_1^{(0)}(t = T) + s_1^{(1)}(t = T)}. & (6.100) \end{aligned}$$

6.6.5 Concrete demonstration of the model

In this section we make a concrete demonstration of the model. We choose the parameters of the model to correspond to the data shown in Fig. 6-1. Specifically, we use the parameters in Table 6.1.

Symbol	Value	Description
n	29.5	Average of $n = 29$ and $n = 30$
α	1150 m/s	most probable velocity for hydrogen gas at 80 K
Δm_ℓ	+1	Change in magnetic quantum number m_ℓ
T_0	400 μs	Interaction time T which gets a $\pi/2$-pulse
N	20000	Total number of atoms in the pulse
δ_{fs}	$(2\pi)1355$ s^{-1}	Fine structure splitting for $n = 29 \rightarrow 30$ from Eq. (2.44)
Γ	840 s^{-1}	decoherence rate from Eq. (6.82)

Table 6.1: Parameters used for a concrete demonstration of the model. These parameters correspond to the data in Fig. 6-1. As we will see, the sign choice for Δm_ℓ does not matter. The choice of $T_0 = 400$ μs is a rough guess. The choice of $N = 20000$ is a rough guess derived from the number of atoms detected per pulse and other factors described in Sec 4.1.4.

Bloch vector angles

We use Mathematica to evaluate the Bloch vector angles θ and ϕ, given in Eqs. (6.99–6.99), for the both the high and low frequency fine structure components. We use the parameter values listed in Table 6.1. Figure 6-6 shows the results of the evaluation The top left graph shows $\theta_\pm$, where the ± subscript depends on the fine structure component. The top right shows $\phi_\pm$. The other four graphs show the average and difference angles. Note that for the $\Delta m_\ell = -1$ transition, but with the same parameters as above, the only change to Figure 6-6 is the sign of the azimuthal angles ϕ_+, ϕ_-, $\bar{\phi}$, and $\delta\phi$.

Perturbation to the Ramsey resonance data

Equations (6.46–6.49) give the resonance lineshape in terms of the Bloch vector angles θ, $\delta\theta$, $\bar{\phi}$, and $\delta\phi$. Using these equations and the angles from Fig. 6-6, the results for the lineshape parameters are shown in Fig. 6-7. The bottom left shows the pseudo polarization ψ, the upper left shows the fine structure phase ϕ_{fs}, the top right shows the average phase perturbation $\bar{\phi}$ (this is the same as in Fig. 6-6), and the bottom right shows the total perturbation to the phase of the lineshape due to the interaction between the dipoles, $\phi_{fs} + \bar{\phi}$.

As specified in Table 6.1, Fig. 6-6 corresponds to a $\Delta m_\ell = +1$ transition. For a $\Delta m_\ell = -1$ transition, the azimuthal variables, ϕ and $\delta\phi$, would change sign. However, the lineshape parameters are independent of the sign of Δm_ℓ. This can be seen from Eqs. (6.46–6.49), where the ± operator in front of the azimuthal variables also depends on Δm_ℓ, thus the two sign changes negate themselves.

The bottom right graph of Fig. 6-7 is to be compared to the residuals in Fig. 6-1: the two are very close. The size and shape of the total perturbation to the phase of the lineshape, $\phi_{fs} + \bar{\phi}$, depends sensitively on the values of the parameters listed in Table 6.1. Among these parameters, N and T_0 are not accurately known. In the next section, we describe our numerical model for fitting the data, and we allow the two parameters, N and T_0, to be fit.

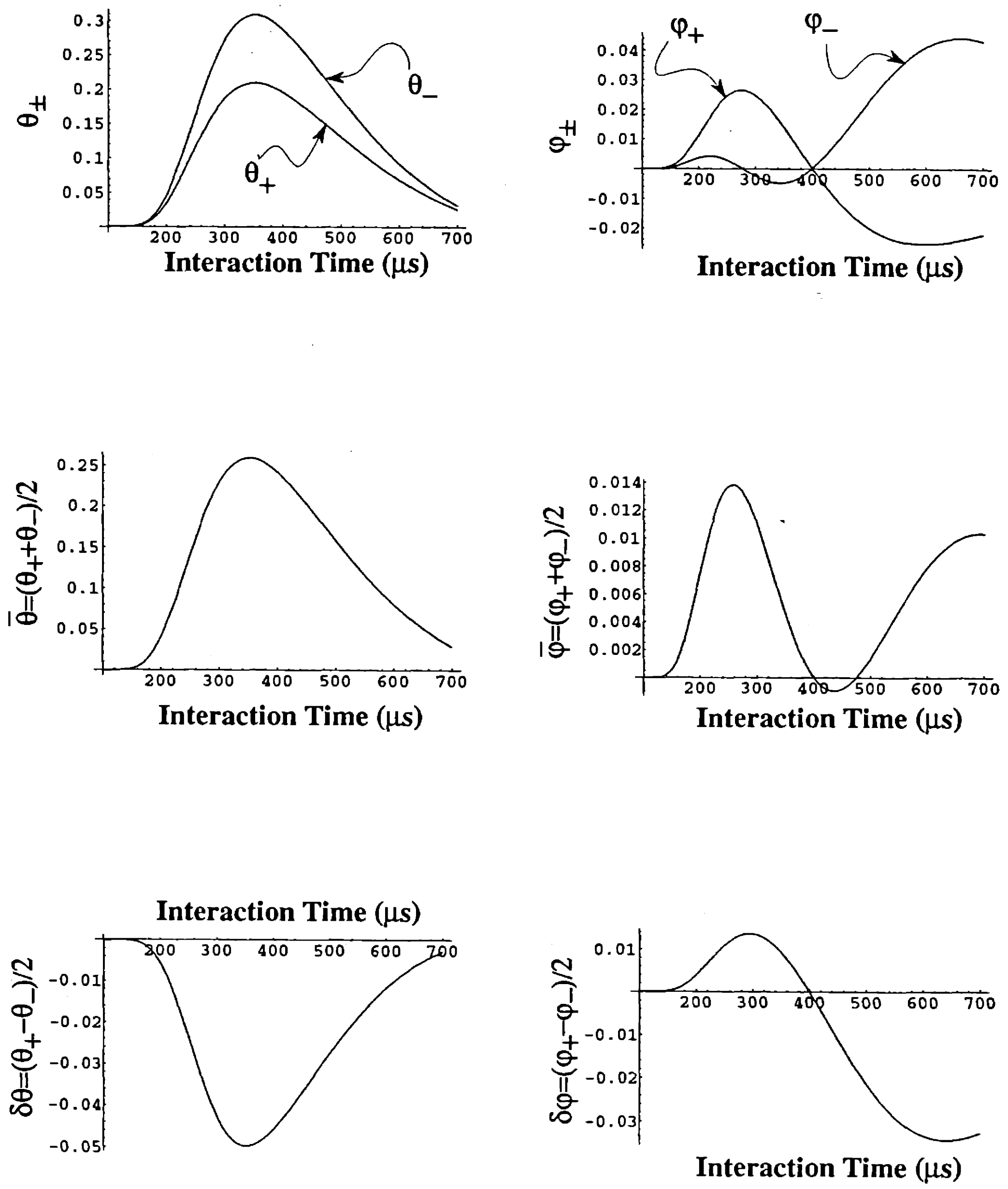

Figure 6-6: Mathematica results for the perturbation angles, θ and ϕ, as given in Eqs. (6.99–6.100), using the parameters in Table 6.1. The top left graph shows $\theta_{\pm}$, where the $\pm$ subscript depends on the fine structure component. The top right shows $\phi_{\pm}$. The other four graphs show the average and difference angles. Note that for the $\Delta m_{\ell} = -1$ transition, but with the same parameters as above, the only change to Figure 6-6 is the sign of the azimuthal angles ϕ_{+}, ϕ_{-}, $\bar{\phi}$, and $\delta\phi$.

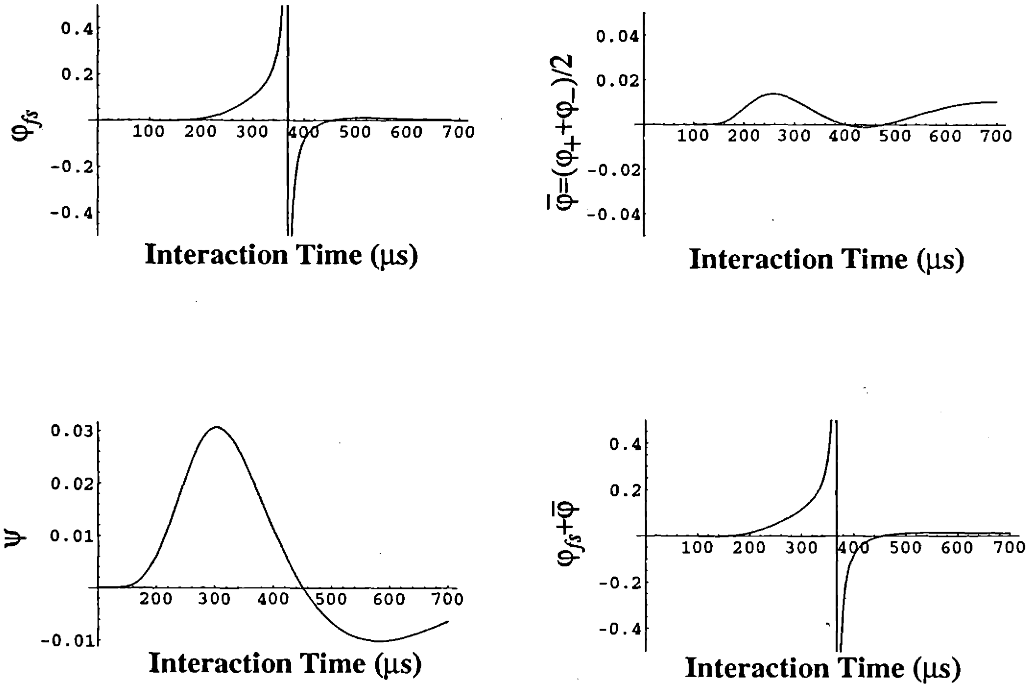

Figure 6-7: Evaluation of the lineshape parameters using the perturbation angles given in Fig. 6-6. The bottom left shows the pseudo polarization ψ, the upper left shows the fine structure phase ϕ_{fs}, the top right shows the average phase perturbation $\bar{\phi}$ (this is the same as in Fig. 6-6), and the bottom right shows the total perturbation to the phase due to the interaction between the dipoles, $\phi_{fs} + \bar{\phi}$.

6.6.6 Demonstration of fitting the model to the data

The lineshape is given by Eq. (3.81), which we reprint here:

$$I_j = \frac{\sin(\frac{T_{bin}}{2}\delta)}{(\frac{T_{bin}}{2}\delta)} A_j \cos\left(\delta T_j - \Phi_j\right) + B_j. \tag{6.101}$$

When we include the interactions between the dipoles, the phase of the lineshape, Φ_j, is slightly different from Eq. (3.82):

$$\Phi_j = \delta_0 T_j + \phi_0 - \frac{L^2\omega_0}{2c^2 T_j} - \tan^{-1}\left[\cot\left(\frac{\pi T_j}{2T_0} - \bar{\theta}\right)\tan\delta\theta\tan\left(\frac{\delta_{fs}T_j}{2} \pm \delta\phi\right)\right] \pm \bar{\phi}. \tag{6.102}$$

To get this expression for Φ_j, we have taken ψ in Eq. (3.82) to be zero: i.e., we have taken the real polarization to be zero. We then added the pseudo polarization phase,

ϕ_{fs}, given by Eqs. (6.48–6.49), and we also added the extra phase $\pm\bar{\phi}$.

The challenge of the model is to calculate the angles $\bar{\theta}$, $\delta\theta$, $\bar{\phi}$, and $\delta\phi$. They are defined in terms of $\theta_\pm$ and $\phi_\pm$ in Eqs. (6.35–6.38). These, in turn, are given by Eqs. (6.99–6.100) in terms of the "zeroth-" and "first-order Bloch vectors", $\vec{s}^{\,(0)}$ and $\vec{s}^{\,(1)}$, respectively. These in turn are given by Eq. (6.92) and Eqs.(6.96–6.98). To evaluate Eqs.(6.96–6.98) we need to use numerical integration. We use Mathematica to evaluate the numerical integrals for several different values of T, for both the n=27→28 and the n=29→30 transitions. We then program these numerical results into our fitting routine, which is written in the C programming language. Our fitting routine uses an interpolation procedure to get the value of the numerical integrals at arbitrary T. The fitting routine treats N, the number of atoms per pulse, and T_0, the interaction time for which atoms traveling along the atomic beam axis get a $\pi/2$–pulse, as fit parameters. The fitting routine uses fixed values for the other parameters in Eqs.(6.96–6.98). For the n=29→30 transition, these fixed values are given in Table 6.1.

Figure 6-8 shows the fit of our numerical model, given in Eq. (6.102), to the same data used in Fig. 6-1. This data represents the highest atomic beam densities that we achieved, and the distortion is quite pronounced. To ease comparison, the scales of Fig. 6-8 are the same as the scales of Fig. 6-1. The two data sets in Fig. 6-8 were fit simultaneously, and the reduced chi-square for the fit is $\chi_r^2 = 1.29(27)$, which is fairly consistent with one. (The number in parenthesis is the expected one σ deviation from a value of $\chi_r^2 \approx 1$. For a large number of degrees of freedom ν this deviation is given by approximately $2/\sqrt{\nu}$, as can be checked by tables for the χ_r^2 distribution.) We fix the parameter values listed in Table 6.1 except for N and T_0, which we allow to be fit. The fit results for these parameters are quite reasonable: $N = 28400(2100)$ and $T_0 = 359(11)$ μs. However, the fit values for these parameters must be taken with a grain of salt. This is because the model is approximate and the parameters are not physically well-defined.

Figure 6-9 shows the fit of our numerical model to data on the n=27 →28 transition. This data represents the highest atomic beam densities that we achieved for

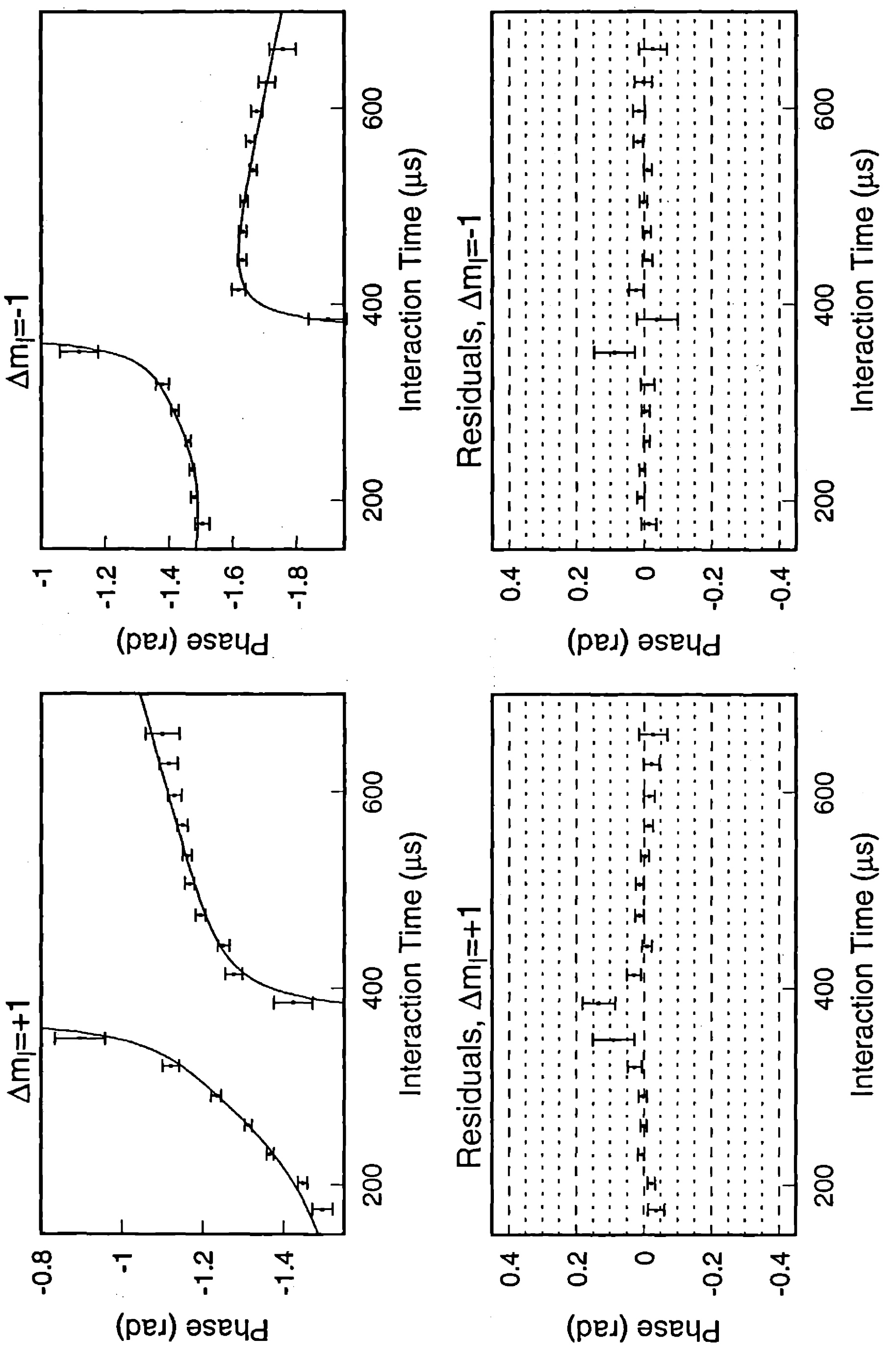

Figure 6-8: Fit of the model, given in Eq. (6.102), to example data for n=29 →30. This figure is to be compared to Fig. 6-1. The quality of the fit is good: The two data sets shown here were fit simultaneously, and the reduced chi-square for the fit is $\chi_r^2 = 1.29(27)$, which is fairly consistent with one.

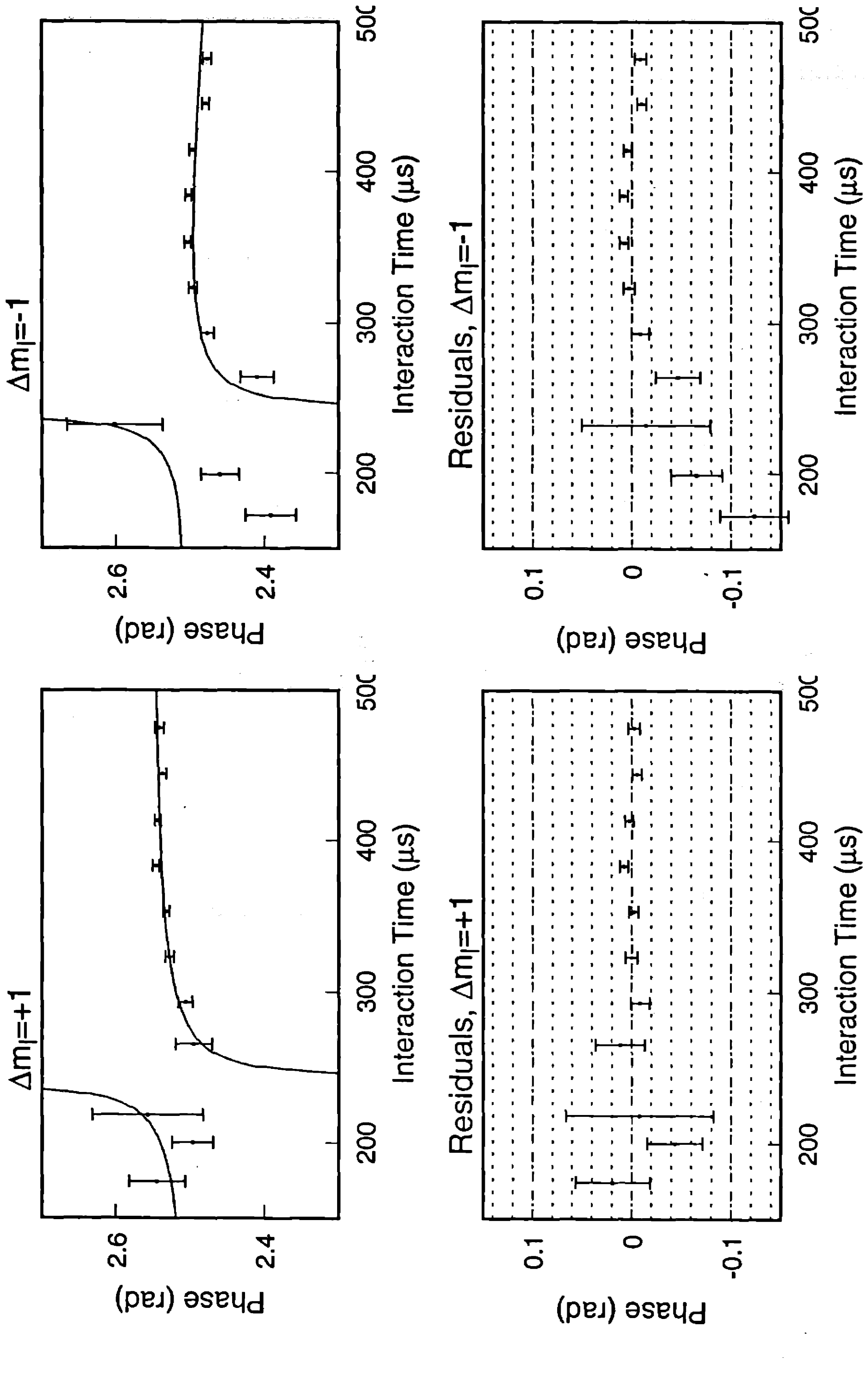

Figure 6-9: Fit of the model, given in Eq. (6.102), to example data for n=27 →28. The quality of the fit is not good: The two data sets were fit simultaneously, and the reduced chi-square for the fit is $\chi_r^2 = 3.10(35)$, which is six σ away from one.

the n=27 →28 transition, and the distortion is fairly well pronounced. The two data sets in Fig. 6-9 were fit simultaneously, and the reduced chi-square for the fit is $\chi_r^2 = 3.10(38)$, which is 5.5 σ away from one. This is only marginally better than a straight-line fit to the data which yields $\chi_r^2 = 3.94(33)$, which is 8.9 σ away from one. For some reason the model lineshape does not work well for our data on the $n = 27 \rightarrow 28$ transition.

The main difference between the n=27→28 and the n=29→30 transitions is the time T_C, given in Eq. (3.78), for which the interference between the two fine structure components of the lineshape is totally destructive (assuming no real or pseudo polarization ψ). The times T_C are 242 μs and 369 μs for the n=27 →28 and the n=29 →30 transitions, respectively. It is for times near T_C that the phase of the lineshape is the most affected by an imbalance in the weights of the two fine structure components. Because of this difference in the fine structure beating, the optimal value of T_0 is different for the two transitions.

We briefly describe the other fit parameters, of which there are four: $\delta_{0\pm}$, $\phi_{0\pm}$, where the ± subscript signifies the sign of Δm_ℓ. Recall that $\delta_{0\pm}$ is the frequency of the transition with respect to the scan center $\omega_{c\pm}$: $\delta_{0\pm} = \omega_{0\pm} - \omega_{c\pm}$. The average, $\delta_0 = (\delta_{0+} + \delta_{0-})/2$, is the magnetic field free transition frequency with respect to the average scan center $\omega_c = (\omega_{c+} + \omega_{c-})/2$. Again, these parameters must be taken with a grain of salt because the model is approximate in many ways.

6.7 Conclusion

In this chapter we developed a semi-quantitative model for the distortion to the phase of the lineshape due to the interaction between the dipoles in the atomic beam. We refer to the model as semi-quantitative because we make approximations which introduce unquantifiable error. The most problematic approximations include:

- Keeping only terms to first-order in the strength of the perturbation.

- Considering only the perturbation to atoms which travel exactly down the axis of the atomic beam.
- Use of a simplified representation of the atomic beam geometry, $\rho(\vec{r}, t)$.
- Use of a simplified representation of the expectation value of the dipole moment, $p_0(\vec{r}, t)$.

Despite these approximations, we showed that the model is successful at (semi-quantitatively) describing some of the data. It fits the n=29 →30 data well, but does not fit the n=27 →28 data. We do not know specifically why the model does not fit well to the n=27 →28 data, except that the model is approximate. We conclude that the dipole interactions are too complex to allow accurate modeling, and we can not use this model to extract cR_∞ with any confidence, especially from the data taken at higher densities.

As far as we know, this coherent dipole-dipole interaction has not been observed in any other precision resonance experiment. However, as discussed in Sec. 6.5.4, we anticipate that the effect should be observable in atomic clocks based on hyperfine transitions at fractional accuracies greater than 10^{-15} and atomic densities greater than 10^9 cm^{-3}, under certain conditions. In a fountain clock, the calculation for the distortion should be much easier because

- A first-order treatment would be well justified.
- The geometry of the atomic cloud is a simple sphere.
- The atoms all see the same pulse of radiation.
- The problem can likely be done analytically.

Chapter 7

Sources of Systematic Error

7.1 Effect of Blackbody Radiation in the Millimeter-Wave Cavities

7.1.1 Introduction

Thermal radiation drives transitions and shifts transition frequencies. The shifts are referred to as AC Stark shifts. As explained in Sec. 5.2.6 of Peter Chang's thesis[Cha92], the AC Stark shift in the resonance frequency due to blackbody radiation is negligible (<0.2 Hz at any temperature below 300 K). The AC Stark shift is small because both the lower and upper states are shifted by close the same amount. For example, in blackbody radiation at 300 Kelvin, the AC Stark shift of a circular state with $n = 30$ is about 2×10^3 Hz, but the differential AC Stark shift between circular states with $n = 29$ and $n = 30$ is only about 2×10^{-2} Hz, which is negligible. However, we easily observe the transitions driven by thermal radiation. Sec. 3.10.2 discusses how we cool the ambient radiation to an effective temperature of about 9 K in order to reduce the thermal transition rate below the spontaneous transition rate.

The thermal radiation contained in the millimeter-wave cavities does not follow a blackbody distribution. The spectral energy density of the radiation contained in the cavities is peaked at the frequencies of the cavity modes, given by Eq. (4.10). One of the fundamental transverse cavity modes is tuned to the atomic resonance under investigation. In this section we find expressions for the transition rate between the two states, Γ_t^c, and the AC Stark shift to the transition frequency, ν_{AC}, both of which are due to the thermal radiation in the resonant cavity mode. We also present data on the transitions driven by the thermal radiation in the cavities. From this data we extract the transition rate Γ_t^c. Using this rate, we make an estimate for ν_{AC}. We then find ν_{AC}^{Ramsey}, the apparent frequency shift to the Ramsey resonance data due to the "pulling" of ν_{AC}. We show that ν_{AC}^{Ramsey} is negligible.

7.1.2 Expressions for Γ_t^c and ν_{AC}

In this section we find expressions for Γ_t^c and ν_{AC}, which, as we will show, are closely related. As usual, we take x-axis to point in the direction of travel of the atomic beam, the y-axis to lie along the cavity axes, and the z-axis to point up. There is no electric field along the y-direction, and the electric field along the z-direction is irrelevant because we observe $\Delta m_\ell = \pm 1$ transitions, not $\Delta m_\ell = 0$ transitions.

For the purposes of estimation, we approximate the shape of the gaussian cavity mode as a uniform cylinder. We take the length to be d = 80.4 mm. We take the diameter to be equal to the waist of the gaussian beam given by w_0 = 3.4 and 3.8 mm for the n = 27→28 and the n = 29→30 transitions, respectively.

The AC Stark shift to the resonance frequency of a two-level system due to a distribution of radiation is [FW81]

$$\nu_{AC} = \frac{e^2 a_0^2 n^4}{16\pi\hbar^2} \int_0^\infty E_\omega^2(\omega) \left(\frac{1}{\omega_0 - \omega} + \frac{1}{\omega_0 + \omega} \right) d\omega \tag{7.1}$$

where e is the proton charge and $E_\omega^2(\omega)\, d\omega$ is the square of the electric field amplitude along the x-direction in the range ω to $\omega + d\omega$. The transition rate due to the thermal radiation is [FW81] (from Fermi's Golden Rule)

$$\Gamma_t^c = \frac{\pi e^2 a_0^2 n^4}{8\hbar^2} E_\omega^2(\omega = \omega_0) \tag{7.2}$$

In Eq. (7.1) and Eq. (7.2) we have used $x_{ab} = \frac{1}{2}a_0 n^2$ for the matrix element of x between the two circular states with quantum number n and $n+1$. Note that Eq. (7.1) incorporates the equal and opposite AC Stark shifts of the upper and lower states.

Next, we estimate $E_\omega^2(\omega)$ at an antinode of the cavity. In thermal equilibrium at a temperature T, the energy in the resonant cavity mode is kT (assuming that $kT \gg \hbar\omega_0$). The energy density is given by

$$u = kT/V, \tag{7.3}$$

where V is the volume of the cylindrical cavity. This result is a spatial average—along the cavity axis, the actual energy density varies sinusoidally as $\cos^2(ky)$. Integrating u over the volume of the cavity yields the total energy kT. The spectral energy density has a Lorentzian distribution:

$$u_\omega(\omega) = \frac{2u}{\pi\gamma}\frac{(\gamma/2)^2}{(\omega-\omega_c)^2+(\gamma/2)^2}, \tag{7.4}$$

where ω_c is the center frequency of the cavity mode and γ is the FWHM of the Lorentzian. From measurements of the reflected power as a function of frequency we find γ to be about $\gamma = 2\pi \cdot 5$ MHz. We have normalized $u_\omega(\omega)$ such that integrating $u_\omega(\omega)$ over ω yields $u = kT/V$. From electrodynamics, the energy density due to a standing plane-wave is $\epsilon_0 E^2 = \epsilon_0 E_0^2 \cos^2(\vec{k}\cdot\vec{r})\cos^2(\omega t + \phi)$, where E is the magnitude of the electric field and E_0 is the amplitude of the oscillating electric field. The spatial- and time-averaged energy density is $u = \frac{\epsilon_0}{4}E_0^2$, where the factor of four comes from averaging the sinusoidal terms: $\langle\cos^2(\omega t)\cos^2(\vec{k}\cdot\vec{r})\rangle = \frac{1}{4}$. It follows that the spectral energy density is

$$u_\omega(\omega) = \frac{\epsilon_0}{4}E_\omega^2(\omega). \tag{7.5}$$

Combining Eqs (7.3–7.5), we find

$$E_\omega^2(\omega) = \frac{8kT}{\pi\epsilon_0 V\gamma}\frac{(\gamma/2)^2}{(\omega-\omega_c)^2+(\gamma/2)^2}. \tag{7.6}$$

Using this result for $E_\omega^2(\omega)$ and Eq. (7.1), we find the AC Stark shift to be

$$\nu_{AC} = \frac{e^2 a_0^2 n^4}{16\pi\hbar^2}\frac{8kT}{\pi\epsilon_0 V\gamma}\int_0^\infty \frac{(\gamma/2)^2}{(\omega-\omega_c)^2+(\gamma/2)^2}\left(\frac{1}{\omega_0-\omega}+\frac{1}{\omega_0+\omega}\right)d\omega. \tag{7.7}$$

We take the rotating-wave approximation by dropping the anti-resonant term (the term with $\omega_0+\omega$ in the denominator). Letting $u=(\omega-\omega_c)/(\gamma/2)$ and $u_0=(\omega_0-\omega_c)/(\gamma/2)$, the integral has the form

$$I=\int_{-\infty}^{\infty}\frac{1}{1+u^2}\frac{1}{u_0-u}\,du=\pi\frac{u_0}{u_0^2+1}, \tag{7.8}$$

where we have taken the principal part of the integral and have approximated the lower bound of the integral as negative infinity. The lower bound is actually $-2\omega_c/\gamma$, the absolute value of which is much greater than one. Note that u_0 is the fractional mistuning of the cavity from the resonance, in terms of half the cavity linewidth. The AC Stark shift is then

$$\nu_{AC}=\frac{e^2a_0^2n^4kT}{2\pi\epsilon_0\hbar^2V\gamma}\frac{u_0}{u_0^2+1}. \tag{7.9}$$

Using the above result for $E_\omega^2(\omega)$ and Eq. (7.2), we find the thermal transition rate when the cavity is tuned on resonance ($\omega_c=\omega_0$)

$$\Gamma_t^c=\frac{e^2a_0^2n^4kT}{\epsilon_0\hbar^2V\gamma}. \tag{7.10}$$

Inspecting Eqs. (7.9–7.10), there is a close relationship between ν_{AC} and Γ_t^c. Combining these equations, we find that the AC Stark shift is given by

$$\nu_{AC}=\frac{\Gamma_t^c}{2\pi}\frac{u_0}{u_0^2+1}, \tag{7.11}$$

which depends only Γ_t^c and the fractional mistuning of the cavity, u_0.

The temperature T in Eqs. (7.9–7.10) is not well defined. This is because the radiation is not in thermal equilibrium. The radiation is coupled to the 4 K cavity mirrors and, via the input coupler, to the 300 K room temperature environment. The effective radiation temperature T_e is determined by the temperature, the emissivity, and the transmission of

- the ~80 K Teflon window on the liquid nitrogen cooled cryogenic shield
- the ~4 K fused silica optic used for the input coupler of the cavity.
- the ~4 K solid copper end mirror of the cavity.

We do not attempt to calculate T_e because of our lack of knowledge of most of these parameters. In the next section we present and analyze some data from which we extract Γ_t^c, and in turn T_e, for the purpose of estimating ν_{AC}.

7.1.3 Presentation and analysis of the data which shows the effect of the cavities

In this section we present data taken under special circumstances in order to make transparent the effect of the thermal radiation in the resonant cavity mode on the inversion of the atom. We analyze this data and extract the thermally-driven transition rate Γ_t^c and then solve for the value of the effective cavity radiation temperature T_e.

Figure 7-1 shows the data from which we extract the transition rate Γ_t^c due to the thermal radiation in the cavities. Figure 7-1 also shows the fits to a function of the form $y = mx + b$, where the slope m is fit and the "y-intercept" b is fixed at -1. The meaning of these fits is discussed below. The data was taken on the $n = 27 \rightarrow 28$ transition. The method for taking this data is straightforward: We turn off the millimeter-wave radiation. We prepare the atoms in the $n = 27$ circular state. We pick a cavity and measure the inversion of the atoms with this cavity tuned and then mistuned. The difference in the atomic inversion is due to the thermal radiation in the resonant cavity mode. We repeat this process for the other cavity.

For a simple understanding of this data, we consider the thermally-driven and spontaneous transitions as a small perturbation and keep only terms up to first order in time t. Also, we take the spontaneous decay rate and thermally-driven rates to be independent of the principal quantum number n. This is a good approximation in

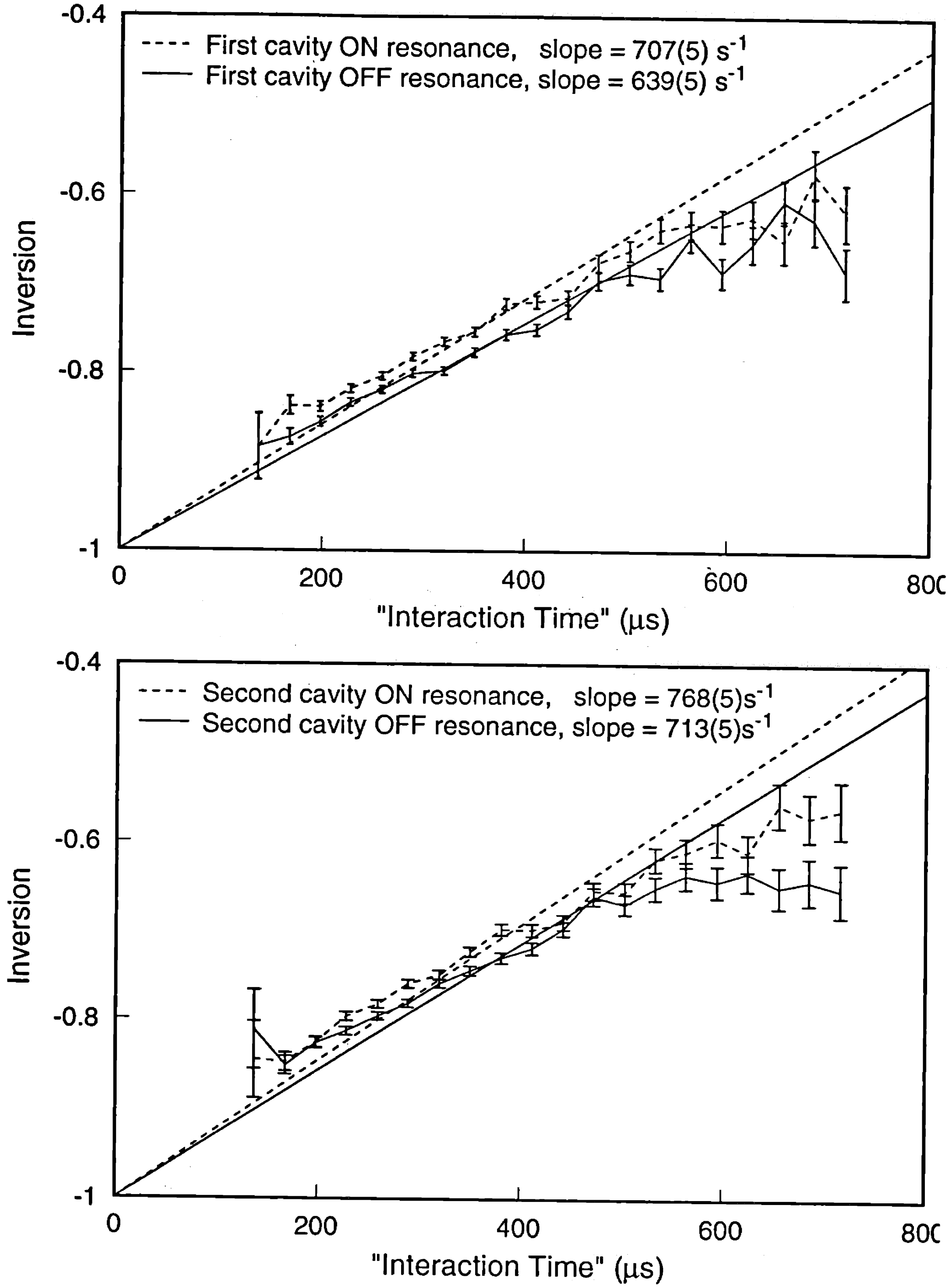

Figure 7-1: Effect of the radiation in both the first and second cavities on the final state inversion. When a cavity is tuned on resonance, the thermal radiation tends to drive the atoms from the lower state to the upper state, which means the inversion goes up. This effect increases with the amount of time spent in the cavity: The change to the inversion is more pronounced for the slower atoms (the atoms with longer interaction time T). As described in the text, the straight lines are a fit of a first-order model to the data. The fit results for the slope are quoted in the figure.

the limit of high n, where n is the principal quantum number. We take all N atoms to be prepared in the lower state: $N_2(t=0) = 0$ and $N_1(t=0) = N$. We label the spontaneous decay rate as Γ_s, and we label the thermally-driven rate as Γ_t. The atoms spend a time $t_c = w_0/v = (w_0/l_{ld})t_{ld}$ in the cavity, where v is the atomic velocity, w_0 is the waist of the cavity mode, l_{ld} is the distance from production to detection, and t_{ld} is the time from production to detection. We label the thermally-driven rate between the upper and lower states while the atoms are are in the cavity as Γ_t^c. We ignore the spontaneous decay induced by the cavity mode—it is a relatively small effect when $\bar{n} = kT/(\hbar\omega_0) \gg 1$. To first order, the population in the upper and lower states just before detection at time $t = t_{ld}$ is easily shown to be

$$\begin{aligned} N_2(t=t_{ld}) &= N\left(\Gamma_t + \frac{w_0}{l_{ld}}\Gamma_t^c\right)t_{ld} && (7.12) \\ N_1(t=t_{ld}) &= N + N\left(-2\Gamma_t - \Gamma_s - \frac{w_0}{l_{ld}}\Gamma_t^c\right)t_{ld}. && (7.13) \end{aligned}$$

These expressions, being only good to first order, neglect the return of atoms that have been transferred out of a state. The inversion, $\mathcal{I} = (N_2 - N_1)/(N_2 + N_1)$, is given to first order by

$$\mathcal{I}(t=t_{ld}) = -1 + 2\left(\frac{w_0}{l_{ld}}\Gamma_t^c + \Gamma_t\right)t_{ld}. \tag{7.14}$$

If the cavity is tuned far from resonance, then the expression for the inversion reduces to

$$\mathcal{I}(t=t_{ld}) = -1 + 2\Gamma_t t_{ld}. \tag{7.15}$$

The quality of the fits in Fig. 7-1 is not good. If we include a second-order term, then the fit is good. For simplicity, we neglect second-order effects. From Eqs. (7.14) and (7.15), it can be seen that the difference in inversion between the tuned and untuned cavity is

$$),\Delta\mathcal{I} = 2\frac{\omega_0}{l_{ld}}\Gamma_t^c t_{ld} \equiv \Delta\Gamma \cdot t_{ld}, \tag{7.16}$$

where $\Delta\Gamma$ is the difference in slope between tuned and untuned cavity. From the fit parameters shown in Fig. 7-1, we find that the difference in the slope $\Delta\Gamma$ is, for the first cavity, $\Delta\Gamma = 42(4)\ \mathrm{s}^{-1}$, and is, for the second cavity, $\Delta\Gamma = 34(4)\ \mathrm{s}^{-1}$. The average for the two cavities is $\Delta\Gamma = 38(3)\ \mathrm{s}^{-1}$. The uncertainty quoted is a statistical uncertainty only. The total uncertainty is probably about 30% because we dropped the second-order terms. Solving Eq. (7.16) for Γ_t^c we find

$$\Gamma_t^c = \frac{l_{ld}}{2w_0}\Delta\Gamma = 4.7 \times 10^3\ \mathrm{s}^{-1}, \tag{7.17}$$

where we have used $l_{ld} = 0.834$ m, $w_0 = 3.4$ mm, and $\Delta\Gamma = 62\ \mathrm{s}^{-1}$. Combining Eq. (7.10) and Eq. (7.17), we derive an estimate for T:

$$T = \Delta\Gamma \frac{l_{cd}}{2w_0} \frac{\epsilon_0 \hbar^2 V \gamma}{e^2 a_0^2 n^4 k} = 18\ \mathrm{K}. \tag{7.18}$$

We expect that Eqs. (7.17–7.18) are accurate to about 30% or so, with most of the inaccuracy coming from the fact that we dropped the second-order terms.

7.1.4 AC Stark shift

We now find an expression for the AC Stark shift by combining Eq. (7.11) and Eq. (7.17):

$$\nu_{AC} = \frac{l_{ld}\Delta\Gamma}{4\pi w_0} \frac{u_0}{u_0^2 + 1}. \tag{7.19}$$

As described in Sec. 4.3.2, we tune the cavities to a fractional accuracy of about 5%. Hence we use $\langle u_0 \rangle = 0$ with an uncertainty of $\Delta u_0 = 0.1$. This translates into an uncertainty for ν_{AC} of

$$\Delta\nu_{AC} = \frac{l_{ld}\Delta\Gamma}{4\pi w_0}\Delta u_0. \tag{7.20}$$

Using Eqs. (7.19–7.20), our best estimate of ν_{AC} in the cavities is

$$\nu_{AC} = 0(70)\ \mathrm{Hz}. \tag{7.21}$$

This shift "pulls" the Ramsey resonance lineshape, leading to an apparent frequency shift reduced by the ratio of the cavity diameter to the inter-cavity separation.

From Eq. (3.66), the shift to the fitted frequency is

$$\nu_{AC}^{Ramsey} = 2\frac{w_0}{L}\overline{\nu_{AC}}, \tag{7.22}$$

where $\overline{\nu_{AC}}$ is the average of ν_{AC} for the two cavities, given by $\overline{\nu_{AC}} = 0(50)$ Hz. Our best estimate for the shift to the Ramsey resonance data is

$$\nu_{AC}^{Ramsey} = 0.0(7) \text{ Hz}, \tag{7.23}$$

which represents a fractional uncertainty in the resonance frequency of about 2×10^{-12}, which is unimportant.

7.2 Collisions with residual gas

This brief section is based on Peter Chang's thesis[Cha92]. Collisions of the Rydberg states with the residual gas result in a frequency shift which is proportional to the pressure. The main gas load in the interaction region is from the hydrogen beam. To estimate this shift, we use a measurement of the pressure shift due to H_2 on Rb Rydberg atoms, which is 150 MHz/torr[TKSW89]. We estimate the gas density in the interaction region, expressed in equivalent room-temperature pressure, to be $p \approx 3 \times 10^{-12}$ torr. The pressure shift is $E_p = 4 \times 10^{-4}$ Hz for an $n \approx 30$ level, and the relative shift between the n level and the $n+1$ level is much smaller. This pressure shift is negligible.

7.3 Spin polarization

As discussed in Sec. 3.10.1, if the electron spins have some non-zero polarization ψ along the quantization axis of the circular states then the two fine structure components will not have equal weights. Here, $\psi = P_+ - P_-$ where P_+ and P_- are the probabilities for the two spin states. Spin polarization perpendicular to the quantization axis does not affect the weighting. We do not entirely resolve the two fine structure components, and an imbalance between them can lead to a systematic error.

In early versions of the experiment, the electron spins were slightly polarized ($\psi \approx 0.1$) along the quantization axis. We deduced that the only mechanism for producing spin polarization was elliptical polarization of the excitation light. However, this mechanism would create spin polarization along the axis of propagation of the excitation light—not along the quantization axis. We then realized that the (essentially random) residual magnetic fields had the effect of unpredictably rotating the spin polarization. The interaction of the spins with the residual magnetic fields was about as strong as the spin-orbit interaction, further complicating the dynamics. Thus, some of the spin polarization created along the axis of the excitation light was rotated to be along the quantization axis. Although our lineshape model can account for a constant spin polarization, but the spin polarization was not constant due to the time-dependent rotations caused by the residual magnetic fields.

In the current generation of the experiment we reduced this problem to a negligible level by using linearly polarized excitation light and by applying a small (150 mG) magnetic field to stabilize the dynamics of the spin polarization. We measure the power in the unwanted linear polarization component to be a factor of 2000 smaller than the power in the desired linear component. This means the spin polarization we impart to the electrons is less than $\psi = 5 \times 10^{-4}$. The uniform magnetic field that we apply is roughly parallel to the quantization axis. This magnetic field has a strength of about 150 mG and overwhelms the residual magnetic fields and the spin-orbit interaction. Any spin polarization we create adiabatically follows the direction of the magnetic field. Thus, any small amount of spin polarization caused by the low level of elliptical polarization of the excitation light stays roughly perpendicular to the quantization axis, reducing the spin polarization ψ along the quantization axis. The angle between the magnetic field and the quantization axis is less than 0.1 radians, so that $\psi < 5 \times 10^{-5}$. This level of spin polarization is negligible; the fine structure splitting is ≈ 2 kHz, and a spin polarization of $\psi = 5 \times 10^{-5}$ leads to a bias of only about 0.1 Hz.

7.4 Absolute frequency and spectral purity of the millimeter-wave radiation

The millimeter-wave radiation we use to do spectroscopy has a frequency on the order of 300 GHz. Its frequency is referenced to the 10 MHz output of a cesium clock (Hewlett-Packard, model 5061A) by a frequency multiplication chain. We regularly check the long term frequency accuracy of the cesium clock by comparing it to atomic clocks maintained by the U.S. Naval Observatory. We do this comparison with a Loran receiver (Stanford Research Systems, model number FS700), and the fractional accuracy of our cesium clock is typically better than 1×10^{-12} over several hours.

The short term accuracy of the millimeter-wave frequency is dominated by phase noise on the millimeter-wave radiation due to the cesium clock and/or the frequency chain picking up noise from the 120 VAC electrical power. This phase noise is at multiples of 60 Hz away from the carrier and is not random—its phase is related to the phase of the 60 Hz, 120 VAC electrical power. In our experiment, we make many short time-scale measurements: about 10^6 measurements a night, each of which lasts about 1 ms. The effect of random phase noise tends to average out over many short time-scale measurements. The systematic phase noise may or may not average out in this manner, depending on the exact timing of the measurements relative to the timing of the noise.

To eliminate our sensitivity to this systematic phase noise, we set the repetition rate of the lasers to be 61.00 Hz and accumulate data for 61 shots before changing parameters. The effectiveness of this approach can be seen by taking the Fourier transform of noise at 60 Hz which lasts for one second. The noise power spectrum is maximized at 60 Hz and is zero at 61 Hz. Consequently, we always take data for one second at each point with the lasers operating at 61.00 Hz.

Chapter 8

Data Analysis: extraction of cR_∞ from the Ramsey resonance data

This chapter is the culmination of this thesis. In it, we describe the data analysis that we perform in order to extract cR_∞ from our Ramsey resonance data.

8.1 Overview

8.1.1 Final data

As in all such precision measurements, the final data was acquired after a long period of data taking to search for, diagnose, and hopefully eliminate systematic errors. Thus the final data represents only a small fraction of all the data acquired. The final data, described in Table 8.1, comes from four separate days and involves both the $n = 27 \rightarrow 28$ and $n = 29 \rightarrow 30$ transitions. Table 8.1 itemizes each data set of the final data. It gives the date that the data was acquired, the circular state transition used, the bias voltage for the electric field, and the the average counting rate R, which is the average number of atoms detected per second.

The instantaneous counting rate fluctuates significantly from shot to shot, due mainly to fluctuations in the power of the optical excitation light, but the average rate R is relatively stable over the time to acquire a given data set in Table 8.1. The

Index	Acquisition Date	Transition	Bias Voltage	Counting Rate R
1	April 12	27→28	+0.19993(1) V	1.10×10^4 s^{-1}
2	April 12†	27→28	−0.19993(1) V	1.10×10^4 s^{-1}
3	May 8 *	27→28	+0.19995(1) V	0.51×10^4 s^{-1}
4	May 16	27→28	+0.50005(1) V	1.15×10^4 s^{-1}
5	May 16	27→28	−0.50006(1) V	1.22×10^4 s^{-1}
6	May 16*	27→28	+0.50000(1) V	0.81×10^4 s^{-1}
7	May 16*	27→28	−0.50001(1) V	0.75×10^4 s^{-1}
8	May 21‡	29→30	+0.40009(1) V	2.25×10^4 s^{-1}
9	May 21	29→30	−0.40009(1) V	2.20×10^4 s^{-1}
10	May 21*	29→30	+0.39991(1) V	0.69×10^4 s^{-1}
11	May 21*	29→30	−0.39991(1) V	0.67×10^4 s^{-1}

Table 8.1: Summary of final Ramsey resonance data on circular transitions. Each row describes a data set, and each data set includes both $\Delta m_\ell = +1$ and $\Delta m_\ell = -1$ data. We index the data sets for later reference. The asterisks mark the data taken at low densities. The † and ‡ symbols mark the data shown in Figs. 6-8 and 6-9, respectively.

average counting rate $\bar{R}$ for a given data set is the total number of atoms counted divided by the time duration of the data set.

The maximum counting rate we can achieve is in the range 0.5-2.5 $\times 10^4$ s^{-1} and varies from day to day and also within a single day due to variations in the efficiency of the atomic source and optical excitation. In acquiring this data, we exercised some control over the counting rate R. On May 16, we allowed the counting rate to drift down on its own by about 40%. On May 21, we changed the counting rate by attenuating the laser used for Rydberg state excitation. We divide the data in Table 8.1 into two rough categories: high and low counting rate R. The low counting rate data is marked with an asterisk.

8.1.2 Data analysis

Our procedure for analyzing the data is as follows: First, we extract a value of cR_∞ for each data set listed in Table 8.1. For this purpose, we use the relatively simple lineshape model summarized in section 3.12. This lineshape model does not include the the distortion to the lineshape phase due to the dipole interactions. In order to estimate the error in this result introduced by ignoring the dipole interactions, we use the fact that the dipole interactions are density-dependent. We compare the results for cR_∞ as a function of counting rate R, which is proportional to the density, and we form an estimate for the error introduced by ignoring the dipole interactions.

8.2 Extracting cR_∞ from a single data set

We extract cR_∞ for each data set in Table 8.1 using the procedure described in Section 3.12. First, we fit the sinusoidal lineshape to each time bin of the data for the $\Delta m_\ell = +1$ transition. We then repeat this for the data on the $\Delta m_\ell = -1$ transition. These fits yield the phase of the sinusoidal lineshape, Φ_j, for each time bin centered at interaction time T_j, where j denotes the time bin. We then fit our model for the phase of the lineshape, Eq. (3.82), to the results for Φ_j as a function of T_j. This fit gives the frequency of the transition. Note that the spin-orbit effect symmetrically splits each transition into a fine structure doublet, and the fit gives the centroid frequency of the fine structure doublet. [The splitting of the doublet, $\Delta\nu_{fs\mu}$, is given by Eq. (2.48).]

Then, as described in Sec. 5.1, we eliminate the Zeeman effect to first-order in $B_\parallel$ by averaging the transition frequencies of the $\Delta m_\ell = +1$ and $\Delta m_\ell = -1$ transitions.

As described in Sec. 5.2, we correct for the second-order Stark effect using measurements of the first-order Stark effect on near-circular state transitions.

Finally, we correct for the fine structure contribution due to the relativistic mass variation $\nu_{fs\mu}$, given in Eq. (2.35). The result is the non-relativistic, field-free transition frequency $\nu_{nr\mu}$ for hydrogen.

As discussed in Chapter 2, QED effects are negligible, except for the anomalous magnetic moment of the electron which is included in the splitting $\Delta\nu_{fs\mu}$ given in Eq. (2.48). Hyperfine structure is also negligible.

Using the Balmer formula with the finite-mass correction, given in Eq. (2.4), it is a simple matter to extract cR_∞.

8.3 Example analysis of a single data set

In this section we describe the extraction of cR_∞ from the data set listed in Table 8.1 that was acquired on May 8, 2000. The analysis in this section neglects the dipole interactions. The uncertainty arising from this effect is discussed later in this chapter. Although the data set considered in this section has a relatively low counting rate, $R = 5.1 \times 10^4\ \mathrm{s}^{-1}$, the statistical uncertainties in this data set are small because most of the day was spent acquiring data for this one data set.

8.3.1 Sinusoidal lineshape fit

We start with the first stage of the fitting process: the fit of each time bin j of resonance data to the sinusoidal lineshape.

The form of the experimental lineshape for each time bin is given by Eq. (3.1), and the associated statistical uncertainty is given by Eq. (3.73). The lineshape model and fitting procedure are summarized in Sec. 3.12.

Figure 8-1 shows the fit for each time bin of raw data to the sinusoidal lineshape model given in Eqs. (3.81) and (3.83). The data on the left of Figure 8-1 is for the $\Delta m_\ell = +1$ transition, and the data on the right is for the $\Delta m_\ell = -1$ transition. We use 15 separate time bins for the data in Fig. 8-1. Each time bin in Fig. 8-1 is labeled with its start time. The time bins are $\mathcal{T}_{bin} = 50\ \mu\mathrm{s}$ wide, and the range of arrival times $\mathcal{T}$ covered by all the time bins is 250 μs to 1000 μs. Recall that the arrival time is the time from production of the Rydberg state to detection. Each frequency scan in Fig. 8-1 has 60 points, separated by 250 Hz, which gives a scan range of 15 kHz. The data set of the $\Delta m_\ell = +1$ transition is similar to that of the $\Delta m_\ell = -1$. The main difference between the $\Delta m_\ell = +1$ and $\Delta m_\ell = -1$ data is the center frequency, which differs by $\approx$ 414 kHz because of the first-order Zeeman effect in the 150 mG applied magnetic field. The center frequency ($\nu_C = \omega_C/2\pi$) of the $\Delta m_\ell = +1$ scan (left) is $\nu_C = 316\,415\,664\,177.4$ Hz. The center frequency of the $\Delta m_\ell = -1$ scan (right) in Fig. 8-1 is $\nu_C = 316\,415\,249\,927.4$ Hz.

Three factors affect the amplitude of the sinusoids in Fig. 8-1. First, the fastest

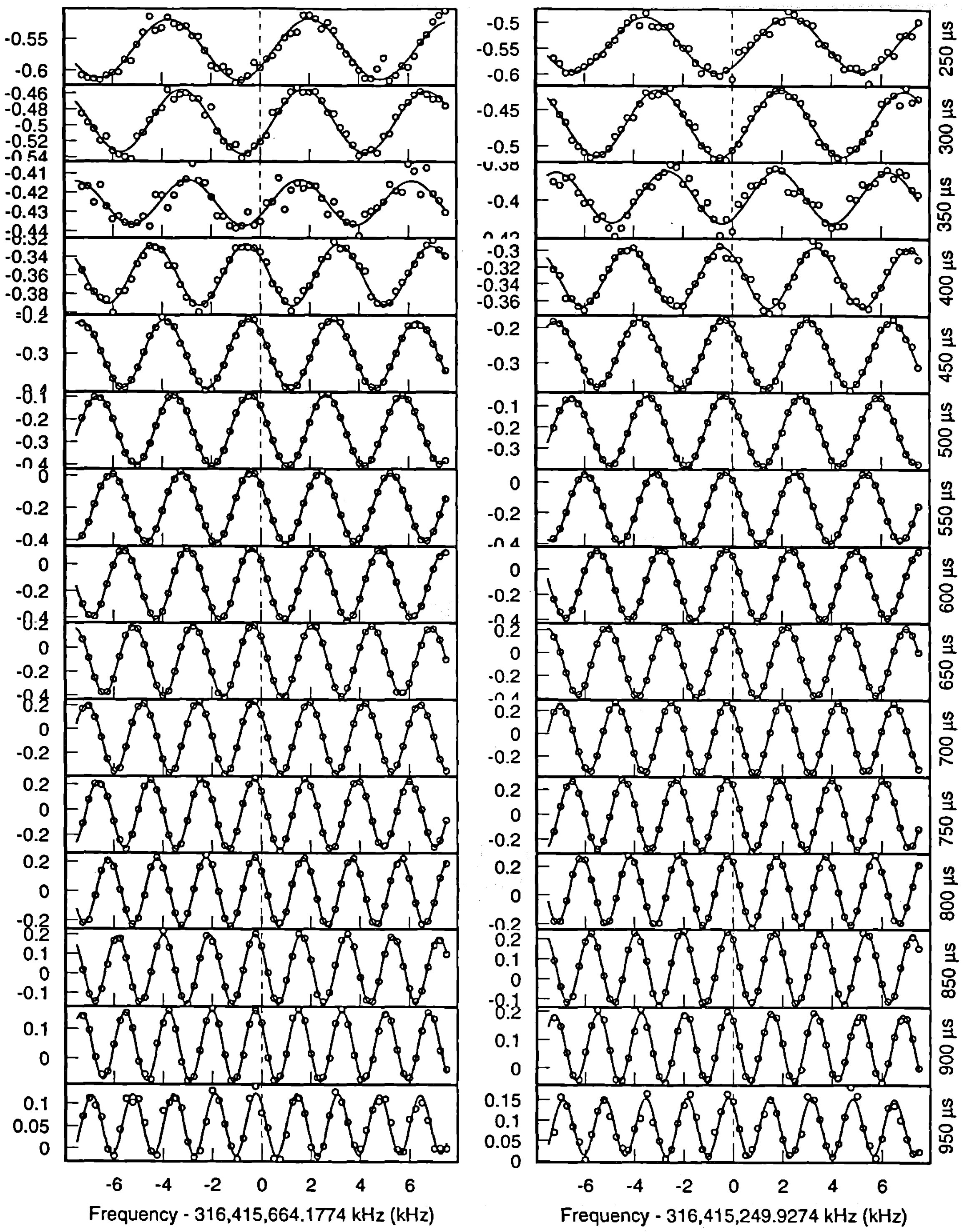

Figure 8-1: Fit of sinusoidal lineshape to Ramsey resonance data. The "y-axis" is the inversion and the "x-axis" is the millimeter-wave frequency. The data on the left is for the $\Delta m_\ell = +1$ transition, and the data on the right is for the $\Delta m_\ell = -1$ transition. The center frequencies for the two scans differ by ≈414 kHz because of the Zeeman effect. Each time bin is labeled with its start time, on the right side of the figure. The time bins are $\mathcal{T}_{bin} = 50$ μs wide, and the range of arrival times $\mathcal{T}$ covered by all the time bins is 250 μs to 1000 μs. The arrival time $\mathcal{T}$ is the time from production of the Rydberg state to detection, whereas the interaction time T is the time an atom spends between the oscillatory fields.

and slowest atoms tend not to "see" the ideal $\pi/2$-pulse at each oscillatory field, and this reduces the amplitude. There is no arrival time $\mathcal{T}$ for which all of the detected atoms "see" exactly a $\pi/2$-pulse. This is because of the spread of atomic trajectories across the oscillatory fields. Second, the interference of the two fine structure components reduces the amplitude by a factor of C_{fs}, given in Eq. (3.76) with the polarization $\psi \approx 0$. The factor C_{fs} is sinusoidal and vanishes at interaction times T_C that satisfy Eq. (3.78). For the data shown in Fig. 8-1, $T_C = 241$ μs, which corresponds to a arrival time $\mathcal{T}_C = 396$ μs, and the amplitude is small for the time bins which start at 350 μs and 400 μs. The amplitude can be seen to change sign between these two time bins, which corresponds to C_{fs} changing sign. Finally, the slower atoms are more affected by spontaneous decay and transitions driven by thermal radiation, both of which reduce the amplitude.

For each sign of Δm_ℓ, we fit all 15 time bins simultaneously. Each time bin j in Fig 8-1 has four fit parameters: A_j (amplitude), B_j (baseline offset), Φ_j (phase), and T_j (interaction time). There is one parameter common to all of the bins: the relative detector efficiency a. Thus, there is a total of 61 fit parameters. The important fit parameters are Φ_j and T_j, where Φ_j is the phase of the j-th sinusoid at the center of the frequency scan, and T_j is the interaction time of the j-th sinusoid ($1/T_j$ is the period).

For the fits in Fig. 8-1, the reduced-chi-squareds are $\chi^2_r = 1.22(5)$ and $\chi^2_r = 1.09(5)$ for the left and right, respectively. Given that there are $60 \cdot 15 = 900$ data points and 61 fit parameters, we expect the χ^2_r distribution to be nearly gaussian with a standard deviation of $\sigma = 0.052$. The value of χ^2_r for these fits is then 4.2 and 1.8 standard deviations away from the expected value of $\langle\chi^2_r\rangle \approx 1.000$. As a test, We added more parameters (linear and quadratic background, amplitude, and phase) and the reduced-chi-squared stayed the same. Hence, we believe that the excess fluctuations are random. Because of the large pulse to pulse fluctuations in the excitation process, any non-linearity in the detection scheme could easily account for such random scatter. A uniform increase in the size of the error bars by about ten percent would correct for this, but since this is such a small adjustment, we neglect it for the sake of simplicity.

8.3.2 Fit of the lineshape phase

Now we go through the second stage of the fitting process—the fitting of the lineshape phase versus the interaction time—in detail for the example data.

Figure 8-2 shows the (Φ_j, T_j) pairs resulting from the fits shown in Fig. 8-1. The top and bottom graphs are for the $\Delta m_\ell = +1$ and $\Delta m_\ell = -1$ transitions, respectively. We plot the uncertainties in the fit values of Φ_j, but we do not plot the uncertainties in the fit values of T_j. The uncertainties in T_j are negligible compared to those for Φ_j.

The uncertainties in the values of Φ_j vary in size for different interaction times T_j. This is because the amplitude of the lineshape and the number of atoms detected varies as a function of T_j. The uncertainty is largest for the fastest and slowest atoms and also for the interaction times near $T_C = 241$ μs, where the interference between the two fine structure components is entirely destructive.

Figure 8-2 also shows the fits of the model for the phase Φ_j of the lineshape, given in Eq. (3.82). These fits assume zero spin polarization ($\psi = 0$), which is justified in Sec. 7.3. The fit function is a nearly straight line with slope δ_0 and "y-intercept" ϕ_0. The line has a slight curvature because of the second-order Doppler effect. The values of the two fit parameters, δ_0 and ϕ_0, along with the goodness of fit parameter, χ_r^2, are listed in the figure. The important fit parameter is the slope δ_0, which is the detuning of the resonance frequency ω_0 from the center frequency of the scan, ω_C.

The reduced-chi-square χ_r^2 is significantly larger than unity for both of these fits. Given that there are 15 data points and 2 fit parameters, we expect the χ_r^2 distribution to be centered on $\langle \chi_r^2 \rangle \approx 1.00$ and to be nearly gaussian with a standard deviation of $\sigma = 0.40$. The reduced-chi-squares are $\chi_r^2 = 1.91(40)$ and $\chi_r^2 = 2.15(40)$ for the $\Delta m_\ell = +1$ and the $\Delta m_\ell = -1$ data, respectively. Statistically, the χ_r^2 would be higher than this 2% and 1% of the time, respectively.

We believe that these χ_r^2 values are too large because of the distortion due to the interactions between the dipoles in the atomic beam. As mentioned at the beginning of this section, the data considered in this section represents the lowest density of

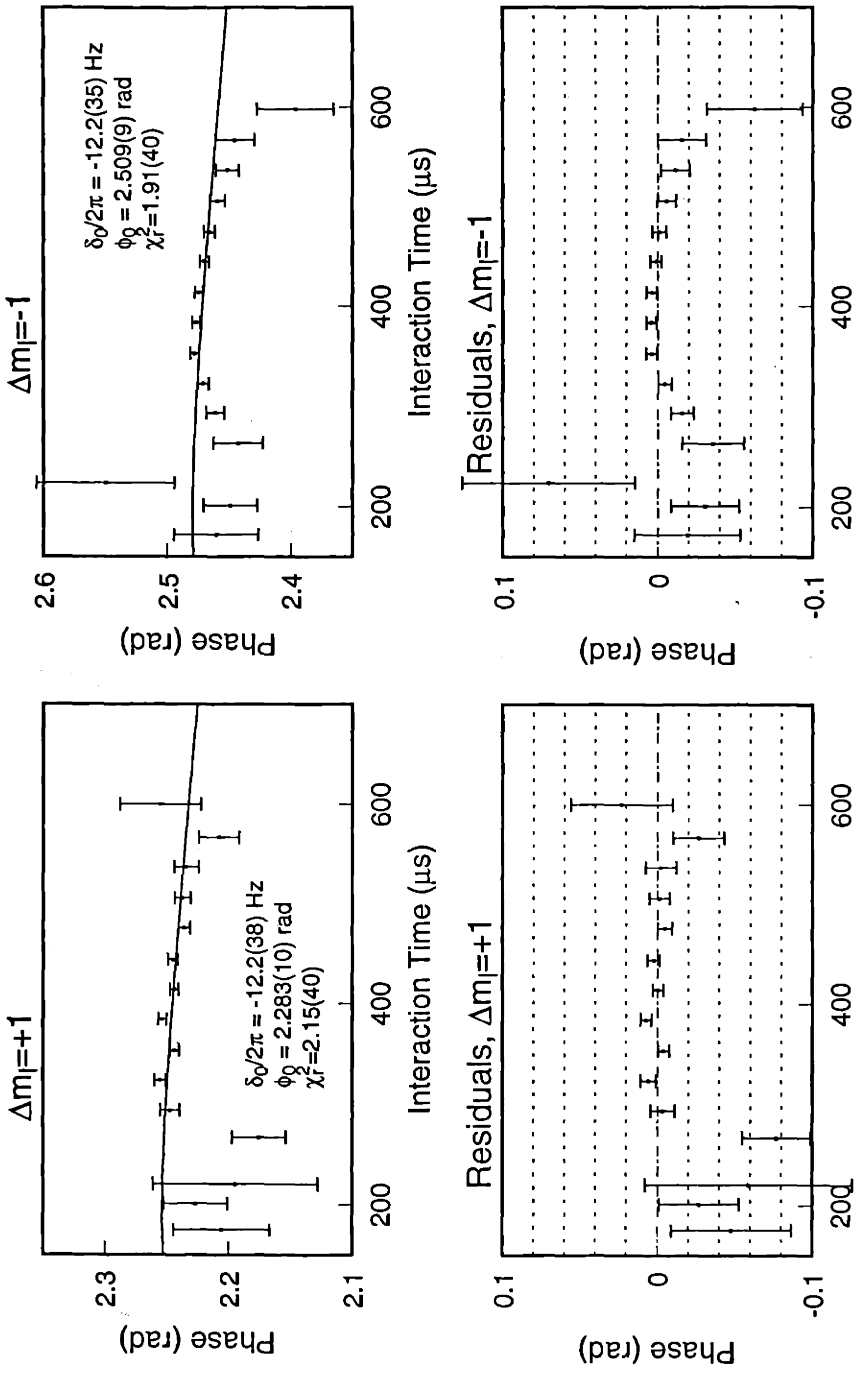

Figure 8-2: Fit of model for the phase of the lineshape, given in Eq. (3.82) with $\psi = 0$, to the (Φ_j, T_j) pairs resulting from the fits shown in Fig. 8-1. The fit function is nearly a straight line with slope δ_0 and "y-intercept" ϕ_0. The slight curvature is due to the second-order Doppler effect. The $\Delta m_\ell = +1$ data is on the left, and the $\Delta m_\ell = -1$ data is on the right. The values of the two fit parameters, δ_0 and ϕ_0, are listed in the figure. The χ_r^2 is significantly higher than one for both fits. We attribute this to the interactions between the dipoles in the atomic beam.

all the data in Table 8.1. The fits for the higher-density data sets in Table 8.1 are of poorer quality. Figure 6-1 shows the poorest quality fit. The data in Figure 6-1 represents the highest-density that we achieved and corresponds to index number "8" in Table 8.1. The quality of the fits call into question the validity of the fit results, especially for the high-density data. At the end of this chapter, we discuss and estimate the error introduced by using a model which ignores the dipole interactions.

Recall that the fit parameter δ_0 is defined as the resonance frequency ω_0 with respect to the scan center ω_C: $\delta_0 = \omega_0 - \omega_C$. Table 8.2 give the values of these parameters for both the $\Delta m_\ell = +1$ and the $\Delta m_\ell = -1$ transitions. The fractional uncertainties in the resonance frequency ω_0 are 1.2×10^{-11} and 1.1×10^{-11} for the $\Delta m_\ell = +1$ and $\Delta m_\ell = -1$ transitions, respectively.

	$\Delta m_\ell = +1$	$\Delta m_\ell = -1$
Scan center $\omega_C/2\pi$	316 415 664 177.4	316 415 249 927.4
Relative fit frequency $\delta_0/2\pi$	−12.2(38)	−12.2(35)
Absolute fit frequency $\omega_0/2\pi$	316 415 664 165.2(38)	316 415 249 915.2(35)

Table 8.2: Values of the frequency parameters, ω_C, δ_0, and ω_0, for both the $\Delta m_\ell = +1$ and the $\Delta m_\ell = -1$ transitions. The units are Hz.

8.3.3 Eliminating the Zeeman effect

It is a simple matter to eliminate the first-order Zeeman effect: we take the average of the two values of ω_0 found from the data on the $\Delta m_\ell = +1$ and the $\Delta m_\ell = -1$ transitions. If we label the average of the center frequencies ω_C as $\bar{\omega}_C$ and the average of the fit values for the resonance detunings δ_0 as $\bar{\delta}_0$, then the average transition frequency, which we label as $\bar{\omega}_0$, is

$$\begin{aligned} \bar{\omega}_0/2\pi &= (\bar{\omega}_c + \bar{\delta}_0)/2\pi = 316\,415\,457\,052.4 - 12.2(26) \text{ Hz} && (8.1) \\ &= 316\,415\,457\,040.2(26) \text{ Hz} && (8.2) \\ & && (8.3) \end{aligned}$$

where the uncertainty of 2.6 Hz comes from the uncertainty in the two fit values of δ_0: $\sqrt{(3.8)^2 + (3.5)^2}/2 = 2.6$.

8.3.4 Correcting for the Stark effect

In this section, we correct for the second-order Stark effect due to the uniform applied field and the stray fields.

As discussed in Sec. 5.2, by measuring the first-order Stark effect at several different voltages V, we determine: the effective plate spacing d, the constant offset field f_0, and the horizontal mean-square field $\overline{f_\perp(x)^2}$. Also discussed in Sec. 5.2 is our estimate of the stray vertical mean-square field: $\overline{f_\parallel(x)^2} = 9.0(45)$ (mV/cm)^2. Combining Eqs. (5.1) and (5.2), we find the size of the second-order Stark effect as a function of the plate bias V and the field parameters:

$$\nu_S = \alpha \left(\frac{V}{d} + f_0 \right)^2 + \alpha \overline{f_\perp(x)^2} + \alpha \overline{f_\parallel(x)^2}. \tag{8.4}$$

The uncertainties in the field parameters, δf_0, δd, and $\delta \overline{f_\perp(x)^2}$, are largely uncorrelated, and the uncertainty in ν_S is

$$\delta\nu_S \approx \sqrt{\left(\frac{2\alpha V^2}{d} \delta V \right)^2 + \left(\frac{2\alpha V}{d} \delta f_0 \right)^2 + \left(\frac{2\alpha V^2}{d^3} \delta d \right)^2 + \left(\alpha \delta \overline{f_\perp(x)^2} \right)^2 + \left(\alpha \delta \overline{f_\parallel(x)^2} \right)^2}. \tag{8.5}$$

For the data considered in this section, the bias voltage was V=+0.19995(1). From measurements of the first-order Stark effect performed on the same day, we find the field parameters to be: $f_0 = 0.099(23)$ mV/cm, $d = 2.44598(13)$ cm, and $\overline{f_\perp(x)^2} = 20.8(31)$ (mV/cm)^2. The values of the field parameters are consistent from day to day for the data sets shown in Table 8.1. Using Eqs. (8.4–8.5) and $\alpha = -12\,588.06$ Hz/(V/cm)^2, the second-order Stark effect is $\nu_S = -84.32(8)$ Hz. The uncertainty in this result is negligible.

8.3.5 Correcting for the fine structure

We correct for the relativistic mass variation by subtracting $\nu_{fs\mu}$, given in Eq. (2.35)

$$\nu_{fs\mu} = 12\,188.30(0)\ \text{Hz} \tag{8.6}$$

from the measured resonance frequency. Recall that the fine structure splitting $\Delta\nu_{fs\mu} = 2068.9(52)$ is dealt with in the fitting process.

8.3.6 Extracting $\nu_{nr\mu}$ and cR_∞

Table 8.3 summarizes the process we used to extract $\nu_{nr\mu}$ and cR_∞ from the fit transition frequencies ω_0, taken from Table 8.2. First we average these two results resulting in the frequency corrected for first-order Zeeman shifts. Then we correct for the second-order Stark contribution, and the fine structure contribution due to the relativistic variation of the mass. This yields $\nu_{nr\mu}$. Note that the Q.E.D. and hyperfine effects are negligible. Then we solve for the hydrogen Rydberg frequency cR_H. Finally, we apply the finite-mass correction to arrive at the infinite-mass Rydberg

ν_0 for $\Delta m_\ell = +1$	316 415 664 165.2(38) Hz	1.2×10^{-11}
ν_0 for $\Delta m_\ell = -1$	316 415 249 915.2(35) Hz	1.1×10^{-11}
$\bar{\nu}_0$ (Zeeman corrected)	316 415 457 040.2(26) Hz	8.2×10^{-12}
ν_S (Stark correction)	+84.32(8) Hz	0.3×10^{-12}
$\nu_{fs\mu}$ (fine structure correction)	−12 188.30(0) Hz	negligible
$\nu_{nr\mu}$ (non-relativistic and field free)	316 415 444 936.2(26) Hz	8.2×10^{-12}
hydrogen Balmer formula: $cR_H = \nu_{nr\mu}\left(\frac{1}{27^2} - \frac{1}{28^2}\right)^{-1}$	$\div\ 9.623\,190\,840\,122 \times 10^{-5}$	exact
finite-mass correction $cR_\infty = cR_H\left(1 + \frac{m_e}{m_H}\right)$	$\times\ 1.000\,544\,617\,023\,2(12)$	1.2×10^{-12}
Rydberg frequency cR_∞	3.289 841 960 257(27) kHz	8.3×10^{-12}

Table 8.3: Extraction of the Rydberg frequency cR_∞ from the data set shown in Fig. 8-1. The stated uncertainty in this value for cR_∞ is due entirely to statistical uncertainty of the data in Fig. 8-1: the Stark, fine structure, and finite-mass correction add negligible uncertainty.

frequency cR_∞. The uncertainty of 2.7 Hz in cR_∞ is dominated by the statistical uncertainty in the fit transition frequencies taken from Table 8.2.

8.4 Final result for cR_∞

8.4.1 Results for cR_∞ from each data set

Using the procedure described in Secs. 8.2 and 8.3, we extracted cR_∞ from each data set in Table 8.1. We present the results in Table 8.4. The data set acquired on May 8 is the one used as an example in Sec. 8.3. The uncertainties for cR_∞ in Table 8.4 are discussed in Sec. 8.3.6 for the example data set. They are dominated by the statistical uncertainty of the Ramsey resonance data. In the next two sections, we discuss uncertainty due to excess fluctuations and systematic error associated with dipole interactions.

Index	Date	Bias	Counting Rate R	cR_∞ (kHz)	Uncertainty
1	April 12	+0.2 V	1.10×10^4 s^{-1}	3 289 841 960 275(33)	1.0×10^{-11}
2	April 12	−0.2 V	1.10×10^4 s^{-1}	3 289 841 960 321(33)	1.0×10^{-11}
3	May 8*	+0.2 V	0.51×10^4 s^{-1}	3 289 841 960 257(27)	0.8×10^{-11}
4	May 16	+0.5 V	1.15×10^4 s^{-1}	3 289 841 960 263(26)	0.8×10^{-11}
5	May 16	−0.5 V	1.22×10^4 s^{-1}	3 289 841 960 305(34)	1.0×10^{-11}
6	May 16*	+0.5 V	0.81×10^4 s^{-1}	3 289 841 960 262(41)	1.2×10^{-11}
7	May 16*	−0.5 V	0.75×10^4 s^{-1}	3 289 841 960 387(36)	1.1×10^{-11}
8	May 21	+0.4 V	2.25×10^4 s^{-1}	3 289 841 960 342(35)	1.1×10^{-11}
9	May 21	−0.4 V	2.20×10^4 s^{-1}	3 289 841 960 304(40)	1.2×10^{-11}
10	May 21*	+0.4 V	0.69×10^4 s^{-1}	3 289 841 960 452(76)	2.3×10^{-11}
11	May 21*	−0.4 V	0.67×10^4 s^{-1}	3 289 841 960 341(80)	2.4×10^{-11}

Table 8.4: Extraction of the Rydberg frequency cR_∞ for all the n=27→28 data sets listed in Table 8.1. The stated uncertainty in cR_∞ is dominated by the statistical uncertainty of the Ramsey resonance data. The Stark, fine structure, and finite-mass corrections add negligible uncertainty. These results have not been corrected for the systematic error due to dipole interactions.

Figure 8-3 shows the results for cR_∞ from Table 8.4. The cR_∞ results are organized along the x-axis according to the index numbers from Table 8.4. The figure separates

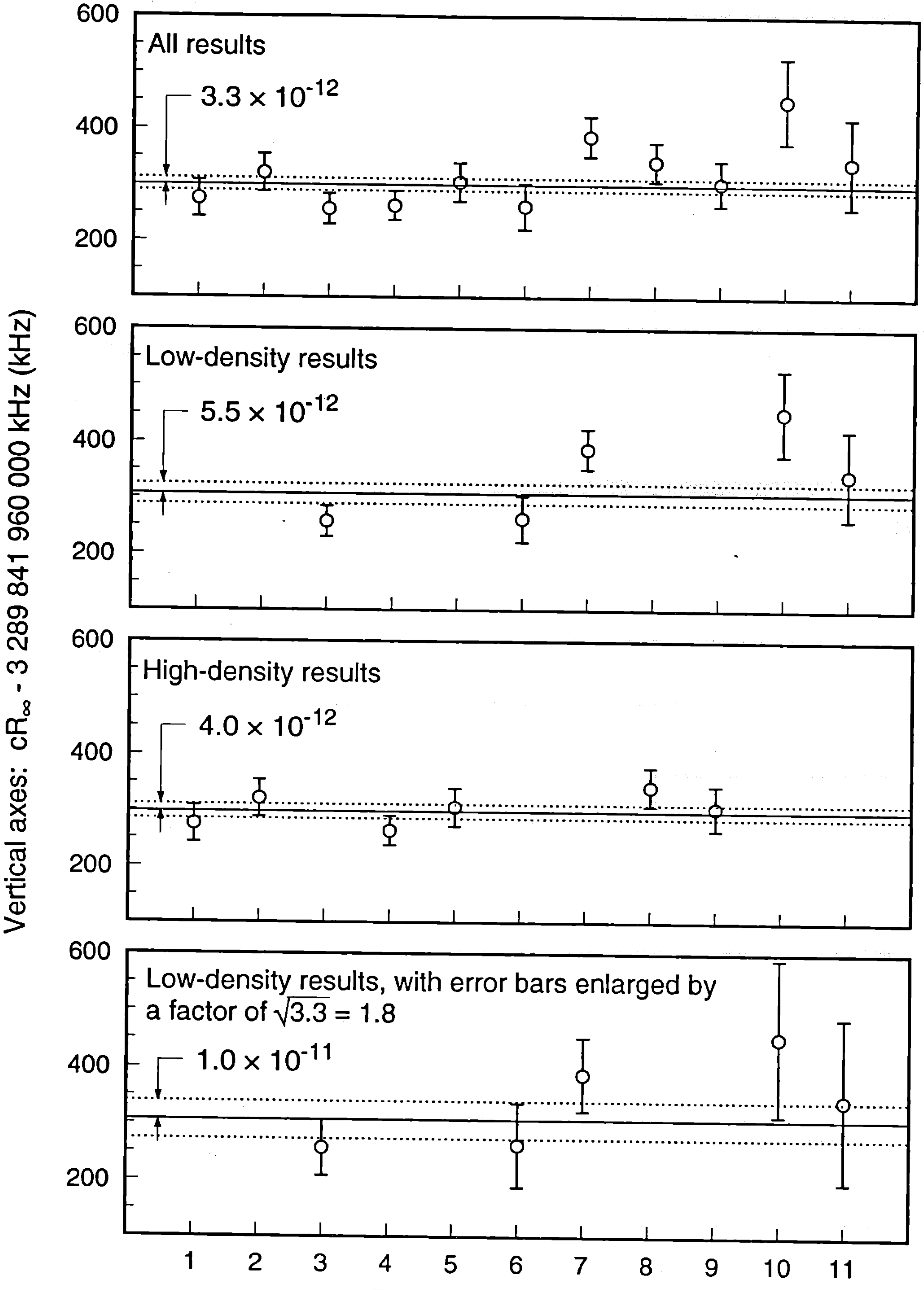

Figure 8-3: Plot of cR_∞ results for low- and high-density. The index number corresponds to those in Table 8.1 and 8.4. The solid horizontal lines are the weighted means. The dashed horizontal lines represent the standard deviations of the means.

the data by low- and high-density. As discussed later, we use only the low-density results, marked with an asterisk in Table 8.4. The upper plot in Fig. 8-3 displays all the results, the upper-middle plot shows the low-density results, the lower-middle plot shows the high-density results, and the lower plot shows the low-density results with enlarged error bars, as explained in the next section. Each plot has a solid line which is a fit of a horizontal line to the data in the plot. Thus each solid line is the weighted mean of the data in the plot. Each plot has a pair of dashed lines which represent the standard deviation of the mean, as reported by the fitting routine. Table 8.5 gives the weighted mean, the standard deviation of the mean, and the reduced-chi-square χ_r^2 for each of the four plots.

Plot	weighted mean	χ_r^2
All results	3 289 841 960 300(11) kHz	1.8
Low-density results	3 289 841 960 306(18) kHz	3.3
High-density results	3 289 841 960 297(13) kHz	0.9
Low-density results with enlarged error bars	3 289 841 960 306(33) kHz	1.0

Table 8.5: Statistics for low- and high- density cR_∞ results. The weighted means are plotted as solid lines in Fig. 8-3.

8.4.2 Excess scatter in low-density results

As can be seen in the upper-middle plot in Fig. 8-3, the distribution of low-density results for cR_∞, shows excess scatter. The reduced-chi-square for the fit in the upper-middle plot is $\chi_r^2 = 3.3$. Statistically, we would expect a χ_r^2 this high or higher about one percent of the time. We do not know the origin of this excess scatter for the low-density data, but we assume that the scatter is due to random fluctuations which average to zero. In this case, the proper approach is to increase the uncertainties by a factor of $\sqrt{3.3} = 1.8$ such that the χ_r^2 is equal to one. Because the error bars are increased by a uniform factor, the value of the weighted mean remains the same while the standard deviation of the mean goes up (by a factor of 1.8).

8.4.3 Estimation of the systematic error due to dipole interactions

The cR_∞ results in Table 8.4 are questionable because the fit model ignores the chief systematic, the dipole interactions, resulting in poor quality fits. This is especially the case for the high-density results. Consequently, we do not use the high-density results except to estimate the the systematic error in the low-density results.

Examining Table 8.5, it can be seen that the result for cR_∞ is surprisingly independent of the density. The difference in the result for cR_∞ between low- and high-density is $\Delta cR_\infty = (cR_\infty)_{low} - (cR_\infty)_{high} = 9(35)$ kHz, which is consistent with zero difference. Thus, while the distortion to the lineshape phase is significantly more pronounced for the high-density data, the slope of the lineshape phase is not significantly different for the high-density data. In other words, the dipole interactions have a statistically significant effect on the *shape* of the lineshape phase versus interaction time T, but the dipole interactions do not have a statistically significant effect on the fit value for the *slope* of the lineshape phase versus interaction time T.

We now estimate the systematic error, Δ_{dipole}, in the low-density result for cR_∞ due to the dipole interactions. The fact that there is no statistically significant dependence on the density does not mean that we can assume that there is zero density dependence. Instead, we take the expected value of the density-dependence of the low-density result to be zero, but with some uncertainty. We take the value of this uncertainty to be the RMS difference between the low- and high-density results, given by

$$\sqrt{\langle(\Delta cR_\infty)^2\rangle} = \sqrt{\langle[(cR_\infty)_{low} - (cR_\infty)_{high}]^2\rangle}, \tag{8.7}$$

From Table 8.5, the difference in cR_∞ between the low- and high-density results is $\Delta cR_\infty = 9(35)$ kHz. Using this, it can easily be shown that the RMS difference is given by 36 kHz ($\sqrt{9^2 + 35^2} = 36$). The uncertainty in Δ_{dipole} of 36 kHz is correlated with the uncertainty in $(cR_\infty)_{low}$ of 33 kHz. To be conservative, we arbitrarily take these two uncertainties to be completely correlated such that the total uncertainty in the low-density result is the sum: 33 kHz + 36 kHz = 69 kHz.

8.4.4 Final result

Table 8.6 summarizes the final result for cR_∞. The top line is the weighted mean of low-density results for cR_∞. The second line is the same except the error bars are increased to account for the excess scatter in the low-density results for cR_∞. The third line is the estimated systematic error due to dipole interactions. The bottom line is the final result for cR_∞. To be conservative, we have arbitrarily taken the uncertainties in the second and third lines to be correlated such that the total uncertainty is the sum: 33 kHz + 36 kHz = 69 kHz.

Low-density result for cR_∞	3 289 841 960 306 (18)
Low-density result for cR_∞ with enlarged error bars	3 289 841 960 306 (33)
Systematic error due to dipole interactions, Δ_{dipole}	0(36)
Final result for cR_∞	3 289 841 960 306 (69)

Table 8.6: The fractional uncertainty of the final result for cR_∞ is 2.1×10^{-11}.

Table 8.7 compares our final result with CODATA 98[MT00] recommended value, which is based on all measurements (except this one) and is up to date. The CODATA 98 result is largely based on optical measurements of transitions in hydrogen and deuterium involving low-lying states. Our result is in acceptable agreement with the CODATA 98 result. The uncertainties of our result and the CODATA 98 result are uncorrelated. The third line in Table 8.7 is the weighted average of the CODATA result and our result. The uncertainty in the combined result is a few percent less

	Rydberg frequency cR_∞	Rydberg constant R_∞	relative uncertainty
Our result	3 289 841 960 306(69) kHz	10 973 731.568 34(23) m^{-1}	2.1×10^{-11}
CODATA 98	3 289 841 960 368(25) kHz	10 973 731.568 55(8) m^{-1}	7.6×10^{-12}
Combined	3 289 841 960 361(24) kHz	10 973 731.568 53(8) m^{-1}	7.3×10^{-12}

Table 8.7: Comparison and combination of this work and CODATA 98.

than the CODATA result, and the value of the combined result is 0.3 σ smaller than the CODATA 98 result.

Our final result has little impact on the currently accepted value of cR_∞ because of its large uncertainty. Nevertheless, the impact on our confidence in cR_∞ is large because we use a completely different technique and because our measurement is insensitive to Q.E.D. effects and nuclear size effects.

Appendix A

Finite-Mass Correction to Stark Effect

After searching the literature, we could not find any reference on how the finite mass of the proton modifies the Stark effect. We use a simple classical argument to show that the problem of two bodies bound by a Coulomb field and also subjected to a uniform electric field can be separated into two one-body problems: one problem for the center of mass motion and the other problem for the relative motion.

The classical equations of motion for both the electron and the proton are:

$$\begin{aligned} m_p\ddot{\vec{r}}_p &= \frac{e^2}{\kappa}\frac{\vec{r}_e-\vec{r}_p}{|\vec{r}_e-\vec{r}_p|^3}+e\vec{F}, \\ m_e\ddot{\vec{r}}_e &= -\frac{e^2}{\kappa}\frac{\vec{r}_e-\vec{r}_p}{|\vec{r}_e-\vec{r}_p|^3}-e\vec{F}, \end{aligned}$$

where e is the charge of the proton, $\kappa = 4\pi\epsilon_0$, and $\vec{F}$ is the electric field. By making the usual transformation to the variables

$$\begin{aligned} \vec{r} &= \vec{r}_e-\vec{r}_p \\ \vec{R} &= \frac{m_e\vec{r}_e+m_p\vec{r}_p}{m_e+m_p}, \end{aligned}$$

we obtain

$$\begin{aligned} M\ddot{\vec{R}} &= 0 \\ \mu\ddot{\vec{r}} &= -\frac{e^2}{\kappa}\frac{1}{r^2} - e\vec{F}, \end{aligned}$$

where $M = m_e + m_p$ is the total mass and $\mu = m_e m_p/(m_e + m_p)$ is the reduced mass. Thus, the problem remains separable in a uniform electric field, and in order to correct our quantum Stark calculations for the finite mass of the proton, we just replace the electron mass m_e with the reduced mass μ.

The Stark effect, as given in Eq. (2.5), contains the mass of the electron via the factors of $a_0 = \kappa\hbar^2/m_e e^2$. To replace m_e with μ, we simply multiply each factor of a_0 with a factor of m_e/μ.

Appendix B

Second-Order Perturbation Theory for $B_\perp$ on circular state

In this appendix, we calculate the effect of a non-parallel magnetic field by finding the second-order perturbation energy for a circular state due to $H_{Z\ell\perp} = \mu_B L_x B_\perp$. We ignore both the electron spin and the finite mass of the proton. We ignore the n-mixing due to the Stark effect, so that the eigenstates of the unperturbed Hamiltonian $H_0 = H_{nr} + H_S + H_{Z\ell\|}$ are the parabolic states:

$$H_0|nkm_\ell\rangle = \left(-\frac{cR_\infty}{n^2} + \frac{3}{2}ea_0nkF + \mu_B m_\ell B_\|\right)|nkm_\ell\rangle. \tag{B.1}$$

We start with the circular state for which $n, \ell = m_\ell = n-1$, and we label this circular state as $|i\rangle$. Later we will generalize the result to include the circular state which has the opposite sign of m_ℓ. The expression for the second-order perturbation energy involves a sum over all other states $|j\rangle$, and is given by:

$$E_i^{(2)} = \sum_{j\neq i} \frac{|\langle i|H_{Z\ell\perp}|j\rangle|^2}{E_i - E_j}, \tag{B.2}$$

where E_i and E_j are the energies of the $|i\rangle$ and $|j\rangle$ states, respectively, and the summation is over all possible states $|j\rangle$ other than the state $|i\rangle$. For parabolic basis states, the selection rules for $H_{Z\ell\perp}$ are $\Delta m_\ell = \pm 1$ and $\Delta n = 0$. $H_{Z\ell\perp}$ only connects

$|i\rangle$ to two other parabolic basis states, the near-circular states $|n; k = \pm 1; m_\ell - 1\rangle$, which we label $|+\rangle$ and $|-\rangle$. We find that these two matrix elements are identical: $|\langle i|H_{Z\ell\perp}|\pm\rangle|^2 = \frac{n-1}{4}(\mu_B B_\perp)^2$. The computation of these two matrix elements is straightforward: we decompose the $|\pm\rangle$ states into spherical basis states: $|\pm\rangle = \frac{1}{\sqrt{2}}(|n,\ell,m_\ell - 1\rangle \pm |n,\ell-1,m_\ell-1\rangle)$, and then employ the ladder operators, $L_\pm = L_x \pm iL_y$. Because the states $|\pm\rangle$ lie above and below the circular state, their effects cancel to a large extent. However, the exact cancelling is prevented by the first-order Zeeman effect due to $B_{||}$.

The expression for $E_i^{(2)}$, including only the two non-zero terms is

$$E_i^{(2)} = \frac{|\langle i|H_{Z\ell\perp}|+\rangle|^2}{E_i - E_+} + \frac{|\langle i|H_{Z\ell\perp}|-\rangle|^2}{E_i - E_-} = \frac{n-1}{4}(\mu_B B_\perp)^2 \left(\frac{1}{E_i - E_+} + \frac{1}{E_i - E_-}\right). \tag{B.3}$$

We write the energy separations in the denominators as

$$E_i - E_\pm = \mp\frac{3}{2}ea_0 nF + \epsilon, \tag{B.4}$$

where $\mp\frac{3}{2}ea_0nF$ is the separation due to the first-order Stark effect and ϵ is the separation due to the the first-order Zeeman effect. Because $|\epsilon| \ll |\frac{3}{2}nF|$, we can approximate the two terms in parentheses in Eq. B.3 as

$$\left(\frac{1}{-\frac{3}{2}ea_0nF + \epsilon} + \frac{1}{\frac{3}{2}ea_0nF + \epsilon}\right) \approx -2\frac{\epsilon}{\left(\frac{3}{2}ea_0nF\right)^2} \tag{B.5}$$

If ϵ were zero, the expression for $E_i^{(2)}$ would vanish.

We calculate ϵ with the help of Eq. (2.12):

$$\begin{aligned} \epsilon &= \mu_B B_{||}\left[m_\ell - (m_\ell - 1)\right] \\ &= \mu_B B_{||}. \end{aligned} \tag{B.6}$$

Using this expression for ϵ and Eq. B.5 we obtain the following result for $E_i^{(2)}$:

$$E_i^{(2)} \approx -\frac{n-1}{2} \frac{\mu_B^3 B_{\parallel} B_{\perp}^2}{\left(\frac{3}{2} e a_0 n F\right)^2}. \tag{B.7}$$

Now we turn our attention to generalizing this result to include the circular state which has the opposite sign for the magnetic quantum number: $m_\ell = -(n-1)$. The matrix elements $\langle i | H_{Z\ell\perp} | \pm \rangle$ stay the same, as do the energy separations due to the first-order Stark effect, but the sign of ϵ changes. We only need to make one small change to Eq. B.7, which is to change the sign. To include this sign change, we make the simple replacement: $(n-1) \rightarrow m_\ell$. The general result for the second-order perturbation energy due to $H_{Z\ell\perp}$ on a circular state is:

$$E_{Z\ell\perp} \approx -\frac{m_\ell}{2} \frac{\mu_B^3 B_{\parallel} B_{\perp}^2}{\left(\frac{3}{2} e a_0 n F\right)^2}. \tag{B.8}$$

Appendix C

Expectation Value of H_{fs} for Spherical Basis States

The goal of this appendix is to calculate the expectation value of H_{fs} for the spherical basis states, which we write as $E_{fs} = \langle n, \ell, m_\ell | H_{fs} | n, \ell, m_\ell \rangle$, or simply $E_{fs} = \langle H_{fs} \rangle$, with the quantum numbers understood. The Hamiltonian H_{fs}, given in Eq. 2.23, is duplicated here:

$$H_{fs} = \underbrace{\frac{-p^4}{8m_e^3c^2}}_{H_{mv}} + \underbrace{\frac{e^2}{2\kappa m_e^2c^2}\frac{1}{r^3}\vec{L}\cdot\vec{S}}_{H_{SO}} + \underbrace{\frac{\pi e^2\hbar^2}{2\kappa m_e^2c^2}\delta(r)}_{H_{Darwin}} + O\left(\frac{1}{c^4}\right). \tag{C.1}$$

For ease of calculation, we rewrite this Hamiltonian with several changes: 1) we exclude the Darwin term which vanishes for states with $l \neq 0$, 2) we rewrite $\vec{L}\cdot\vec{S}$ using the ladder operators, defined as: $L_\pm = L_x \pm iL_y$ and $S_\pm = S_x \pm iS_y$, and 3) we rewrite p^4 using the expression for the unperturbed Hamiltonian

$$H_{nr} = \frac{p^2}{2m_e} - \frac{e^2}{\kappa r}. \tag{C.2}$$

With these changes, the perturbation Hamiltonian is

$$H_{fs} = \underbrace{\frac{-1}{2m_ec^2}\left(H_{nr}^2 + H_{nr}\frac{e^2}{\kappa r} + \frac{e^2}{\kappa r}H_{nr} + \frac{e^4}{\kappa^2 r^2}\right)}_{H_{mv}} + \underbrace{\frac{e^2}{2\kappa m_e^2c^2}\frac{1}{r^3}\left(L_zS_z - 2L_-S_+ - 2L_+S_-\right)}_{H_{SO}} . \tag{C.3}$$

We start by calculating the expectation value of the first term: $E_{mv} = \langle H_{mv}\rangle$. Using the eigenvalues of H_{nr} and the expectation values of r^n given in Bethe and Salpeter [BS77] we get

$$\begin{aligned} E_{mv} &= -\frac{1}{2m_ec^2}\left[\left(\frac{-hcR_\infty}{n^2}\right)^2 + \frac{-hcR_\infty}{n^2}\frac{e^2}{\kappa a_0 n^2} + \frac{e^2}{\kappa a_0 n^2}\frac{-hcR_\infty}{n^2} + \frac{e^4}{\kappa^2 a_0^2 n^3(\ell+1/2)}\right] \\ &= hcR_\infty\frac{\alpha^2}{n^3}\left(\frac{3}{4n} - \frac{1}{\ell+1/2}\right) \end{aligned} \tag{C.4}$$

Next we calculate the matrix element of the second term: $E_{SO} = \langle H_{SO}\rangle$. Using the matrix elements for the ladder operators: $J_\pm|j,m\rangle = \hbar\sqrt{(j\mp m)(j\pm m+1)}|j,m\pm 1\rangle$, we find that the expectation value of the terms containing the raising and lowering operators vanish, leaving only:

$$E_{SO} = \frac{e^2}{2\kappa m_e^2c^2}\frac{\hbar^2 m_\ell m_s}{a_0^3 n^3\ell(\ell+1/2)(\ell+1)} \tag{C.5}$$

$$= hcR_\infty\frac{\alpha^2}{n^3}\frac{m_\ell m_s}{\ell(\ell+1/2)(\ell+1)} \tag{C.6}$$

Adding E_{mv} and E_{SO}, we get the following result for the expectation value of H_{fs} for a spherical basis state:

$$E_{fs} = hcR_\infty\frac{\alpha^2}{n^3}\left[\frac{3}{4n} - \frac{1}{\ell+1/2} + \frac{m_\ell m_s}{\ell(\ell+1/2)(\ell+1)}\right] . \tag{C.7}$$

Bibliography

[BPR+99] Michael P. Bradley, James V. Porto, Simon Rainville, James K. Thompson, and David E. Pritchard. Penning trap measurements of the masses of ^{133}Cs, ^{87,85}Rb, and ^{23}Na with uncertainties ≤ 0.2 ppb. *Physical Review Letters*, 83(22):4510, 1999.

[BR92] Philip R. Bevington and D.Keith Robinson. *Data Reduction and Error Analysis for the Physical Sciences.* McGraw-Hill, second edition, 1992.

[BS77] Hans A. Bethe and Edwin E. Salpeter. *Quantum Mechanics of One- and Two-Electron Atoms.* Plenum Publishing Corporation, 1977.

[Cha92] Pin Peter Chang. *Measurement of the Rydberg Frequency Using Circular Rydberg States of Atomic Hydrogen.* Ph.d. dissertation, Massachusetts Institute of Technology, Department of Physics, 1992.

[CT87] E.F. Cohen and B.N. Taylor. The 1986 adjustment of the fundamental constants. *Reviews of Modern Physics*, 59(4):1121–1148, 1987.

[CTDL77] Claude Cohen-Tannoudji, Bernard Diu, and Franck Laloën. *Quantum Mechanics.* John Wiley and Sons, 1977.

[dBNJ+97] B. de Beauvoir, F. Nez, L. Julien, B. Cagnac, F. Biraben, D. Touahri, L. Hilico, O. Acef, A. Clairon, and J.J. Zondy. Absolute frequency measurement of the $2S - 8S/D$ transitions in hydrogen and deuterium: New determination of the Rydberg constant. *Physical Review Letters*, 78(3):440–443, 1997.

[Eri77] Glen W. Erickson. Energy levels of one-electron atoms. *Journal of physical and chemical reference data*, 6(3):831, 1977.

[FG00] Chad Fertig and Kurt Gibble. Measurement and cancellation of the cold collision frequency shift in an ^{87}rb fountain clock. *Physical Review Letters*, 85(8):1622, 2000.

[FVH57] R.P. Feynman, F.L. Vernon, Jr., and R.W. Hellwarth. Geometrical representation of the Schrödinger equation for solving maser problems. *Journal of Applied Physics*, 28(49), 1957.

[FW81] John W. Farley and William H. Wing. Accurate calculation of dynamic stark shifts and depopulation rates of rydberg energy levels induced by blackbody radiation. hydrogen, helium, and alkali–metal atoms. *Physical Review A*, 23:2397–2424, 1981.

[GL86] M. Gross and J. Liang. Is a circular Rydberg atom stable in a vanishing electric field? *Physical Review Letters*, 57(25):3160–3163, 1986.

[Jac98] John David Jackson. *Classical Electrodynamics*. John Wiley and Sons, third edition, 1998.

[Kin96] T. Kinoshita. The fine structure constant. *Reports on Progress in Physics*, 59(11):1459, 1996.

[KL66] H. Kogelnik and T. Li. Laser beams and resonators. *Proceedings of the IEEE*, 54(10):1312–1329, 1966.

[LHC$^+$97] R. Lutwak, J. Holley, P.P. Chang, S. Paine, and D. Kleppner. Circular states of atomic hydrogen. *Physical Review A*, 56(2):1443–1452, 1997.

[Lut97] Robert Lutwak. *Millimeter-Wave Studies of Hydrogen Rydberg States*. Ph.d. dissertation, Massachusetts Institute of Technology, Department of Physics, 1997.

[MT00] P.J. Mohr and B.N. Taylor. Codata recommended values of the fundamental physical constants: 1998. *Reviews of Modern Physics*, 72(2), 2000.

[Par60] D.A. Park. Relation between the parabolic and spherical eigenfunctions of hydrogen. *Zeitschrift Fur Physik*, 159:155, 1960.

[Ram56] Norman F. Ramsey. *Molecular Beams.* Oxford University Press, New York, 1956.

[Sil78] H.J. Silverstone. Perturbation-theory of Stark effect in hydrogen to arbitrarily high-order. *Physical Review A*, 18(5):1853–1864, 1978.

[TKSW89] D.C. Thompson, E. Kammermayer, B.P. Stoicheff, and E. Weinberger. Pressure shifts and broadenings of Rb Rydberg states by Ne, Kr, and H_2. *Physical Review A*, 36(5), 1989.

[UHG+97] Th. Udem, A. Huber, B. Gross, J. Reichert, M. Prevedelli, M. Weitz, and T.W. Hänsch. Phase-coherent measurement of the hydrogen $1S-2S$ transition frequency with an optical frequency interval divider chain. *Physical Review Letters*, 79(14):2646–2649, 1997.

Acknowledgments

My time at MIT has been great because of the people that I have met here. I came to MIT because of the large atomic physics community and because essentially all of it was located on one floor of building 26, making for easy interaction. We've shared equipment, ideas, and beers at the Muddy. We've also played sports together: basketball, soccer, and, most notably, softball with the Balldrivers. The Balldrivers provided important opportunities to get out of the lab and onto a grassy field for a low-key game with a fun bunch of guys.

In my early years, I had two great people for officemates: Hong Jiao and Neal Spellmeyer. Both helped me with physics problems, be they for general exams, the experiment, or purely academic.

The success of the Rydberg measurement is due in large part to the thousands of man-hours put in by all the graduate students who have worked on it, namely Peter Chang, Scott Paine, Robert Lutwak, and Jeff Holley. I personally worked with the latter two. Robert Lutwak was the senior graduate student when I came aboard. I worked closely with him and he taught me a great deal about lasers, computers, and NeXT network administration. I have a great deal of respect for him, despite the almost constant friction that existed between us. Once Robert graduated, it was Jeff Holley and I who had to make the measurement work. Jeff Holley is an intelligent, motivated scientist who is a joy to work with. He provided his calm brand of leadership that made the experiment work (except for that one time when he blew his top at me, which I may well have deserved).

Ted Ducas has been of great help, giving me both moral and technical support. This is especially true for the years after the other students graduated. During this time, he has brainstormed with me about the experiment and coached me on thesis writing.

I should also mention helpful discussions that I had with two theorists visiting MIT: James Anglin, Henk Stoof. Discussions with these two helped me get started with the model for the dipole interactions.

The CUA secretary, Carol Costa, has been of great administrative help and has been generally supportive of my work. Our frequent conversations on baseball, East Cambridge, her grandchildrens' exploits, and so forth offered an enjoyable and needed break from thesis writing.

Upstairs in RLE headquarters, Maxine has acted as an extremely helpful, competent purchasing agent for our group, and has done so for many years.

The guys in the ICR group downstairs, James and Simon, have helped me in many ways over the years, including supplying me with liquid helium and computing time on their Mac in my hour of need. Also, they've been good enough to let me play basketball with them over this past summer (along with Steve Moss, may he soon graduate).

The interferometer group, David Kokorowski, Tony Roberts, and Alex Cronin have been helpful. They've offered physics advice, computing time on their Mac, various and sundry laboratory items, time in their fume hood, the list goes on. David and Tony (along with Simon) stand out as people who have taken leadership roles in the Balldrivers organization. Without men like these, softball in the CUA would not be where it is today.

I could go on like this about the AMO physicists in this hallway. Having been hear for eight years and counting, I've been helped by, and also enjoyed the company of, seemingly countless people.

My roommates, past and present, deserve acknowledgement. Two names stand out: Michael Bradley (ICR group) and Steve Cronin. These are friends and fellow physicists, with whom I both revelled and commiserated.

My parents have been very supportive of my work here at MIT. They got me started by helping me move out here and have given me love and encouragement ever since. Thanks Mom and Dad.

I consider myself lucky to have met my fiancee, Meg, during my time here at MIT. She has given me her love, companionship, and a sense of perspective. And she's got a great family to boot!

Our advisor, Dan Kleppner, is a wonderful advisor and always seemed to have a heap of ideas to solve our problems—some of which even worked and/or somehow helped us better understand the real problems.